4-2016

Characterization of a continuous-flow reactor for solar UV water disinfection

Margaret M. Busse
Purdue University

PURDUE UNIVERSITY
GRADUATE SCHOOL
Thesis/Dissertation Acceptance

This is to certify that the thesis/dissertation prepared

By Margaret Busse

Entitled
CHARACTERIZATION OF A CONTINUOUS-FLOW REACTOR FOR UV WATER DISINFECTION

For the degree of   Master of Science in Engineering

Is approved by the final examining committee:

Ernest R. Blatchley III
Chair

Amisha D. Shah

Chad T. Jafvert

Bruce M. Applegate

To the best of my knowledge and as understood by the student in the Thesis/Dissertation Agreement, Publication Delay, and Certification Disclaimer (Graduate School Form 32), this thesis/dissertation adheres to the provisions of Purdue University's "Policy of Integrity in Research" and the use of copyright material.

Approved by Major Professor(s): Ernest R. Blatchley III

Approved by: Dulcy M. Abraham   4/21/2016

Head of the Departmental Graduate Program   Date

CHARACTERIZATION OF A CONTINUOUS-FLOW REACTOR FOR SOLAR UV

WATER DISINFECTION

A Thesis

Submitted to the Faculty

of

Purdue University

by

Margaret M. Busse

In Partial Fulfillment of the

Requirements for the Degree

of

Master of Science in Engineering

May 2016

Purdue University

West Lafayette, Indiana

For my parents for their support and many sacrifices.

ACKNOWLEDGEMENTS

TABLE OF CONTENTS

LIST OF TABLES

LIST OF FIGURES

ABSTRACT

Busse, Margaret M. M.S.E., Purdue University, May 2016. Characterization of a Continuous-Flow Reactor for Solar UV Water Disinfection. Major Professor: Ernest R. Blatchley III.

Lack of access to safe water is a common problem in many developing countries (UNICEF/WHO, 2011). Fortunately, solar ultraviolet (UV) radiation is abundantly available in many of these same areas, and it has been used to accomplish disinfection of drinking water by processes that involve no electrical power, such as solar water disinfection (SODIS). However, conventional SODIS systems are limited by batch processing and exclusion of UVB radiation, which is the most germicidally-active portion of the UV spectrum (Coohill and Sagripanti, 2008). To address these limitations, a continuous-flow solar UV disinfection system was developed to amplify ambient solar UV radiation, while including the UVB portion of the spectrum. With knowledge of the inactivation characteristics of target microbes and ambient spectral irradiance, community-scale, continuous-flow solar UV disinfection systems can be designed. This same information will inform the design of process control devices for these systems that will ensure adequate disinfection.

To address these needs, dose-response experiments were conducted in the UVB range to develop action spectra for two bacteria (*Salmonella typhimurium* LT2, *Vibrio harveyi*) and a protozoan parasite, *Cryptosporidium parvum*. The bacteria were selected as surrogates for the organisms that cause typhoid fever and cholera, respectively. *C. parvum* was studied because it is known to cause cryptosporidiosis, which together with the two selected bacteria, account for a large fraction of waterborne disease outbreaks in developing countries (GEMS, 2013). UV dose-response experiments were carried out between 254 nm to 330 nm using three different collimated beam sources. The range of wavelengths used for these experiments was selected to allow overlap with previously published work for each of these microbes, while at the same time extending measured action spectra across the entire UVB spectrum.

Measurements of UVB spectral irradiance from the USDA UVB Monitoring Network were compared with simulations of UVB spectral irradiance using the Tropospheric Ultraviolet and Visible Radiation Model (TUV) for West Lafayette, Indiana. The TUV model was used to simulate incident, ambient solar spectral irradiance at locations corresponding to planned implementation of the CPC reactor, including Eldoret, Kenya and Port-Au-Prince, Haiti. Integration of measured action spectra with simulated spectral irradiance indicated that peak antimicrobial effectiveness occurs around 320 nm – 330 nm for all three target microbes. This suggests that process control should be based on real-time measurements of UV radiation in this wavelength range.

A raytracing program (Photopia, LTI Optics) was then used to simulate amplification of solar spectral irradiance within the CPC system using the results of TUV simulations as input. Output from the raytracing simulation illustrated the fluence rate distribution throughout the inner tube of the CPC, based on amplification of the input power within the reactor. Integration of these results with computational fluid dynamics (CFD) will allow for future simulations of the inactivation responses of all three microbes in the CPC system at any given location.

CHAPTER 1. INTRODUCTION

1.1   Problem Definition

Globally, 783 million people lack access to an improved water source (UNICEF/WHO,

2011). The United Nations established the millennium development goal to halve the

number of people with no access to improved water by 2015, and this has been achieved.

Unfortunately, even though this goal has been met, these sources are only defined as

improved, and do not guarantee safety or sustainability of the water source (Onda et al.,

2012). To address this, the WHO/UNICEF Joint Monitoring Programme for Water

Supply and Sanitation (JMP) conducted Rapid Assessment for Drinking Water Quality

(RADWQ) between 2006 and 2010. Samples of these defined improved water sources

were collected in five countries (Jordan, Tajikistan, Nicaragua, Nigeria and Ethiopia) and

tested against the World Health Organization (WHO) microbial drinking water standards.

None of the sources were compliant in all of cases, and protected wells alone were

contaminated with waterborne pathogens in over 50% of cases (UNICEF/WHO, 2011).

Figure 1.1 illustrates the percentage of samples form each source type that were non-

compliant with WHO standards for microbial quality.
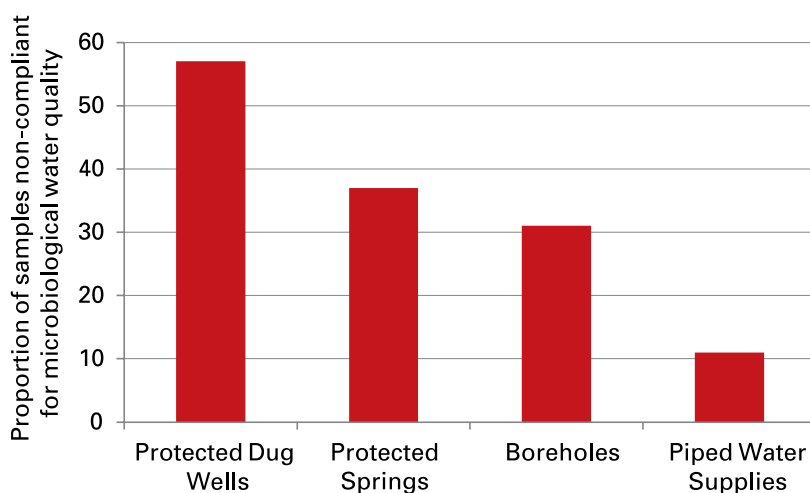
Figure 1.1. Water samples from improved sources not meeting WHO standards for microbial water quality (UNICEF/WHO, 2011).

In a separate study, samples of improved water were collected from 100 homes in Vietnam and Kenya and tested for *Escherichia coli* (Grady et al., 2015). Results of these analyses were compared against the WHO risk categories for drinking water. The samples were taken at the point-of use in each household. Of the 205 improved sources tested, over 60% were considered unsafe to drink. Figure 1.2 provides a more detailed summary of these results.
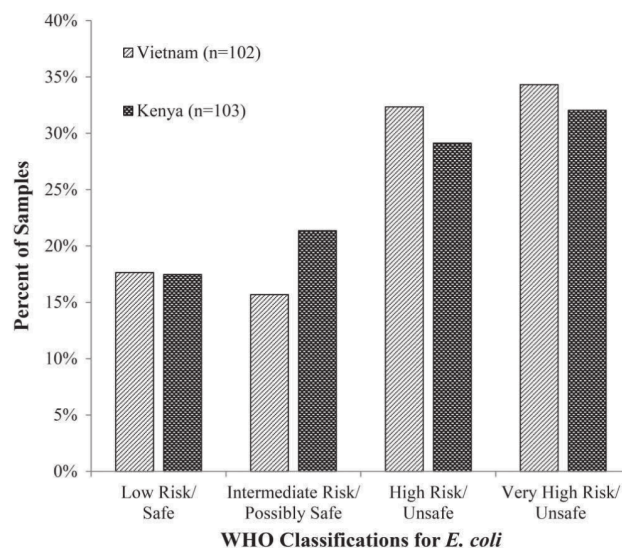
Figure 1.2. Distrubution of samples (by percentage) among WHO classifications for drinking water, based on viable *E. coli* concentration (Grady et al., 2015).

In situations where intervention has taken place, another obstacle is that many of the implemented solutions have actually been more of a burden than benefit to the recipient community. Small community-scale systems are often left unused due to lack of operating and maintenance knowledge and/or supplies. Adding to the complexity, the drinking water conditions that have been least improved are in Least Developed Countries (LDCs), the place where improvement is most needed (UNICEF/WHO, 2011). Access has also been focused on urban areas, while 84% of those in need live in rural areas (UNICEF/WHO, 2011). Figure 1.3 shows that this disparity continues to increase due to commitments of funds for large systems designed for densely populated areas, as opposed to rural communities that rely on small, basic systems.
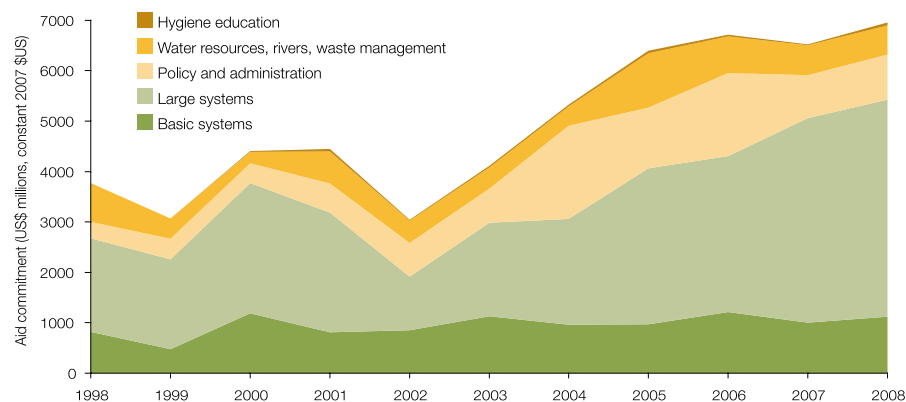
Figure 1.3. Allocation of water related aid money (UNICEF/WHO, 2011).

These small, basic systems include solutions such as rainwater collection, small distribution systems, systems operated by gravity feed, hand pumps, etc. Furthermore, it has been predicted that the pace at which communities have access to improved water will decrease in the future due to the challenges of providing to those in most need (UNICEF/WHO, 2011). As illustrated in Figure 1.4, large percentages of urban populations are expected to have access to piped water sources by 2020 (UNICEF/WHO, 2011). Therefore, UNICEF and the World Health Organization are working to establish sustainable solutions, particularly in rural communities.

Forecast urban water 2020
- No data
- >75% and >50% piped system
- >75%
- 51-75%
- 51-75% and >50% piped system
- 26-50%
- <= 10%
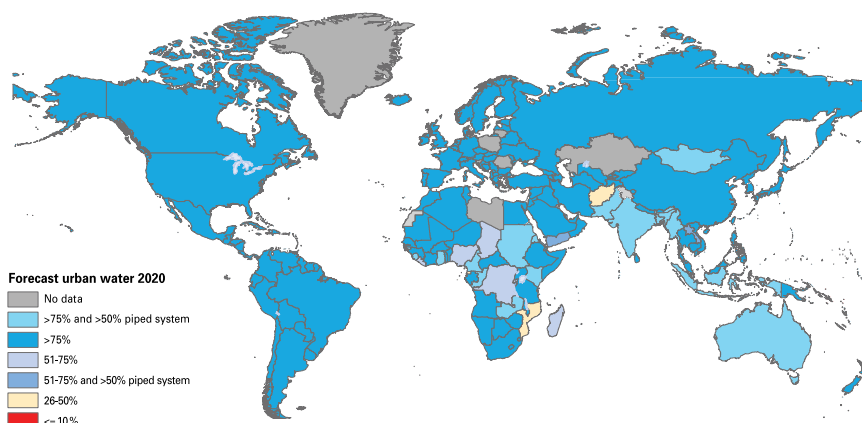
Figure 1.4. Percentages of urban populations predicted to have access to piped water sources by 2020 (UNICEF/WHO, 2011).

Work on this project builds upon the work of Mbonimpa et al. (2012) to develop a solar UV disinfection system based on a low cost compound parabolic collector (CPC) for continuous-flow disinfection of drinking water, applicable in developing countries. This system is a "point-of-use" technology that can be applied in rural regions with intense solar radiation without the requirement of electricity, lamps or batteries (Mbonimpa, 2010).

1.2 Objectives

1.2.1 Determine action spectra for key pathogens

Current disinfection processes, including chlorination and ozonation, lead to hazardous disinfection by-products (DBPs), which can be avoided through disinfection with UV radiation (Hijnen et al., 2006). UV disinfection is a process that depends largely on direct damage to nucleic acids and proteins; some organisms have limited ability to repair this

damage (Coohill and Sagripanti, 2008). The ability of UV radiation to prevent these microorganisms from reproducing is also highly dependent on the distinct physiological and chemical characteristics of each organism as well as variation at the strain level (Blatchley et al., 2001).

E. coli is commonly used as an indicator organism in disinfection. However, many waterborne microbial pathogens are more difficult to inactivate than *E. coli* with UV radiation (Hijnen et al., 2006). However, most previous investigations of UV dose-response behavior have involved wavelengths not found in natural sunlight at earth's surface (Coohill and Sagripanti, 2008). Therefore, experiments were conducted to define the action spectra for key pathogenic organisms (or surrogates) commonly found in contaminated water supplies. This knowledge will allow researchers to understand the behavior of these more UV resistant organisms at wavelengths in the UVB range.

1.2.2   Comparison of TUV model predictions to UVB measurements

Ambient UVB spectral irradiance will be critical to the performance of the continuous-flow solar UV disinfection system that is under investigation. The United States Department of Agriculture (USDA) has established monitoring sites for UVB spectral irradiance. The USDA is interested in this primarily because UVB radiation can damage crops. The locations of monitoring sites with the USDA UVB Monitoring Network were selected based on proximity to agricultural and biological resources; these sites do not necessarily coincide with candidate locations for solar disinfection systems (Bigelow et al., 1998).

Rural communities in developing countries that are near the equator are likely candidates for application of solar UV disinfection, but are not within the USDA monitoring network. Therefore, estimates of ambient UVB spectral irradiance were developed by application of the Tropospheric Ultraviolet & Visible Radiation (TUV) Model. This model predicts spectral irradiance based on input parameters that define time, location and atmospheric composition. Predictions of the TUV model were compared with measurements from the UVB Monitoring Network to allow an assessment of TUV model error.

1.2.3   Define effectiveness spectra to predict performance

The products of the action spectra and available spectral irradiance (from TUV predictions) were used to define effectiveness spectra for each pathogen as a function of wavelength (λ) and location. An effectiveness spectrum will describe the relative contribution of each wavelength to a photochemical process – in this case, UV-induced microbial inactivation (Mbonimpa et al., 2012). The wavelength contributing the most will be crucial for process control for the system.

In turn, the behavior of radiation at key wavelengths was used as input for Photopia, a commercially-available raytracing program, to simulate the performance of a CPC reactor. Output from this modeling effort illustrated the spatial distribution of UVB energy within the CPC reactor. In the future, simulations of this type will also be used as a component of community-scale reactor design.

CHAPTER 2. LITERATURE REVIEW

2.1   UV Inactivation of Microorganisms

2.1.1   Background

The process of UV disinfection is designed to eliminate the ability of a microorganism to be infectious, meaning that the organism may still be alive without the ability to reproduce or infect. Viable cells are those that are able to reproduce. Some microbes are able to repair sub-lethal damage, and those that are unable to overcome this damage are defined non-viable.

The rate of microbial inactivation will vary with wavelength. The three portions of the spectrum with microbial inactivation potential are UVA (380-320 nm), UVB (320-290 nm) and UVC (290-190 nm) (Coohill and Sagripanti, 2008). Most UV inactivation studies are conducted in the UVC range because this is where DNA and proteins absorb most efficiently. Also, most UV disinfection systems are based on UVC sources. UVB is absorbed by nucleotides at the next highest efficiency, followed by UVA. As absorbance decreases, the disinfection time increases (Coohill, 1996).

Mechanisms that cause microbial inactivation in SODIS systems that harness UVA radiation are dominated by thermal processes and reactive oxygen-based intermediates

(Gómez-Couso et al., 2010; Khaengraeng and Reed, 2005). Microbial DNA damage could be promoted by including UVB radiation because it is absorbed by DNA much more strongly than UVA radiation (Setlow, 1974).

UV disinfection processes generally rely on direct damage of nucleic acids through dimerization. In the UVC range, the main photoproducts involved in inactivation are the pyrimidine dimer (5, 6 cyclobutane dipyrimidine) and the photoproducts pyrimidine-pyrimidone (6-4) lesion series and 5-thyminyl-5, 6-dihydrothyomine (Coohill and Sagripanti, 2008). Conventional chemical disinfection processes, such as chlorination and ozonation, involve metabolic interference or cell lysis as inactivation mechanisms (Blatchley et al., 2001). Benefits of UV compared to chlorination include diminished disinfection byproduct (DBP) formation and higher disinfection efficiency for many microorganisms (Guo et al., 2009; Hijnen et al., 2006).

2.1.2   Solar UV Disinfection (SODIS)

UVA radiation accounts for up to 8% of the total solar output, which is the highest of any segment of the UV range (Coohill and Sagripanti, 2008). Solar disinfection (SODIS) is a low cost technology applied in many developing countries that harnesses UVA radiation to yield temperatures above $45^{\circ}C$ and reactive oxygen species to disinfect drinking water (Khaengraeng and Reed, 2005). The process requires at least 6 hours of direct exposure to sunlight in polyethylene terephthalate (PET) plastic bottles to adequately disinfect the water (Luzi et al., 2016), equating to approximately 500 W/m^2 of solar radiation (McGuigan et al., 2011). Factors that can affect the speed of this process and its ability to

achieve adequate disinfection include ambient solar spectral irradiance, temperature, topography, climate and water quality (especially turbidity). An illustration of the time-dependent behavior of available solar radiation is presented in Figure 2.1. For the location illustrated in this figure, these results indicate that on average, 5 hours of exposure resulted in an average peak intensity of 651 W/m^2 with water temperature sustaining 45°C for 3 hours. On the observed sunny days the peak intensity was 735 W/m^2 and this dropped to 457 W/m^2 on recorded cloudy days (Oates et al., 2003). Temporal behavior is likely to be qualitatively similar at other locations.
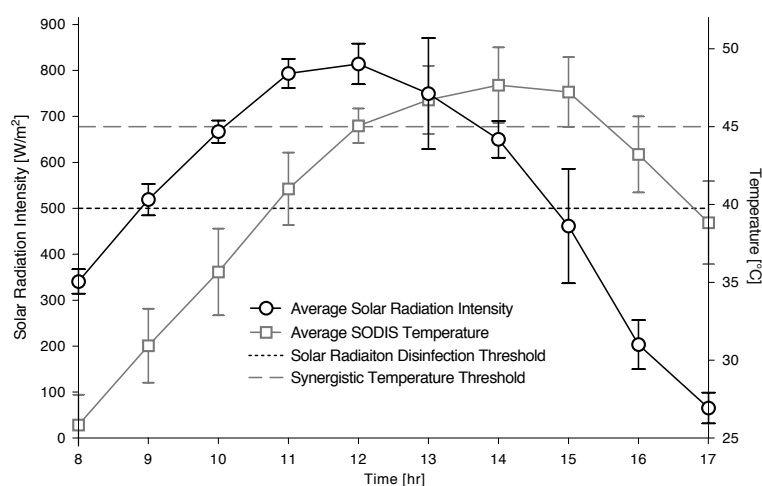
Figure 2.1. Average solar radiation and temperature profile on sunny days for PET bottles exposed during January in Haiti (Oates et al., 2003). Data are illustrated as mean values for the period of February 12-21, 2001.

These results indicate that between the hours of 9 AM and 2 PM the available radiation meets the solar radiation disinfection threshold. This is only for a 5-hour period, and 6 hours of exposure at radiation above 500 W/m^2 is required. Results in Table 2.1 reflect

the consequences of under-exposing the samples. After one day of exposure, the number of samples tested positive for total coliforms was 50%, while 45.8% tested positive for *E. coli.* After two days of exposure, no coliform or H$_2$S producing bacteria were detected (Oates et al., 2003).

Table 2.1. Field studies for inactivation of microorganisms in the SODIS system (Oates et al., 2003).

Total microbial analysis

Target organisms	% (Positive/sampled)[a]		
	Raw water	1-day exposure	2-day exposure
Total coliform[b]	100.0% (24/24)	50.0% (12/24)	0.0% (0/18)
E. coli[b]	91.7% (22/24)	45.8% (11/24)	0.0% (0/18)
H$_2$S producing[c]	100.0% (24/24)	41.7% (10/24)	0.0% (0/17)
Total	97.2% (70/72)	48.3% (33/72)	0.0% (0/53)

[a] Values in parenthesis are number positive tests out of number of tests performed.
[b] Total coliform and *E. coli* were tested with Hach's presence–absence broth.
[c] H$_2$S producing bacteria were tested with Hach's PathoScreen[TM].

Results such as those listed in Table 2.1 indicate that exposure to only UVA radiation can require upwards of 2 days to fully disinfect water, even though 1-day exposure reduces the samples into "low risk" category. Low risk is defined at 1-10 fecal coliforms per 100 mL of sample (WHO, 1997). This is not an uncommon result from SODIS systems. There are varying results in the literature that indicate complete microbial inactivation, where no microbes were detected during testing, can be achieved within a few hours of exposure to the sun to the possibility that there are still organisms present after an entire day of exposure. This range is indicated in Figure 2.2 where solar disinfection studies in the field using PET bottles indicated that disinfection may require less than an hour in some locations, while in other locations the process could take close to 30 hours (Fisher

et al., 2012, 2008). It was also concluded that wild type cultures generally took longer to be inactivated than laboratory cultures (Fisher et al., 2012).
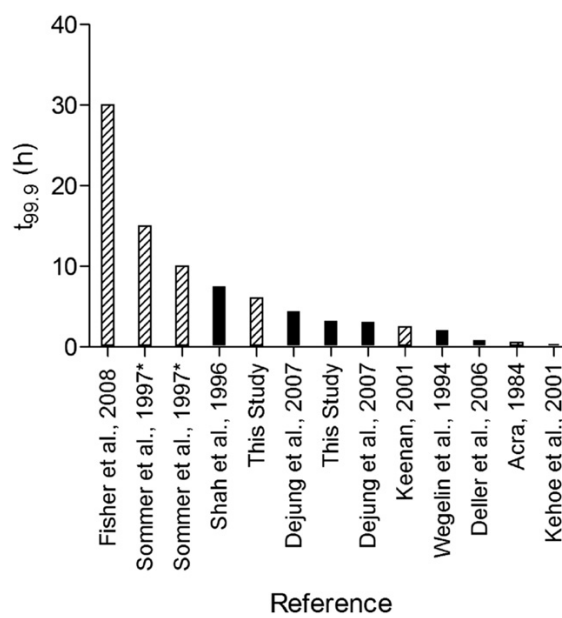
Figure 2.2. Three-log$_{10}$ inactivation times due to solar exposure for *E. coli* wild type (striped bars) and laboratory cultured (solid bars) calculated from published data (Fisher et al., 2012).

One solution to this problem is the addition of accelerating compounds (i.e., catalysts or promoters). Hydrogen peroxide, juice from lemons and limes and some copper materials may be able to accelerate the SODIS process (Fisher et al., 2008). Alternatively, the process may also be enhanced by the inclusion of solar UVB radiation (Mbonimpa et al., 2012).

2.1.3   UVB Range Studies

Most studies of UV disinfection have been conducted in the UVA range (for SODIS systems) or the UVC range (for most commercial UV reactors). Consequently, little work has been done to define microbial responses to UVB radiation.

UVB radiation is generally more germicidally-active than UVA radiation, but it is absorbed by atmospheric ozone (O_3) more strongly than UVA (Madronich et al., 2011). Only a few tenths of a percent of extraterrestrial solar UVB radiation reaches earth's surface (Coohill and Sagripanti, 2008).

Conventional SODIS systems do not make use of UVB radiation because of the absorptive properties of PET plastic. More recent studies have looked into employing plastics with partially UVB-transparent properties. The use of polypropylene copolymer (PPCO), was demonstrated to reduce SODIS disinfection by half compared to PET plastic (Fisher et al., 2012).

Figure 2.4 illustrated, the transmittance characteristics of five plastic materials. The materials included were Eastman Tritan (Tritan), polycarbonate (PC), polypropylene copolymer (PPCO), polystyrene (PS) and polyethylene terephthalate (PET). The only material that allowed measurable transmittance of wavelengths shorter than 300 nm was the PPCO (Fisher et al., 2012).
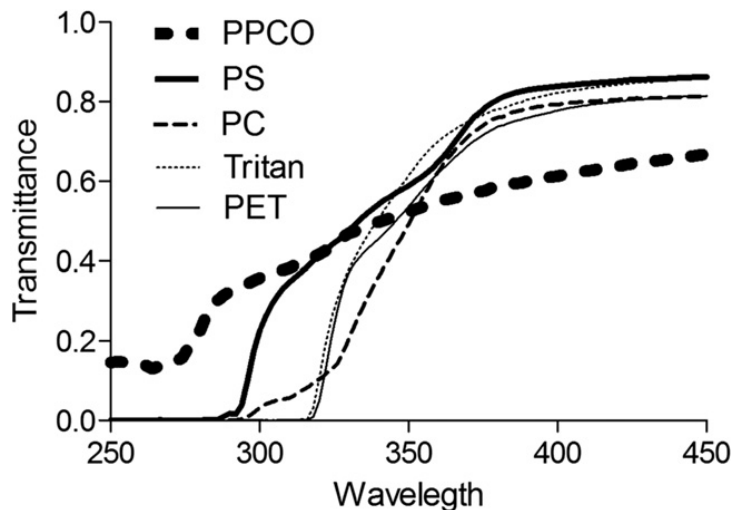
Figure 2.3. Transmittance of plastics used for SODIS bottles (Fisher et al., 2012).

Disinfection of water in SODIS bottles with the above-mentioned materials were evaluated with wastewater and lab-grown *E. coli* and *Enterococcus faecalis* as well as laboratory cultured MS2 coliphages. As illustrated in Figure 2.5, samples that were exposed in PPCO bottles required significantly less time to reach 3-$\log_{10}$ units of inactivation compared to the other four materials (Fisher et al., 2012).
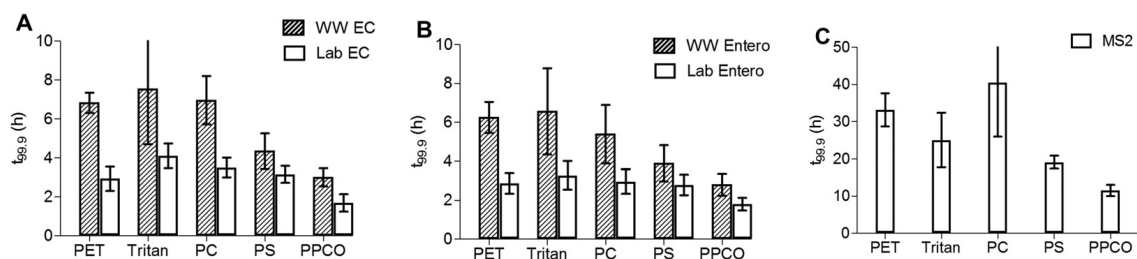
Figure 2.4. Time to reach 3-$\log_{10}$ units of inactivation for (a) *E. coli*; (b) *Enterococcus faecalis*; (c) MS2 coliphage (Fisher et al., 2012).

2.1.4   Action Spectra

Germicidal efficacy varies with organism and with wavelength. A microbial inactivation

action spectrum is used to illustrate the dose of radiation required for a given extent of

inactivation as a function of wavelength (Beck et al., 2015). For comparison across

organisms, action spectra are commonly normalized by defining the response of a given

wavelength relative to the response at 254 nm (Chen et al., 2009). Normalization to 254

nm is also used to determine weighting factors or relative wavelength effectiveness; an

implicit assumption of this approach is that all damage is caused by absorbance of UV

radiation by DNA (Mamane-Gravetz et al., 2005).

The action spectrum for a microbe may also be compared to the absorbance spectrum of

the microbe's DNA, if available, as a means of evaluating the validity of this assumption

(Coohill, 1996). Bernhard et al. (1997) presented a standardized DNA action spectrum

(Equation 2.1). This spectrum is sometimes used when the DNA absorbance spectrum is

not available for an organism. Standardization was determined based on the DNA action

spectrum of Setlow (1974) and the Commission Internationale de l'Eclairage (CIE)

action spectrum for sunburn from McKinlay and Diffey (1987) (Bernhard et al., 1997).

$$A_{DNA}(\lambda) := \left\{ \frac{1}{0.0326} \exp\left[13.82\left(\frac{1}{1 + \exp\left[\frac{(\lambda[nm] - 310)}{9}\right]} - 1 \right) \right], \quad \lambda \leq 370 \ nm \right\} \qquad \text{Equation 2.1}$$

In this equation, λ is the wavelength in nm and $A(\lambda)$ is the action spectrum. At

wavelengths greater than 370 nm the action spectrum is zero, implying that no

inactivation takes place at these longer wavelengths. Equation 2.1 is illustrated

graphically in Figure 2.6, where the blue dotted lines represent the wavelengths of

interest for the experiments in this project. It is important to note that the nucleotide

composition of each organism's DNA differs, resulting in variance among absorbance

spectrum (Chen et al., 2009).
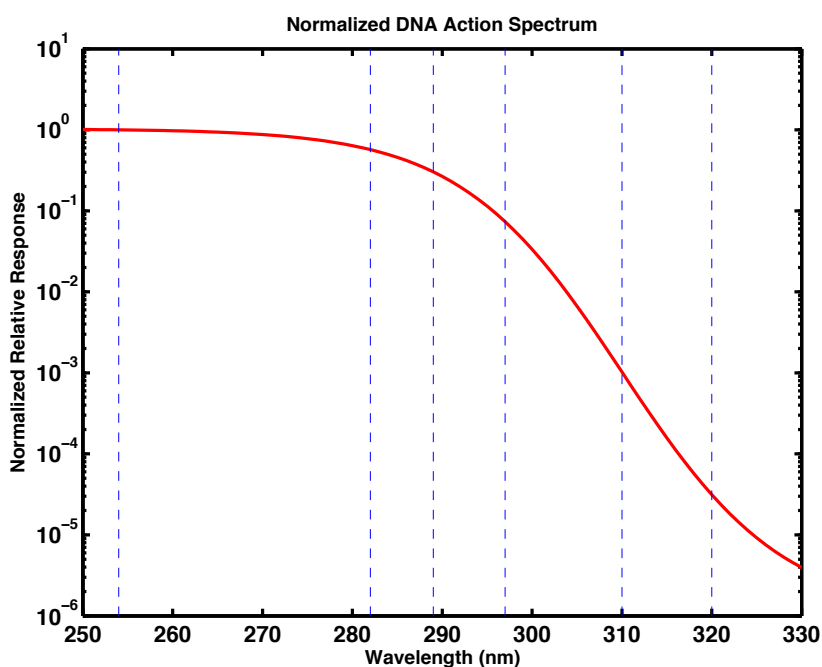
Figure 2.5. Normalized action spectrum for DNA (Bernhard et al., 1997).

Beck et al. (2015) measured action spectra for a range of common waterborne

microorganisms, including *Cryptosporidium parvum,* at wavelengths between 210 nm –

290 nm using a tunable laser. This allowed for isolation of discreet (i.e., monochromatic)

UV wavelengths between 210 nm – 290 nm at intervals of 10 nm. A claim of their work

was that weighting MP doses by action spectra more appropriately described the data

than weighting by DNA absorbance (Beck et al., 2015). However, their data did not

extend into the UVB range.

2.1.5   Effectiveness Spectra

With knowledge of an action spectrum and available UV energy as a function of

wavelength (i.e., spectral irradiance), an effectiveness spectrum can be determined. The

product of spectral irradiance (E_λ) and the DNA action spectrum (A_λ) defines the relative

DNA damage as a function of wavelength for a given source of radiation (Mbonimpa et

al., 2012; Setlow, 1974). Coohill (1996) applied this method to quantify the effects of

stratospheric O_3 depletion on solar UVB damage to plant tissues (Figure 2.6). This

analysis indicated that the majority of plant tissue damage was associated with radiation

in the range of approximately 300 nm $\lesssim \lambda \lesssim$ 310 nm. Depletion of stratospheric O_3

exacerbated this problem.
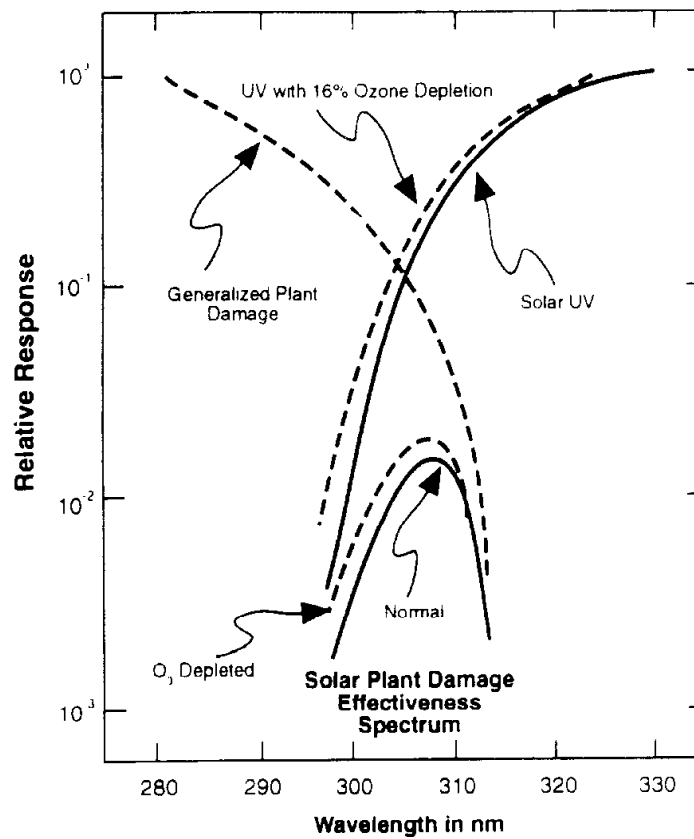
Figure 2.6. Effectiveness spectrum as for plant damage by UVB radiation and the effects of stratospheric ozone depletion (Coohill, 1996).

Mbonimpa et al. (2012) applied a similar approach to illustrate that solar UVB damage to DNA based on mid-day, summer sunlight in West Lafayette, IN was dominated by essentially the same wavelength range (300 nm – 310 nm) (Figure 2.7). These spectra were produced using synthetic solar irradiance spectra from the USDA UVB Monitoring Network and the DNA action spectrum of Setlow (1974) normalized to 290 nm (Mbonimpa et al., 2012). The DNA action from Setlow (1974) is for DNA in human skin, studied for sunburns.
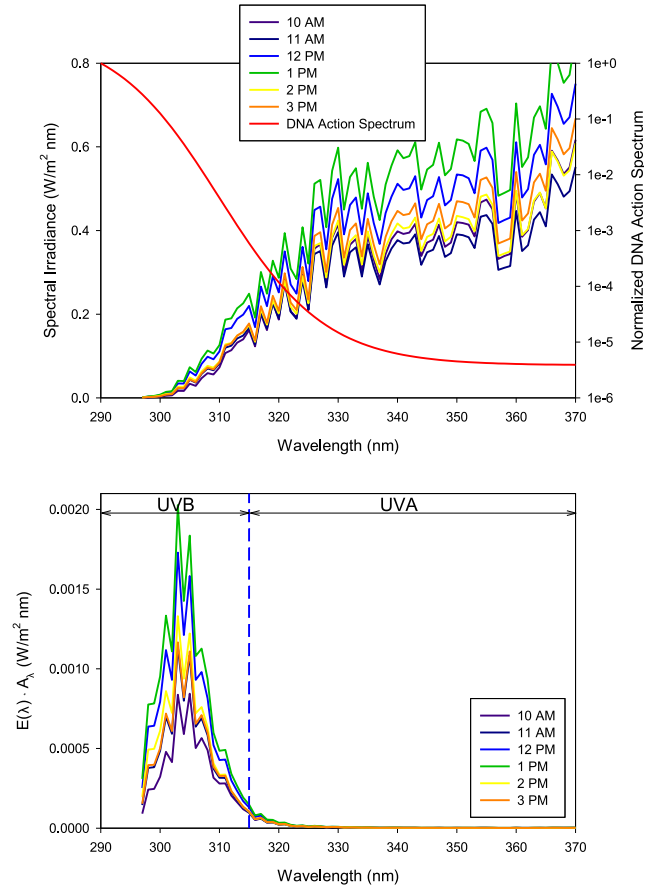
Figure 2.7. Effectiveness spectrum for DNA damage based on the DNA action spectrum of (Setlow, 1974) and synthetic solar spectral irradiance for summer (August) sunlight in West Lafayette, IN (Mbonimpa et al., 2012).

2.1.6 Key Waterborne Pathogens

Salmonella typhimurium LT2

In humans *S. typhi* causes typhoid fever and *S. typhimurium* causes gastroenteritis. When sequenced, *S. typhi* has 98% of the same DNA and 99% of the same amino acids as the *S. typhimurium* strain LT2 (Hooton et al., 2013). Due to the fact that UV disinfection generally relies on DNA and/or protein damage to cause microbial inactivation, these two

strains should respond similarly to UVB exposure (Chen et al., 2009). Therefore, *S. typhimurium* LT2 is hypothesized to represent a (non-pathogenic) surrogate for *S. typhi*. Chang et al. (1985) concluded that *S. typhi* required approximately the same dose of UV_{254} to achieve 3-$\log_{10}$ units of inactivation as other vegetative bacteria, specifically a dose of approximately 7 mJ/cm^2.

Chen et al. (2009) extracted and purified *S. typhimurium* LT2 DNA using a DNeasy$^®$ kit (QUAGEN, Germany), and measured an absorbance spectrum for the extracted DNA. Figure 2.8 illustrates the resulting absorbance spectrum of the DNA.
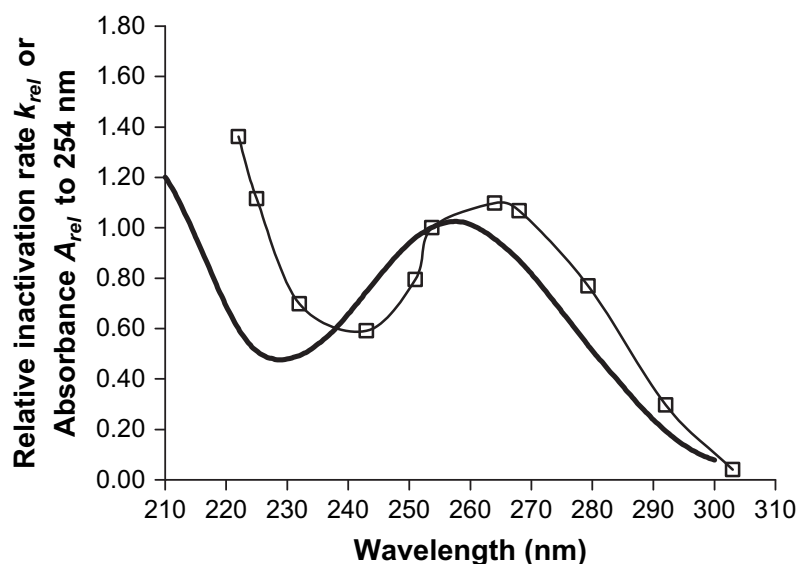
Figure 2.8. Comparison of the DNA absorbance spectrum (solid line) for *S. typhimurium* LT2 with the action spectrum (symbols) (Chen et al., 2009).

Chen et al. (2009) also measured the UV dose-response behavior of *S. typhimurium* LT2
at several wavelengths by using a polychromatic collimated beam and series of narrow
bandpass optical filters. The results of these experiments are illustrated in Figure 2.9.
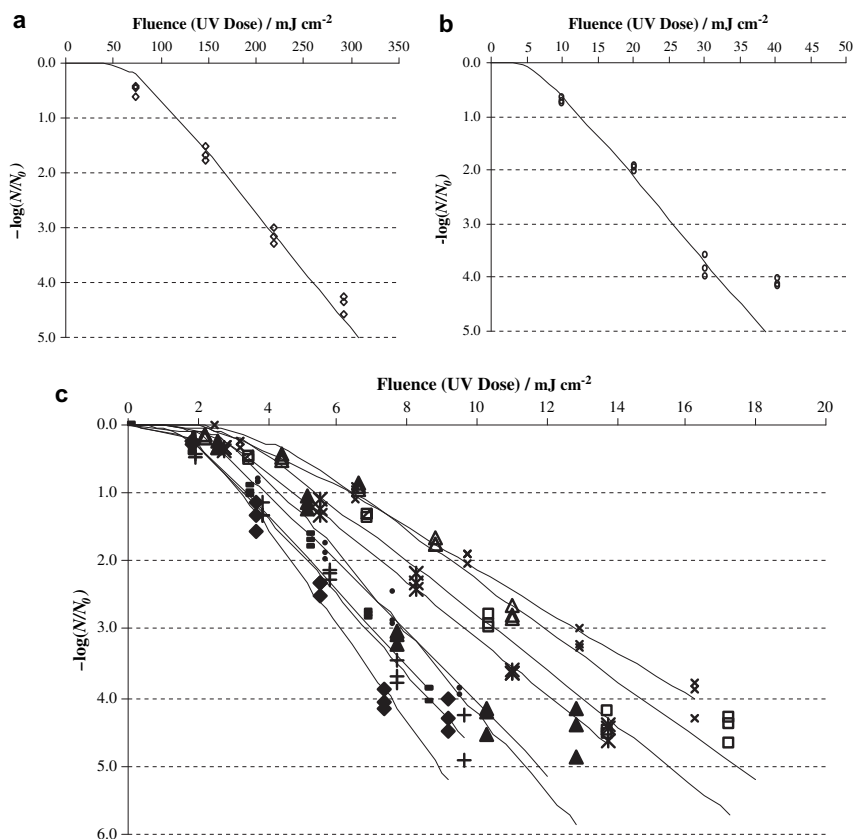
Figure 2.9. Inactivation of *S. typhimurium* LT2 at different wavelengths (a) 292 nm; (b)
303 nm; (c) ◆222 nm, ▲ 225 nm, Δ 232 nm, × 243 nm, * 251 nm, • 254 nm, + 264 nm, −
268 nm, □279 nm (Chen et al., 2009).

The *S. typhimurium* LT2 action spectrum mimicked the absorbance spectrum from the
extracted DNA above 240 nm (Figure 2.8). This similarity to the DNA absorbance
spectrum indicates that the primary mechanism of inactivation involves DNA damage.

However, at roughly 302 nm the DNA absorbance of *S. typhimurium* LT2 DNA approaches zero (Chen et al., 2009).

Chen et al. (2009) also calculated an inactivation rate constant (k) at each wavelength based on the multi-target model. The data were then normalized against the inactivation constant at a wavelength of 254 nm. It was observed (Figure 2.8) that the action spectrum below 230 nm was proportionally greater than the absorbance spectrum, thereby suggesting participation of other biomolecules (e.g., proteins) in inactivation (Chen et al., 2009).

Vibrio cholerae

Vibrio is a genus of bacteria that comprises species that are pathogenic and non-pathogenic to humans. *Vibrio cholerae* is responsible for the disease cholera (Gennari et al., 2012). UV_{254} irradiation causes 1-$\log_{10}$ inactivation at a dose of 2 mJ/cm^2, while 4-$\log_{10}$ inactivation was achieved with 9 mJ/cm^2. This corresponds to an inactivation constant (k) of 1.34 mJ/cm^2 using the single-event model (Hijnen et al., 2006). Other sources have reported 1-$\log_{10}$ unit inactivation after a dose of 1.1 mJ/cm^2 and 2.5-5 mJ/cm^2 for 4-$\log_{10}$ unit inactivation (Das and Das, 1983; Das et al., 1981; Hoyer, 1998). Figure 2.10 illustrates a comparison of the reported UV_{254} dose-response (aka fluence-response) behavior for vegetative cells of *S. typhi* and *V. cholerae*. Like most vegetative cells, they tend to be quite sensitive to UV_{254} exposure.
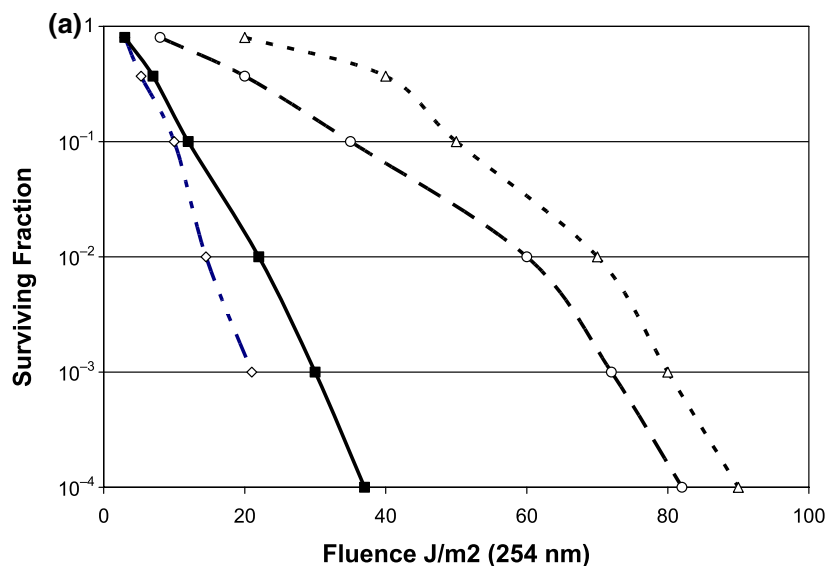
Figure 2.10. Survival of four types of bacteria after irradiation to UV at 254 nm (♦ *Vibrio cholerae;* ■ *Yersinia enterocolitica*; Δ *Salmonella typhi*, ο *E. coli*) (Coohill and Sagripanti, 2008).

The simples model to describe UV disinfection kinetics is the single-event model, in which log-linear dose-response is predicted. Some microbes demonstrate dose-response behavior that can be accurately described by this model (e.g., *Y. enterocolitica* and *E. coli* from Figure 2.10). However, some microbes demonstrate UV dose-response behavior that deviates from the single-event model. Common deviations include lag in inactivation (shouldering) and tailing (see Figure 2.11). The lag is caused by the ability of an organism to accumulate a certain level of damage before it is no longer viable (Coohill, 1994). Tailing behavior has been attributed to particle-association or the presence of a resistant sub-population (Blatchley et al., 2005). It is important to note that just as the linear portion of the curve varies with wavelength, the shoulder may also vary based on the amount of damage required to achieve complete inactivation of the organisms.
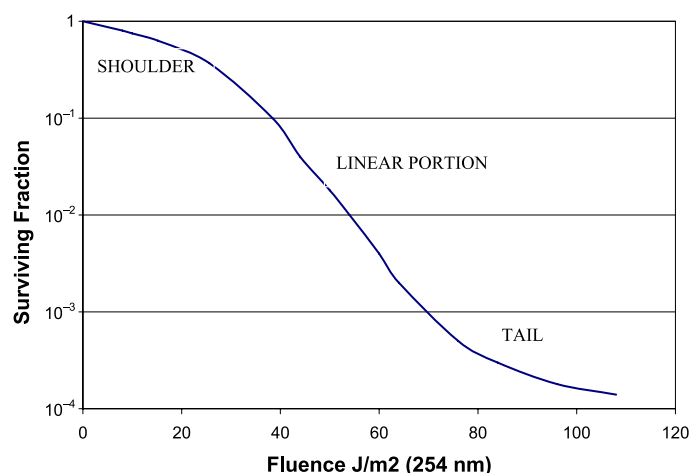
Figure 2.11. Graphical representation of the distinct part of an inactivation curve (Coohill and Sagripanti, 2008).

Cryptosporidium parvum

Infection by the protozoan parasite *Cryptosporidium parvum* can cause acute diarrhea in healthy individuals, but has potentially fatal consequences when the individual is immunocompromised (Rochelle et al., 2002). The oocysts of this parasite have thick walls that make for a resilient form that is often found in surface waters. This resilience allows *C. parvum* oocysts to be largely unaffected by chlorination (2-6 mg/L) at treatment facilities (Rochelle et al., 2002). Even under conditions where multiple barriers were employed, there have been numerous documented outbreaks caused by *C. parvum* (Campbell et al., 1995). The resistance of *C. parvum* to chlorination led to studies of inactivation with UV sources .

Beck et al. (2015) used a laser as the UV source that was tunable at wavelengths between 210 nm – 290 nm to quantify the action spectrum for *C. parvum*. The results are

summarized in Figure 2.12. Dose response experiments at each wavelength were performed in triplicate with each repeat representing an independently run study. All of the axis scales in Figure 2.12 are the same, ranging from a UV dose of 0-4 mJ/cm^2 at each wavelength (excluding 290 nm). The inactivation rate increased from 210 nm to 260 nm at which point, a decrease in inactivation rate was observed with increasing wavelength.
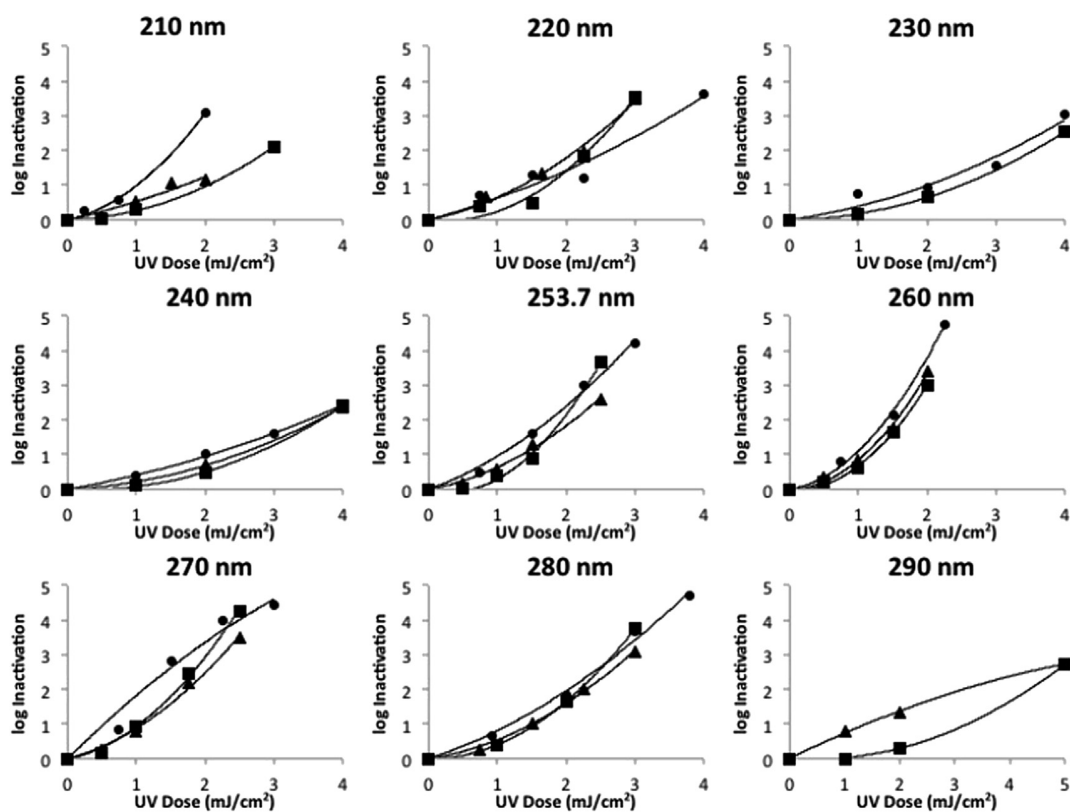
Figure 2.12. UV dose-response behavior of *C. parvum* at wavelengths spanning the UVC range (Beck et al., 2015).

Normalized inactivation constants were determined from the data through a process of

mapping data at each wavelength to a reference wavelength my minimizing the sum of

the least squares between the data and the regression line for the reference data set (253.7

nm). The action spectrum for *C. parvum* is presented in Figure 2.13, based on the data set

illustrated in Figure 2.13. Also included in Figure 2.13 is an action spectrum for *C.*

parvum that was developed by Linden et al. (2001), in which experiments were

conducted over a similar wavelength range using the optically filtered output of a

polychromatic UV source with a UV dose of 2 mJ/cm^2 at each wavelength. The resulting

action spectrum was similar to the spectrum that was developed with the tunable UV

laser for wavelengths ranging from approximately 235 nm to 290 nm. At wavelengths

below roughly 235 nm, substantial deviations between the two action spectra were

observed.
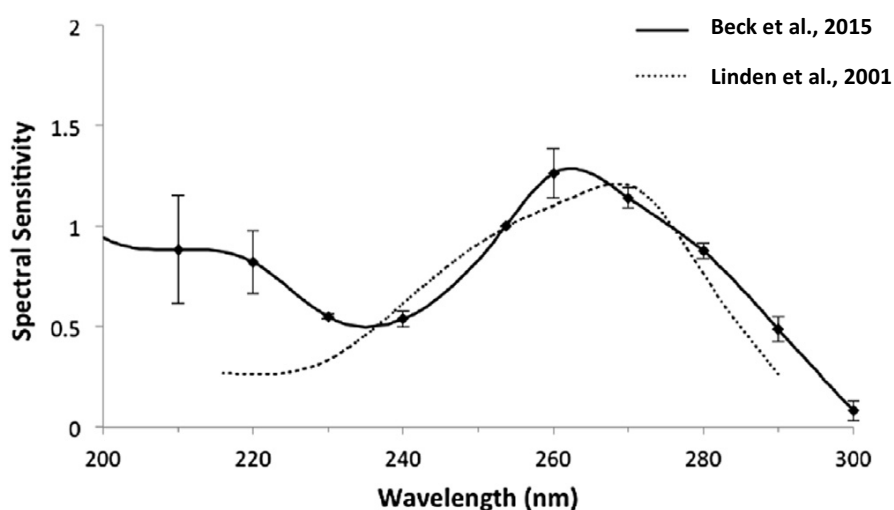
Figure 2.13. UV action spectra for *C. parvum* as presented by Beck et al. (2015) and Linden et al. (2001).

The differences in values below 240 nm were attributed to the UV source and the range of wavelengths emitted. Beck et al. (2015) used a tunable laser, which emitted essentially monochromatic radiation, whereas Linden et al. (2001) used a medium pressure UV lamp used with bandpass filters.

2.1.7   Kinetic Models

Single-Event Model

The single-event model or first-order inaction model is described by Equation 2.2. This model assumes that the inactivation rate (dN/dt) is directly related to the UV dose. The first order inactivation constant is a function of the dose (fluence) of UV radiation delivered to the microbes (Ye et al., 2007).

$$\frac{N}{N_0} = e^{-kD} \hspace{3cm} \text{Equation 2.2}$$

Where,

N = concentration of viable organisms (cfu/mL)

N_0 = concentration of viable organisms prior to UV exposure (cfu/mL)

k = first order inactivation constant (cm^2/mJ)

D = dose of UV radiation (mJ/cm^2).

Multi-Target Model

The multi-target model is described by Equation 2.3. The fundamental assumption of this model is that one or more critical targets within an organism must be damaged before inactivation is observed. When more than one critical target exists, a shoulder will be evident in the dose-response behavior. This is accounted for in the term *n*, implying that there are a finite number of critical targets (Severin et al., 1983).

$$\frac{N}{N_0} = 1 - (1 - 10^{-kD})^n$$
<div align="right">Equation 2.3</div>

Where,

N = concentration of viable organisms (cfu/mL)

N_0 = concentration of viable organisms prior to UV exposure (cfu/mL)

k = first order inactivation constant (cm^2/mJ)

D = dose of UV radiation (mJ/cm^2)

n = number of critical targets.

The multi-target model reduces to the single-event model when n = 1. The multi-target model was used by Chen et al. (2009) to fit dose-response data for *S. typhimurium* LT2.

Series-Event Model

Dose-response behavior for microorganisms yielding a shoulder can also be evaluated based on series-event model. This model is based on the assumption that organisms must

accumulate discreet units of damage above a critical threshold before they are inactivated. Blatchley et al. (2005) used this model (Equation 2.4) to fit dose-response curves for *Bacillus anthracis* and *Bacillus cereus* spores.

$$\frac{N}{N_0} = exp(-kD) \sum_{i=0}^{n-1} \frac{(kD)^i}{i!}$$

Equation 2.4

N = concentration of viable organisms (cfu/mL)

N_0 = concentration of viable organisms prior to UV exposure (cfu/mL)

k = inactivation rate constant (cm^2/mJ)

D = dose of UV radiation (mJ/cm^2)

n = threshold number of damage events required for microbial inactivation

i = index.

Mapping Approach

A mapping approach was proposed by Sutherland (2002) and Coohill (1991), and further applied by Beck et al. (2015) for MS2, T1UV, Q Beta, T7, and T7m Coliphages, *Bacillus pumilus* and *C. parvum*. At each wavelength, a polynomial fit to dose-response data (Equation 2.5) was applied at a reference wavelength (i.e., 253.7 nm).

$$\log_{10} \frac{N}{N_0} = A \cdot D + B \cdot D^2$$

Equation 2.5

Where,

N = concentration of viable organisms (cfu/mL)

N_0 = concentration of viable organisms prior to UV exposure (cfu/mL)

D = dose of UV radiation (mJ/cm^2)

A, B = constants.

At each wavelength, an inactivation constant (k) was identified as a weighting function that was required to "map" the dose-response curves to the curve at 253.7 nm. This method was applied by minimizing the sum of squares between the experimental data points and the quadratic fit of the data. This mapping method is illustrated in Figure 2.14 where the dose response data for MS2 at 220 nm is mapped onto the dose response for MS2 at 253.7 nm with a weighting factor of 2.37 (Beck et al., 2015).
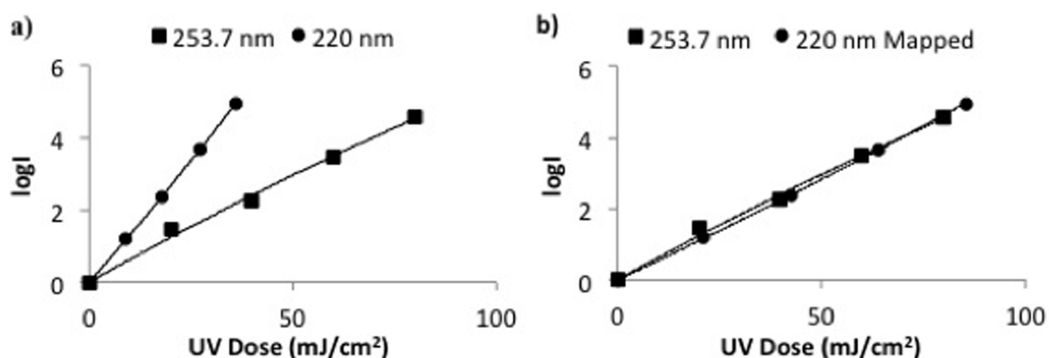
Figure 2.14. Dose response behavior of MS2 coliphage at 220 nm and 253.7 nm (a) experimental results; (b) post-mapping of 220 nm onto 253.7 nm (Beck et al., 2015).

Equation 2.6 (Sutherland 2002) was used to perform this mapping process, where the

weighting function $w(\lambda)$ is equal to the inactivation constant.

$$R\left(\lambda_{ref}, w(\lambda)D\right) = R(\lambda, D) \hspace{4cm} \text{Equation 2.6}$$

Where,

$w(\lambda)$ = weighting function (inactivation constant)

λ_{ref} = 254 nm

D = dose of UV radiation (mJ/cm^2)

R = function for inactivation (log$_{10}$ N/N$_0$).

The product of the weighting function and the dose of UV radiation is the dose of

radiation at λ_{ref} producing the same effect as the dose at another wavelength, λ. This

method is used to infer that at every wavelength tested, the same mechanism is

responsible for inactivation. This can be true when the data from the wavelength of study

can be superimposed on the reference data (Coohill, 1991).

2.2   UV Modeling

2.2.1   Background

The amount UVB radiation received at earth's surface is affected by atmospheric

composition, which is variable by location, as well as the sun's zenith angle. Radiation

with wavelengths, between 280-320 nm will be partially absorbed by ozone, aerosols and

clouds (Chang et al., 2010).Clouds are important because they scatter solar radiation, and they are difficult to model. Scattering can be observed in the diffuse radiation signal from monitoring devices (USDA, n.d.). To predict the performance of a disinfection system based on solar UVB radiation, it is important to understand these parameters and their effects on solar radiation.

2.2.2   USDA UVB Monitoring Network

In partnership with Colorado State University, the United States Department of Agriculture (USDA) has developed a UVB Monitoring and Research Program, where a network of UVB monitoring stations have been established. Their locations, which extend outside of the United States through collaborators, are illustrated in Figure 2.15. Ultimately, the goal of this program is to establish a network that spans the United States with one monitoring location every 5° latitude x 10° longitude (Wang et al., 2008). The site at the Purdue University Agronomy Farm in West Lafayette, Indiana was used most often throughout this work.
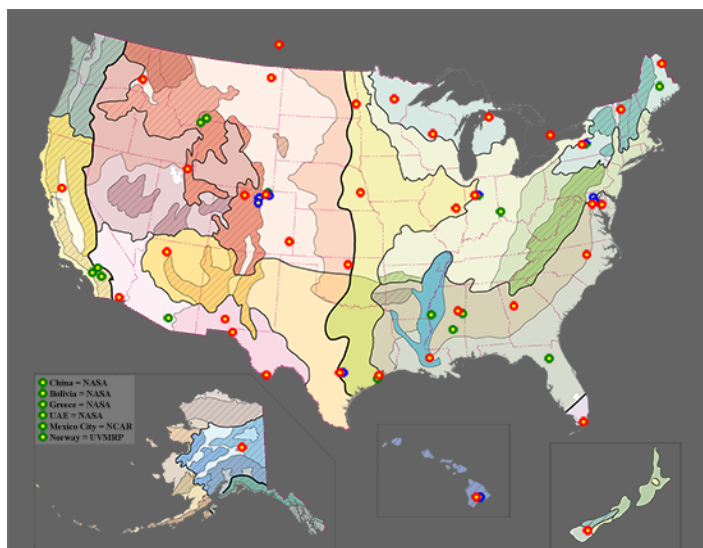
Figure 2.15. Locations of UV-B monitoring sites (red – climatological locations, blue - long term sites, green – short term sites) (USDA, n.d.).

All of the instruments in the network are mounted the same way (1.5 m above the ground level) and processed on a central data server for consistency (Wang et al., 2008). Data from the network are collected, sunrise to sunset, by a Multi-Filter Rotating Shadow-band Radiometer (MFRSR) in the UV and visible ranges. Factors that affect the accuracy of measurements from this instrument include calibration with the aerosol optical depth (AOD), instrument alignment, as well as tilt and accuracy of the angular response as a result of the instrument shape. The error in measurements of optical depth alone can be almost 1% (Figure 2.16), and this error is compounded by other factors (Alexandrov et al., 2007). Factors that affect the readings from the system most significantly are ozone, cloud cover and aerosols (Wang et al., 2008).
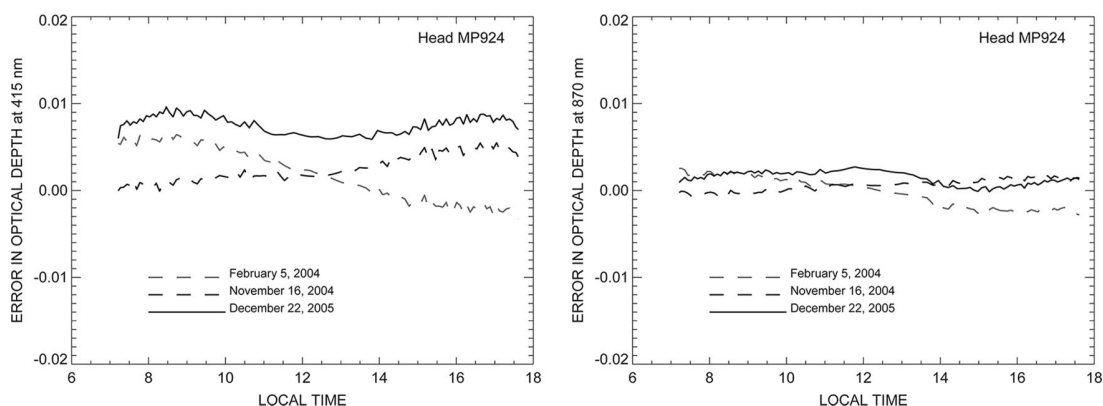
Figure 2.16. Error throughout the day in measurements of optical depth (Alexandrov et al., 2007).

A synthetic spectrum can also be generated from these data using an interpolation algorithm that was developed for the USDA Monitoring Network. Synthetic spectra were used in the work of Mbonimpa et al. (2012) for modeling reactor performance. Synthetic spectra can be generated for each of the test sites within the USDA UVB Monitoring Network for wavelengths between 297 nm – 370 nm in increments of 1 nm (USDA, n.d.).

2.2.3   Tropospheric Ultraviolet & Visible Radiation Model

The Tropospheric Ultraviolet & Visible (TUV) Radiation Model (version 5.2) was downloaded from the National Center for Atmospheric Research (NCAR). This model can be used to simulate surface UV spectral irradiance by accounting for scattering and absorption of solar UV travelling to earth's surface based on atmospheric composition (Madronich et al., 2011). Input data for atmospheric ozone and scattering aerosols can be retrieved from NASA's Ozone Monitoring Instrument (OMI). Atmospheric O_3 strongly

influences tropospheric spectral irradiance in the UVB range; a 0.25% increase in UVB irradiance will result for every Dobson unit (DU) decrease in the ozone column (Ghude et al., 2008). Aerosol data can also be obtained from the Aerosol Robotic Network (AERONET) stations, but are limited in availability and not spatially matched to the ozone data sourced from OMI (Buntoung and Webb, 2010). Other inputs to the TUV model include surface elevation, time zone, longitude and latitude, which were all specific to input location.

In a study conducted by Greenfield et al. (2012),TUV was used to understand the effects of solar UVB radiation on measures of vitamin D3. OMI was used as a data source for atmospheric total ozone and total nitrogen dioxide (NO_2), while the European Centre for Medium-Range Weather Forecasts (ECMWF) was used as the source of surface albedo data. Results were obtained for wavelengths from 280 nm to 315 nm, but they were not compared to measured UVB data for model validation (Greenfield et al., 2012).

Wang et al. (2006) compared measurements from a MFRSR and a UVB-1 broadband radiometer to simulated TUV results as well as results from a synthetic model developed for their study. Pawnee, Colorado was chosen for evaluation because it is part of the USDA UVB monitoring network. Figure 2.17 illustrates the results of this comparison. The TUV model consistently under-estimated erythema-weighted irradiance. The wavelengths taken into account were 200, 305, 311, 317, 325, 323 and 368 nm (Wang et al., 2006).
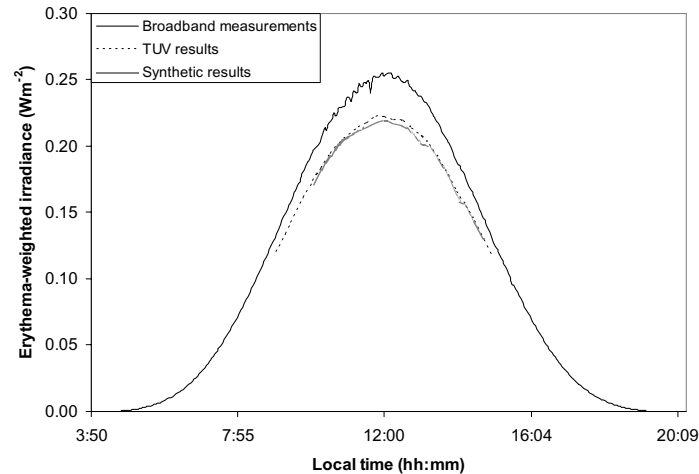
Figure 2.17. Comparison of broadband measurements using UVB-1 broadband monitor to TUV simulations and synthetic analytical results on June 1, 2006 in Pawnee, Colorado (Wang et al., 2006).

2.3   Raytracing

2.3.1   Background

Photopia (LTI Optics, Westminster, CO) is raytracing software package developed for

photometric analysis of optical systems. This program is CAD based and allows users to

design a 3-dimensional system and assign objects within the computational domain with

reflective, refractive and transmissive properties to allow for photometric analysis (Yu et

al., 2014). Modeling with Photopia has been used to study solar energy collection in CPC

reactors (Su et al., 2012b), fiber optic solar lighting (Han et al., 2013) and admitted light

into dimly lit spaces (Oh et al., 2013).

In the study by Su et al. (2012), a mirror CPC was compared to a solid and lens-walled

CPC which were being used to increase the effectiveness of standard, flat PV systems. A

CPC was selected due to its non-tracking and low cost characteristics. The three CPCs,

represented in Figure 2.18, each had a concentration ratio of 2.5 relating to a half

acceptance angle of 23.5^o in the mirror CPC (a), 36.5^o in the solid CPC (b) and 30° in the

lens-walled CPC (c) (Su et al., 2012b). The concentration ratio is defined as the aperture

size of the CPC divided by the area of the receiver (Mbonimpa, 2010). The mirror CPC

was made of aluminum reflector material on the interior, while the solid CPC was filled

with dielectric material (acrylic) and the lens-walled CPC utilized the same dielectric

material to form a lens inside the CPC (Su et al., 2012a, 2012b).
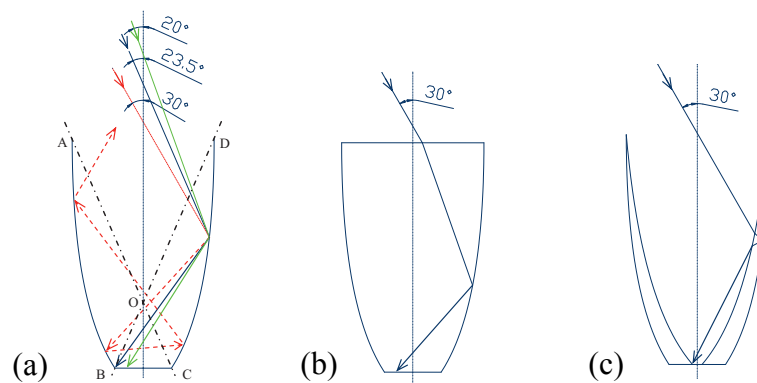
Figure 2.18. Comparison of light travel in different types of CPC reactors (a) mirror CPC (b) solid CPC (c) lens-walled CPC (Su et al., 2012b).

Solar radiation can be simulated in Photopia using a flat lamp source with output

characteristics that match local ambient solar radiation. When rays enter the CPC at an

incident angle less than or equal to the half acceptance angle, they will be directed to the

focal point of the CPC. The model can be used to illustrate the path of ray traces as a

means of illustrating radiation focusing by the CPC (Figure 2.19), the model can also be

used to quantify photometric output.
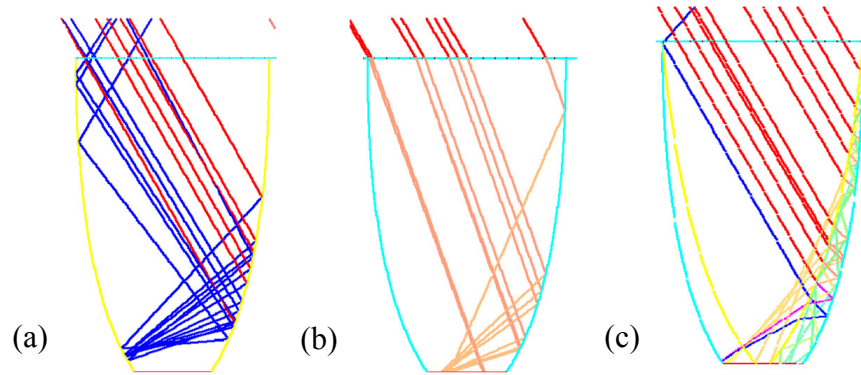
Figure 2.19. Raytracing in different types of CPC reactors (a) mirror CPC (b) solid CPC (c) lens-walled CPC (Su et al., 2012b).

The mirror CPC will not focus radiation on the base of the system when the incidence angle is greater than the half acceptance angle seen in Figure 2.19 (a). At the same concentration ratio, the solid CPC (Figure 2.19 (b)) focuses the rays more to the bottom of the CPC based on differences in the refractive index of the material, indicating the importance of specifying material properties in Photopia. The lens-walled CPC (Figure 2.19 (c)) focuses different incident rays on different points at the bottom of the reactor based on the portion of the lens with which that the ray comes into contact. This results in a wider angle of acceptance for the lens-walled CPC with less optical efficiency (Su et al., 2012b).

CHAPTER 3. ORGANIZATION OF STUDY

The research described herein comprises a combination of laboratory experiments and numerical simulations that were conducted to support the development of community-scale, continuous-flow, solar UV disinfection systems. Laboratory experiments were conducted to quantify action spectra for three microorganisms that are associated with waterborne illnesses in developing countries. Data from the USDA UVB Monitoring Network station at several locations including, the Purdue Agronomy Farm, were evaluated. The TUV model was used to simulate solar spectral irradiance at corresponding locations and times of data collection, thereby allowing direct comparisons of TUV model output with measured (or interpolated) data. In turn, these results were integrated with action spectra for each microbe to allow calculations of effectiveness spectra. The results of these calculations allowed identification of the range of wavelengths that was most effective for inactivation of microbial pathogens by exposure to solar UV radiation. This information was then used to assign input data for raytracing simulations of solar UV amplification by an existing CPC prototype (Mbonimpa et al., 2012). Raytracing simulations allowed definition of the fluence rate distribution within the transmission tube of the CPC reactor system. These results will inform the future design of community-scale CPC reactor systems.

CHAPTER 4. UV DOSE RESPONSE STUDIES

4.1   Introduction

Salmonella typhimurium LT2

S. typhimurium LT2 was used as a non-pathogenic surrogate for *S. typhi* (Chen et al., 2009). UV dose-response data for a range of UV wavelengths were fit with the single-event model and the multi-target model used by Chen et al. (2009).

Vibrio harveyi

V. harveyi was used as a surrogate organism for *V. cholerae* because it is non-pathogenic to humans, but responds similarly to UV radiation (Gennari et al., 2012). *V. harveyi* exhibits a luminescent property due to the presence of the *lux* operon. Samples exposed to UV-irradiation may lose this luminescence as a result of DNA damage (Alifano et al., 2011). Other studies indicate that this is not the case, and the luminescent property may lead to photoreactivation (Czyz et al., 2000; Kozakiewicz et al., 2005). Data from dose-response experiments with *V. harveyi* were fit with the multi-target model.

Cryptosporidium parvum

C. parvum is a protozoan parasite, differing from the two previous organisms studied. This organism infects the human digestive tract and causes the diarrheal disease

Cryptosporidiosis. The protozoan oocysts are typically between 4 μm - 6 μm, and are highly resistant to chlorination and some other forms of treatment (Beck et al., 2015). The mapping approach was used to fit these data for comparison to results presented by Beck et al. (2015).

4.2   Materials & Methods

Bacterial Culturing

Salmonella typhimurium LT2:

An aliquot of *S. typhimurium* LT2 (TL155) was removed from a -80°C freezer and thawed. Frozen cultures were stored in a 1:1 ratio of sample to glycerol. A *S. typhimurium* LT2 culture was maintained and washed with sterile lysogeny broth (LB) consisting of 10 g/L tryptone, 5 g/L yeast extract and 10 g/L sodium chloride in RO water. For washing, the thawed cells were centrifuged for 8 minutes at 7500 x g in an Eppendorf tube. Supernatant was removed and the pellet was re-suspended in 1 mL of LB and centrifuged again. This wash step was repeated an additional time to fully remove any residual glycerol (found in the freezing medium). Following the last wash step, the LB was removed while the pellet was re-suspended and transferred to a sterile flask containing 100 mL autoclaved LB solution. This starter culture was incubated overnight at 37°C while being stirred with a magnetic stir bar and plate, or on a shaker. After incubation, 1 mL of the culture was transferred to a new autoclaved flask of 100 mL LB to inoculate a subculture. Once the subculture reached an optical density of 1.0, 1 mL of sample was removed, centrifuged and re-suspended in 100 mL MSM. This approach yielded a subculture concentration (N_0) of approximately 10^6 cfu/mL.

Vibrio harveyi:

An aliquot of *V. harveyi* (BB120 #300) was removed from a -80°C freezer and thawed. The bacterium was maintained and washed with sterile heart infusion broth (HIB) consisting of 25 g/L HIB and 25 g/L sodium chloride in RO water. The sodium chloride was added to create a saline environment, necessary for this bacterium. For washing, the thawed cells were centrifuged for 8 minutes at 7500 x g in an Eppendorf tube. Supernatant was removed and the pellet was re-suspended in 1 mL of HIB and centrifuged again. This wash step is repeated an additional time to fully remove any residual glycerol (found in the freezing medium). Following the last wash step, the HIB was removed and the pellet was re-suspended and transferred to a sterile flask containing 100 mL autoclaved HIB solution. This starter culture was incubated overnight at 30°C while being stirred with a magnetic stir bar and plate, or on a shaker. After incubation, 1 mL of the culture was transferred to a new autoclaved flask of 100 mL HIB for beginning of the subculture. The subculture was allowed to grow to an optical density of 1.0 before 1 mL was removed, centrifuged and re-suspended in 100 mL MSM. Again, this approach yielded a value of N_0 of 10^6 cfu/mL.

Growth Curve:

A growth curve describes the pace at which a culture grows based on the optical density of the culture, which can be related to the number of cells within the culture through plating at each measurement interval. For both bacteria, the spectrophotometer (DU 800 UV/VIS, Beckman Coulter) was zeroed against growth media in a plastic cuvette. Absorbance of the bacterial subculture was then measured at 30-minute intervals for

absorbance (λ = 600 nm) (Fisher et al., 2008) until the optical density of the solution reached 1.0, corresponding to approximately 10^8 cells/mL. At this point, 1 mL of the subculture was centrifuged to remove any growth media and re-suspended into 100 mL sterile minimal salts medium (MSM) consisting of 0.68 g/L monopotassium phosphate, 2.2 g/L potassium phosphate dibasic trihydrate, 0.1 g/L magnesium sulfate and 1.0 g/L ammonium nitrate, for experimentation. Results were plotted as a function of absorbance (or optical density) vs. time.

Cryptosporidium parvum Infectivity Assay Preparation

Cell Monolayer Preparation:

HCT-8 cells were obtained from the lab of Dr. Arun Bhunia (Purdue University) (ATCC CCL-244) and routinely passaged every 3-4 days. Cells were maintained in Dulbecco's Modified Eagle's Medium (DMEM)/High Glucose supplemented with L-glutamine, sodium pyruvate from HyClone and 10% Fetal Bovine Serum (FBS) from Atlanta Biologicals. Cells were grown in 175 cm^2 flasks, where they attached to the wall of the flask to create a monolayer. For experimentation, the cell monolayer was washed with DMEM by pipetting to remove medium. The monolayer was then detached from the flask by adding 0.25% Trypsin and incubating for 10 minutes at 37°C. Following incubation, maintenance medium was added and pipetted onto the monolayer to remove cells from the flask wall and dilute the trypsin/cell mixture. The cells were transferred to a 10 mL centrifuge tube and centrifuged for 3 minutes at 800 x g. Supernatants were decanted and the cells were re-suspended in maintenance medium by pipetting.

To count the cells, 100 μL of trypan blue were mixed with 100 μL of cell suspension, resulting in a 1:2 dilution. A sample of the cells suspension was added to a hemocytometer chamber by capillary action and cells were counted in the four corner squares of the hemocytometer grid illustrated in Figure 4.1. Trypan blue is only absorbed by dead cells (Sigma-Aldrich, 2010), so cells that were not stained blue were counted.
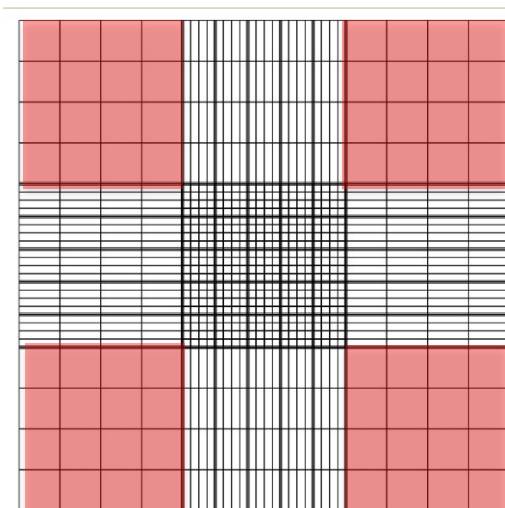
Figure 4.1. Hemocytometer cell used for cell counting where the boxes in red were counted.

The number of cells counted in the four red boxes indicated with the hemocytometer in Figure 4.4 was input into Equation 4.1 for calculation of the total viable cells in the sample per mL of sample based on standard protocol.

$$\frac{Total\ Viable\ Cells}{mL} = \frac{cells\ counted}{\#\ quadrants} \times dilution\ factor \times 10^4 \qquad \text{Equation 4.1}$$

175 cm^2 flasks were seeded at 4.5 x 10^4 cells/cm^2 for two-day passage with 15 mL of

maintenance medium. Cells were placed into 37°C incubator. Two days later, cells were

harvested using the same method as above with 1.25 x 10^5 cells per mL in 50 mL in the

final suspension. 1 mL of this suspension was added to each well of a 48-well plate,

which was incubated at 37°C in 5% CO_2 for 40-48 hours to reach at least 90% confluence

(Sifuentes and Di Giovanni, 2007).

Cryptosporidium parvum preparation:

After 2 days of cell growth, oocysts were prepared for UV exposure and inoculation.

Acidified HBSS/2% Trypsin solution was also freshly prepared by adding 20 mg/L of

trypsin to HBSS at pH 2.0. The target concentration of oocysts was prepared to be 5.4 x

10^5 oocysts/mL in 8 mL of PBS for UV exposure. Samples were centrifuged for 2

minutes at 18,600 x g, and approximately 850 μL of media was aspirated off leaving

oocysts in 150 μL. An equal amount of AHBSS/2% trypsin solution was added (150 μL),

and samples were incubated for 1 hour at 37°C while being vortexed every 15 minutes.

Following this step, 300 μL of PBS was added to the samples at room temperature.

Samples were centrifuged at 18,600 x g for 2 minutes and 550 μL of media was removed

and replaced with 500 μL PBS. This step was repeated and 530 μL were aspirated off and

7980 μL of PBS was added, bringing the final volume of the sample to 8000 μL (Johnson

et al., 2012).

Exposure Studies

UV Source:

Several UV sources were used for exposure microbial suspensions for wavelengths

ranging from 254 nm to 330 nm. All sources used in this study were housed in flat-plate

collimated beam devices to promote uniform, quantifiable dose delivery to microbial

suspensions (Blatchley, 1997). For experiments at 254 nm, a conventional low pressure

(LP) mercury lamp was used. A XeBr excimer lamp was used at 282 nm for *S.*

typhimurium LT2 and *V. harveyi*; this lamp was characterized by an output spectrum with

a peak at 281.6 nm, and a bandwidth of 2.6 nm at half-maximum output (see Figure 4.2).
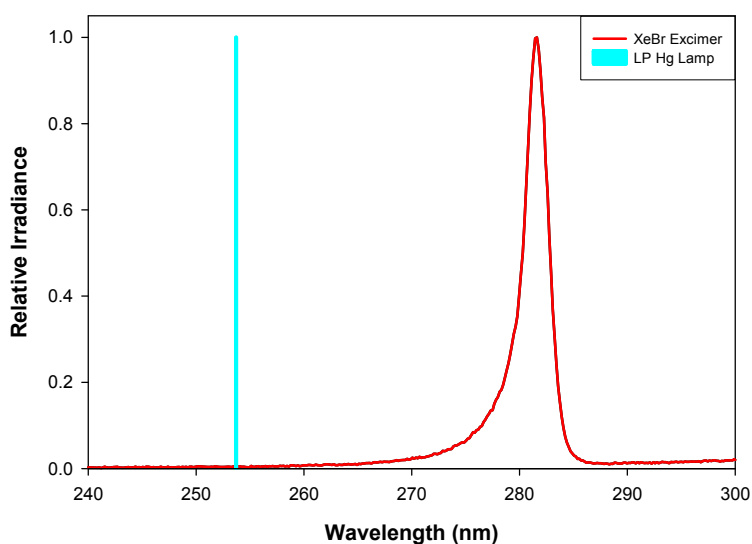
Figure 4.2. Relative UV outputs for LP and XeBr excimer lamps.

At wavelengths greater than 282 nm, a collimated beam with a medium pressure (MP)

mercury lamp was used. Medium pressure Hg lamps are polychromatic, so the collimator

was equipped to accommodate narrow bandpass optical filters (Andover Corporation,

USA) to isolate desired wavelengths. The filters were categorized by their peak

transmittance wavelength for output radiation ranging from 280 nm and 310 nm, Filter

Type 7 was used. For 320 nm and 330 nm, Filter Type 3 was used, with a broader peak of

transmittance. All filters were 50-mm in diameter and 10-nm bandpass. Details of the

bandpass filters including the proper usage orientation, filter types and transmittance

spectra for each are presented in Appendix A.

The UV sources used in this work were evaluated for change in output irradiance over the

course of experiments. The MP lamp optically filtered at 330 nm, varied by less than 2%

in output irradiance over the course of 11 hours. The LP lamp demonstrated variability of

approximately 10% over the course of an hour. The XeBr lamp varied in output

irradiance by an average of 5% over the course of 2 hours. Variability in UV source

output represents a source of error that should be considered when evaluating the

inactivation results, because UV dose was calculated based on an irradiance at the

beginning of each experiment.

Calculation of Exposure Times:

To determine the sample exposure time, average irradiance imposed on a sample must be

calculated using Equation 4.2, which accounts for the effects of reflectance, beam

divergence, beam non-uniformity and absorbance through the depth of the exposed

microbial suspension (Bolton and Linden, 2003).

$$I_{avg} = \frac{I_0(1-R)\left(\frac{L}{L+\ell}\right)P\left(1-e^{-\alpha\ell}\right)}{\alpha\ell}$$

Equation 4.2

Where,

I_{avg} = average irradiance exposed to sample (mW/cm^2)

I_0 = incident irradiance (mW/cm^2)

R = reflection coefficient at wavelength of interest at air:water interface

L = distance from lamp axis to liquid surface (cm)

ℓ = liquid depth in petri dish (cm)

P = petri factor

α = absorbance coefficient for bacterial suspension at wavelength of interest (cm^{-1}).

Incident irradiance was measured using a radiometer (IL1700, International Light) at the same elevation of the sample surface. The petri factor characterizes the light distribution across the petri dish (Linden and Mofidi, 2004); it was assumed to be 1 for all experiments described herein. Transmittance of each microbial suspension used in this work was evaluated at the wavelength of interest using a 1.0 cm quartz cuvette in a UV/Vis spectrophotometer (DU 800 UV/VIS, Beckman Coulter). The absorbance coefficient was calculated with Equation 4.3 using the transmittance of radiation through the sample (T) was measured at the wavelength of interest.

$$\propto = \frac{-\ln(T)}{\ell}$$

Equation 4.3

Where,

α = absorbance coefficient for bacterial suspension at wavelength of interest (cm^{-1})

T = transmittance

ℓ = optical path length of spectrophotometer cell (cm).

Snell's law can be used to quantify reflection and refraction of radiation as it encounters an interface between media with different refractive indexes. For the special case of radiation imposed perpendicular to an interface, Equation 4.4 can be used to calculate the reflection coefficient (R), which represents the fraction of incident radiation that is reflected from the interface.

$$R = \left[\frac{(n_2 - n_1)}{(n_2 + n_1)}\right]^2$$

Equation 4.4

Where,

R = reflection coefficient

n_1 = index of refraction for first medium

n_2 = index of refraction for second medium.

Table 4.1 provides a summary of values of n_1, n_2 and R for an air:water interface at the wavelengths used in this work.

Table 4.1. Reflection coefficients for planar interfaces (air:water) perpendicular to incident radiation at the experimental wavelengths of interest (Edlén, 1966; Schiebener et al., 1990).

Reflection Coefficient Between Air:Water			
Wavelength (nm)	n_{air}	n_{water}	$R_{air:water}$
254	1.0003	1.3764	0.0250
282	1.0003	1.3651	0.0238
289	1.0003	1.3629	0.0235
297	1.0003	1.3607	0.0233
310	1.0003	1.3575	0.0229
320	1.0003	1.3553	0.0227
330	1.0003	1.3534	0.0225

For experiments conducted with the MP lamp, the optical filter was place at the bottom of the collimated beam, approximately 2.5 cm from the sample surface. Target doses (and by extension exposure times) were calculated based on the DNA action spectrum of Bernhard et al. (1997), as well as previously published results for each target organism at 254 nm (Beck et al., 2015; Chen et al., 2009; Coohill and Sagripanti, 2008).

Sample Exposure:

8 mL of sample were added to a 47-mm petri dish with stir bar. The sample was then placed under the center of the collimated beam for the desired exposure time while being continuously stirred. For bacteria samples after exposure, 100 μL of the sample was plated in 1:10 serial dilutions (using MSM) on agar plates. For experiments involving wavelengths between 254 nm and 297 nm, a new sample was added to a petri dish for

each studied dose. Above these wavelengths, long exposure times resulted in one sample being used for continuous exposure for all doses.

All experiments for *C. parvum* were conducted using only one sample continuously exposed due to limited quantities of the protozoa. For experiments involving *C. parvum*, 100 μL of each exposed sample was diluted into inoculation medium (described below), from which 500 μL of each diluted sample was added to the cell cultures.

Viability Assays

Plate Counting:

Plates were incubated for 24-48 hours at 37°C (*S. typhimurium* LT2 on LB agar plates) or $30\,^{\circ}$C (*V. harveyi* on HIB agar plates), and colonies were counted for plates containing between 30-300 colonies (Chen et al., 2009).

Figure 4.3 illustrates dilutions of one sample, from experimental run 1 at 320 nm, exposed to 90 mJ/cm^2 of radiation. The left most sample was the 10^{-1} dilution, and 1:10 serial dilutions were performed and plated until the far right at a dilution of 10^{-5}. The count on the 10^{-4} dilution was used for the inactivation curve because that count was between 30-300. The plate at the third dilution (10^{-3}) should have 10 times more colony forming units (cfu) as the fourth dilution (10^{-4}) and the fifth dilution (10^{-5}) should have 10 times less.

$$10^{-1} \qquad 10^{-2} \qquad 10^{-3} \qquad 10^{-4} \qquad 10^{-5}$$
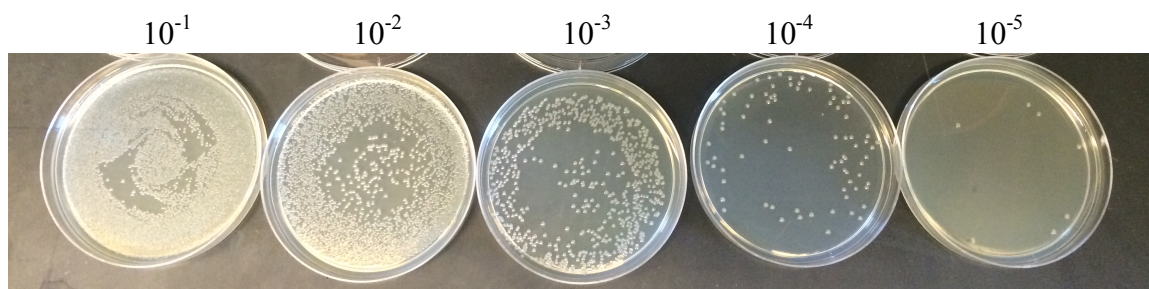
Figure 4.3. Dilutions of *S. typhimurium* LT2 after exposure to 90 mJ/cm^2 of UV radiation at 320 nm. Numerical values above each image indicate dilution ratio for each sample.

The results of an experimental run of *V. harveyi* at 289 nm, where the dilution was held constant across all petri dishes and the UV dose increased from 0 mJ/cm^2 to 33 mJ/cm^2 are illustrated in Figure 4.4. This serves as a visual representation of the data points in the dose response graph at λ = 289 nm, where the number of viable organisms decreased with an increase in exposure to UV radiation.

Figure 4.4. *V. harveyi* after exposure to UV radiation at 289 nm at the same dilution with increasing dose from left to right (0 mJ/cm^2, 13 mJ/cm^2, 26 mJ/cm^2, 33 mJ/cm^2).

Colony counts were recorded and evaluated for inactivation based on the mean of the initial concentration of viable bacteria (N_0), evaluated in triplicate.

C. parvum Infectivity Assay:

After each sample was exposed to a target dose of UV radiation, 1:10 serial dilutions were conducted by removing 100 µL of exposed sample and adding it to 900 µL inoculation medium - DMEM/High Glucose supplemented with L-glutamine, sodium pyruvate, 1% FBS and 200 mg/L bovine bile (King et al., 2012). The monolayer seeding medium was removed from the seeded wells of the 48-well plate row by row to prevent cells from drying out. Each well was then inoculated with the appropriate sample (500 µL inoculum volume). Plates were incubated for 65-72 hours at 37°C and 5% CO_2, to allow infection of the host cells.

To quantify the infected cells, the medium was aspirated off without disturbing the cell monolayers. 250 µL of absolute methanol was added very slowly and gently, drop-wise, to the center of each well with a multichannel pipette and let stand for 10 minutes at room temperature. During this time, 100 µL of SporoGlo (Waterborne, Inc.) was prepared for each monolayer. This preparation requires dilution of the SporoGlo at a ratio of 1:20 into 1% PBS with Tween 20. After 10 minutes the methanol was removed from the wells, and the monolayers were allowed to dry completely, allowing them to attach firmly to the well. This process fixes the monolayers and *C. parvum* preventing further infection and allowing for staining of *C. parvum* life stages (Joe et al., 1998). Once dry, SporoGlo was added to each well and the plate was placed on a rocking platform in a humid environment (container with wet paper towels in the bottom), protected from light. After 45-60 minutes, excess SporoGlo was removed from the wells and they were washed with 200 µL of PBS without disturbing the monolayer. The PBS was removed, and 150 µL

mounting medium was added to each well and then wells were examined under an epifluorescent microscope with a long working distance 20X objective. Infectious foci in each monolayer were counted based off of the criteria published by Johnson et al. (2012).

Infection was defined as at least one focus of life stages in the monolayer, and a focus was defined as at least three life stages within a ≤ 175 μm diameter. Further, a life stage is defined as a stage between 1-10 μm in diameter with the appropriate apple green color and fluorescent intensity (Johnson et al., 2012). Slifko et al. (1997) demonstrated that the number of foci after cell infection is strongly affected by incubation time. After 24 hours of incubation, the focus-to-oocyst ratio increased from 0.5:1 to 1.5:1. This ratio increases to 9.3:1 up to 29.6:1 after 48 hours of incubation seen in Table 4.2 (Slifko et al., 1997). When counting infectious oocysts, this increase in focus-to-oocyst ratio can result in observation of hundreds of life stages associated with one focus.

Table 4.2. Focus-to-oocyst ratio in relation to incubation time (Slifko et al., 1997).

No. of oocysts plated per well	No. of replicate wells or fields[a]		No. of foci counted per well after[b]:		Ratio of foci per oocyst after:	
	24 h	48 h	24 h	48 h	24 h	48 h
1,000	2*	8**	512.00 ± 121.62	13,839.50 ± 5,393.50	0.51	13.8
100	2*	8**	151.00 ± 79.20	2,960.20 ± 3,873.50	1.51	29.6
10	2*	4*	5.50 ± 0.71	93.00 ± 80.50	0.55	9.3
1	2*	4*	<1.00 (NA)[c]	18.80 ± 25.70	<1.00	18.8
0[d]	2*	2*	0.00	0.00	≤1.00	≤1.00

[a] *, wells; **, fields.
[b] Results are given as mean ± standard deviation.
[c] NA, not applicable.
[d] Control.

The number of infectious foci are determined by counting the number of grouped life stages (between 3 to many hundred) in a diameter equal to or less than 175 μm. Figure

4.5 shows an infectious focus, and this image under the microscope would count as 1 focus.
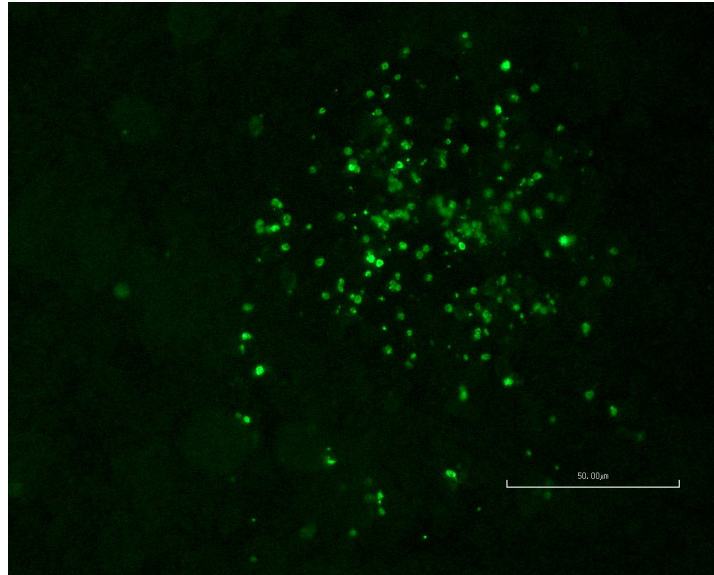
Figure 4.5. Infectious focus made up of many *C. parvum* life stages, stained candy apple green FITC-like SporoGlo (Johnson, 2015).

4.3   Results

Salmonella typhimurium LT2

A growth curve was developed to determine the point at which the absorbance of the subculture reached 1.0, which correlated to 10^8 cfu/mL. To determine this value, the absorbance of three separate *S. typhimurium* LT2 subcultures was measured every 20 minutes, resulting in Figure 4.6.
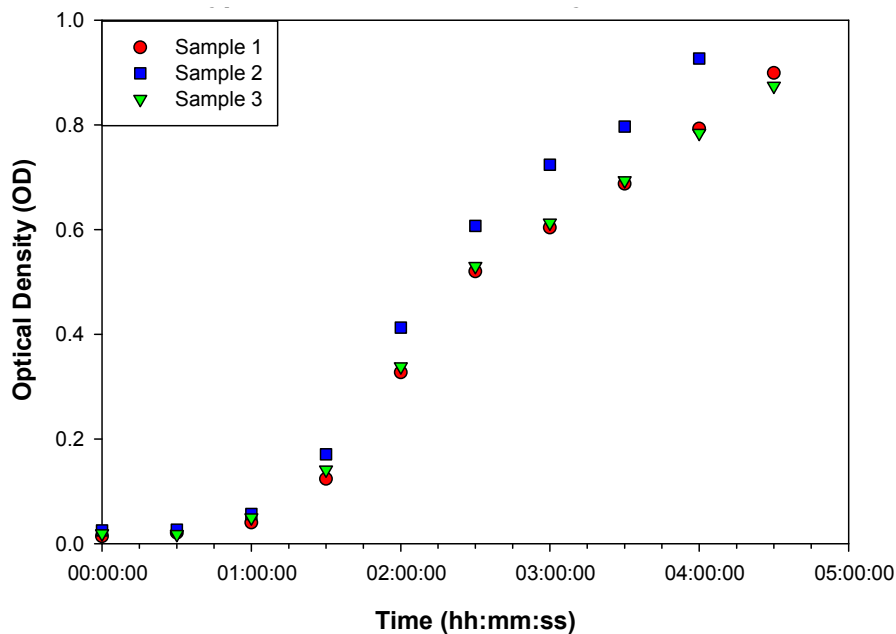
Figure 4.6. Secondary growth curve for *S. typhimurium* LT2.

Samples were plated in triplicate at intervals throughout the secondary growth curve to quantify the number of viable microbial cells as a function of optical density. Results are illustrated in Figure 4.7. An optical density of 1.0 correspond to a viable cell concentration of approximately 10^8 cfu/mL.
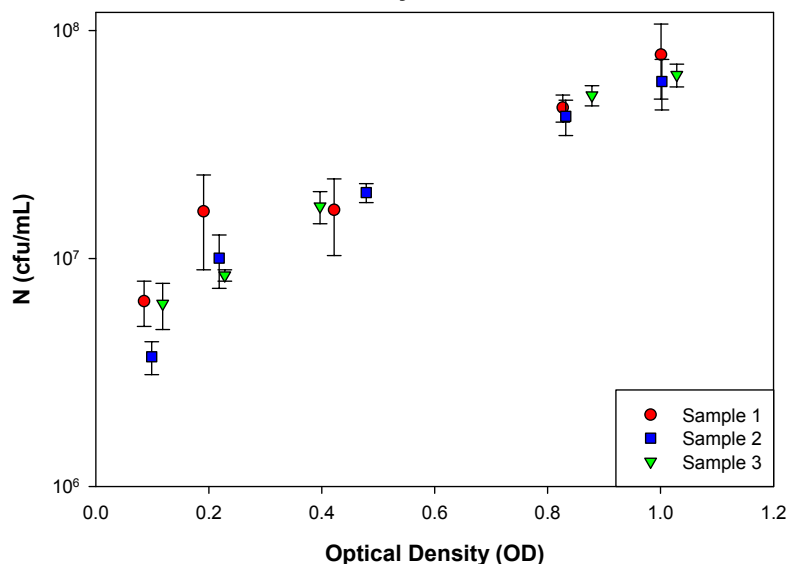
Figure 4.7. Number of viable *S. typhimurium* LT2 colony forming units per mL suspension compared to optical density.

Based on Figures 4.6 and 4.7, the *S. typhimurium* LT2 subculture required approximately 4.5 hours to reach an optical density of 1.0, corresponding to a cell concentration of 10^8 cfu/mL. Therefore, before experimentation, subcultures were incubated for 4.5 hours and then prepared for exposure. After exposure, plating and enumeration, the data were plotted for each wavelength-specific experiment as a function of UV dose. Figures 4.8-4.14 illustrate *S. typhimurium* LT2 dose-response behavior at each wavelength.

The data from these experiments indicated weak evidence of deviation from first-order (single-event) behavior. As such, the data for *S. typhimurium* LT2 were fitted with a single-event model and a multi-target model (Chen et al., 2009). These model fits are also included in Figures 4.8-4.14. A summary of the MATLAB code used to fit the multi-target model is presented in Appendix B. Inactivation constants were estimated from both

models, and normalized to 254 nm. Due to the shoulder constant, an exponential term, in the multi-target model, the inactivation constants were lower before normalization than those developed from the single-event model. For the single-event model, each run was fit with a line and the average of the inactivation constants among the runs was plotted in the following Figures 4.8-4.14. This differs from the method used to fit the multi-target model where all of the data sets at a given wavelength were fit with one curve to establish only one shoulder constant at each wavelength. Without forcing one shoulder constant, the inactivation constants would not be comparable at the same wavelength.

At 254 nm, the inactivation constant from the multi-target model was estimated to be 0.586 cm^2/mJ with a shoulder constant (n) of 3 and an R^2 value of 0.903. With the single-event model, the inactivation constant was 1.231 cm^2/mJ with a standard deviation (σ) of 0.21 cm^2/mJ among the three trials. All wavelengths were normalized to the inactivation in Figure 4.8; therefore, the normalized inactivation constant at this wavelength for both models was 1.0.
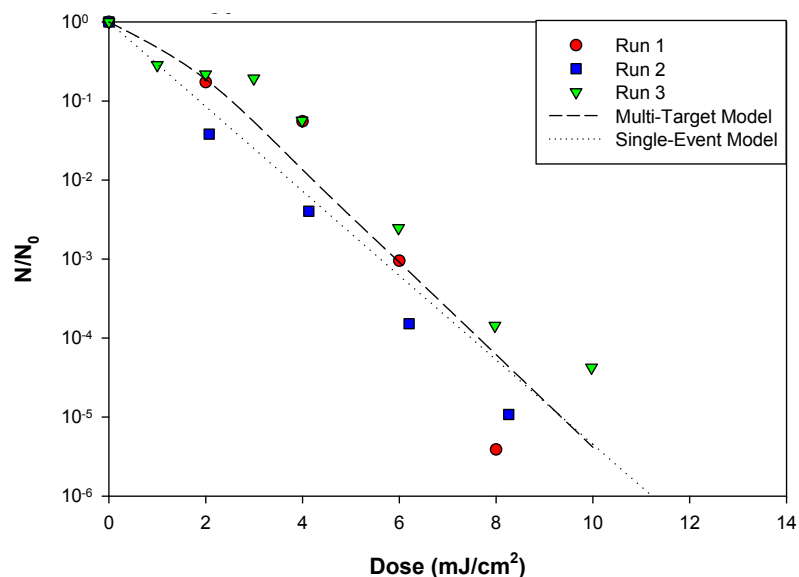
Figure 4.8. *S. typhimurium LT2* dose-response at 254 nm (multi-target model k = 0.586 cm^2/mJ; single-event model k = 1.231 cm^2/mJ).

Figure 4.9 illustrates UV$_{282}$ dose-response behavior. The inactivation constants that were estimated from these data were smaller than those from 254 nm, which is consistent with the absorbance of DNA from *S. typhimurium* LT2 (Chen et al., 2009). Only two runs of this experiment were completed because the lamp was damaged while attempting the third run. The MP lamp did not have a filter at 282 nm, so no further experiments were conducted on *S. typhimurium* LT2 at 282 nm. The inactivation constant at this wavelength from the multi-target model was estimated to be 0.470 cm^2/mJ with a shoulder constant of 6 and an R^2 value of 0.981. With the single-event model, the inactivation constant was 0.872 cm^2/mJ with a standard deviation of 0.03 cm^2/mJ among the three experimental runs. This resulted in normalized inactivation constants of 0.802 and 0.708 respectively.

At 289 nm (Figure 4.10), the multi-target model produced a normalized inactivation constant of 0.341, while the single-event model produced a value of 0.332. The multi-target model yielded an inactivation constant estimate of 0.20 cm^2/mJ with a shoulder constant of 3 and an R^2 value of 0.917, whereas the single-event model yielded an average inactivation constant estimate of 0.409 cm^2/mJ with a standard deviation of 0.074 cm^2/mJ.
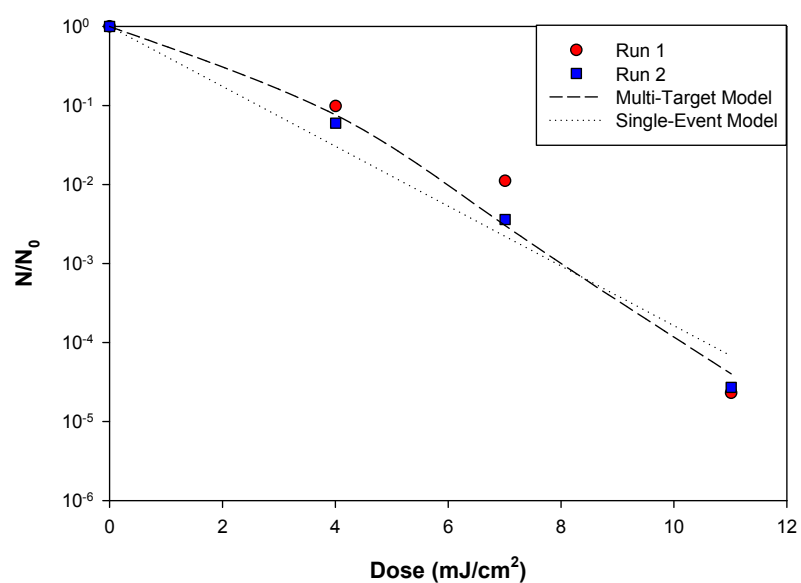
Figure 4.9. *S. typhimurium* LT2 dose-response at 282 nm (multi-target model k = 0.470 cm^2/mJ; single-event model k = 0.872 cm^2/mJ).
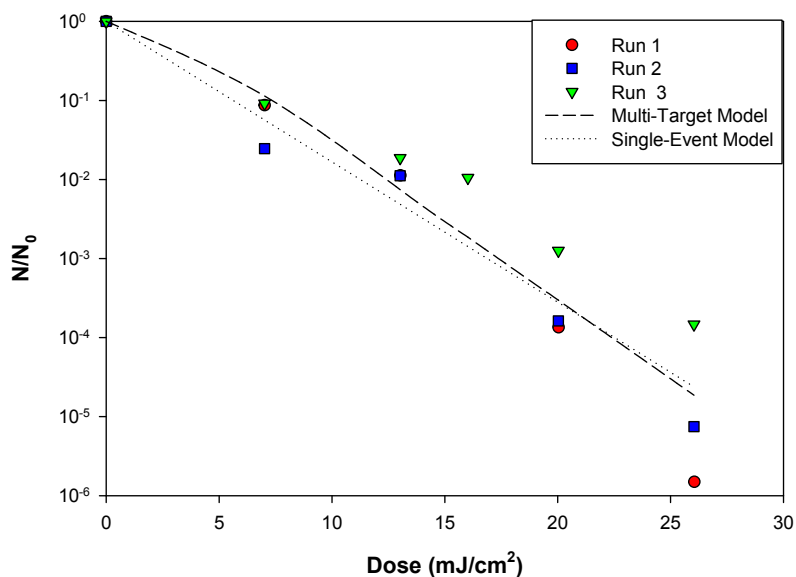
Figure 4.10. *S. typhimurium* LT2 dose-response at 289 nm (multi-target model k = 0.200 cm^2/mJ; single-event model k = 0.409 cm^2/mJ).

Figure 4.11 illustrates the fits of both models for dose-response behavior at 297 nm. With

the multi-target model, the inactivation parameters were k = 0.060 cm^2/mJ, n = 6 and R^2

= 0.963. The single-event model yielded an average inactivation constant estimate of 0.11

cm^2/mJ with a standard deviation of 0.013 cm^2/mJ. The normalized inactivation constants

were 0.102 and 0.089, respectively.
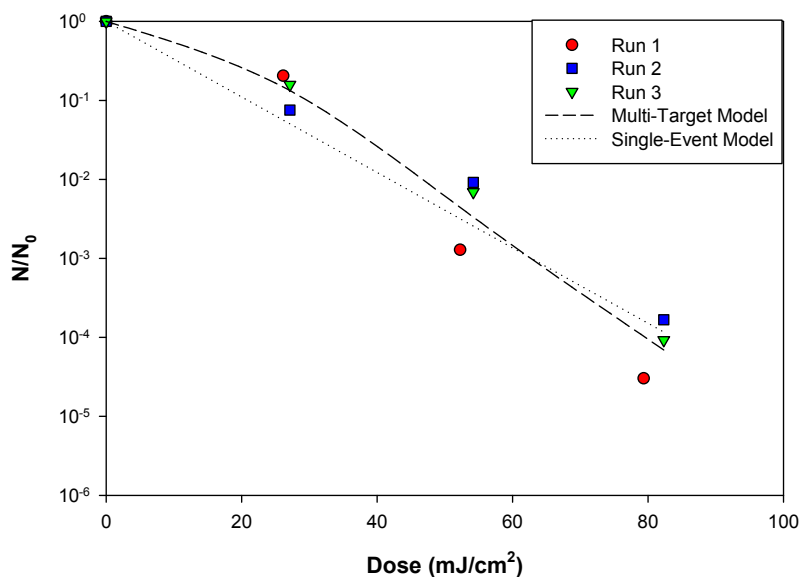
Figure 4.11. *S. typhimurium* LT2 dose-response at 297 nm (multi-target model k = 0.060 cm^2/mJ; single-event model k = 0.110 cm^2/mJ).

No evidence of a shoulder (lag) was evident in the data at 310 nm (see Figure 4.12). This corresponds to a value of n = 1 in the multi-target model. The multi-target model yielded an inactivation constant of 8.0 x 10^{-3} cm^2/mJ with an R^2 value of 0.740. This indicates a relatively poor fit of the multi-target model at 310 nm. A similar trend in the fit of the regression line was not observed for the single-event model where the R^2 values for each individual data set are above 0.9 (R$_1^2$ = 1.0; R$_2^2$ = 0.973; R$_3^2$ = 0.910). Only two usable data points were observed for the first run of the dose-response study at 310 nm at doses of 0 mJ/cm^2 and 388 mJ/cm^2. Target doses used at this wavelength were based off of previously reported DNA action spectrum as reported by Bernhard et al. (1997). Initial target doses for inactivation at 310 nm ranged from 1950 mJ/cm^2 to 19,500 mJ/cm^2. These doses produced unacceptably long exposure times. Therefore, exposure times were limited to four hours, sampling every half hour, corresponding to doses as high as 3110

mJ/cm^2. No colonies were present in samples exposed to more than 388 mJ/cm^2, so

exposure times for the study were shortened to observe the inactivation behavior between

0 mJ/cm^2 and 388 mJ/cm^2. The average inactivation constant was 0.021 cm^2/mJ with a

standard deviation of 7.0 x 10^{-3} cm^2/mJ. The normalized inactivation constants indicated

similarity between the two fits, where the normalized k for the multi-target model was

0.013 and for the single-event model it was 0.017.
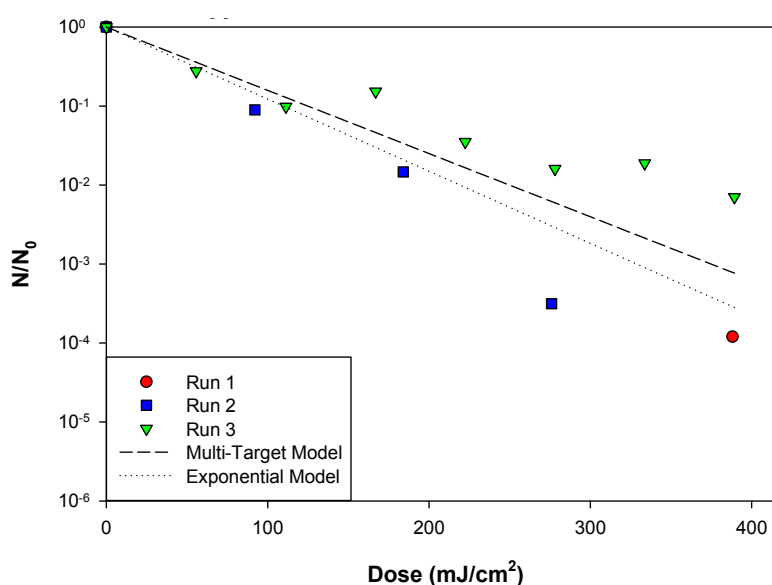
Figure 4.12. *S. typhimurium* LT2 dose-response at 310 nm (multi-target model k = 0.008 cm^2/mJ; single-event model k = 0.021 cm^2/mJ).

The dose-response behavior of *S. typhimurium* LT2 at 320 nm shown in Figure 4.13.

Again, no evidence of a shoulder existed in the data set. The inactivation constant with

the multi-target model was 0.013 cm^2/mJ with an R^2 value of 0.494. The single-event

model yielded an average inactivation constant of 0.034 cm^2/mJ with a standard

deviation of 0.021. Again the individual fits of each data set had a high R^2 value in

comparison to the multi-target model. The R^2 values were all above 0.87 ($R_1{}^2 = 0.914$; $R_2{}^2 = 0.979$; $R_3{}^2 = 0.876$). The normalized inactivation constant was 0.023 for the multi-target model compared to 0.027 for the single-event model.
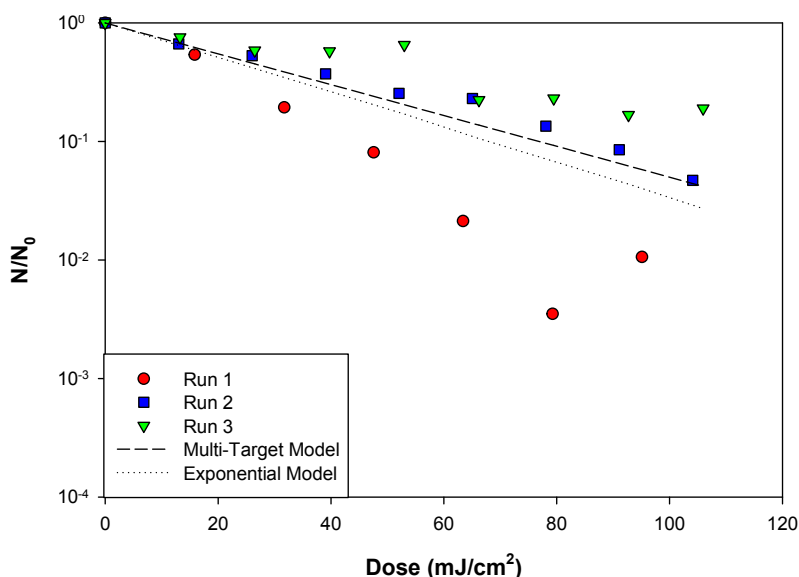
Figure 4.13. *S. typhimurium* LT2 dose-response at 320 nm (multi-target model k = 0.013 cm^2/mJ; single-event model k = 0.034 cm^2/mJ).

Inactivation at 330 nm (Figure 4.14) produced similar results to those observed at 310 nm and 320 nm. Again, no evidence of a shoulder was observed, and the inactivation constant from this model was about half that of the single-event model. The multi-target model fit the data with an inactivation constant of 6.0 x 10^{-3} cm^2/mJ, a shoulder constant of 1 and an R^2 value of 0.594. The single-event model fit the data sets with an average inactivation constant of 0.015 cm^2/mJ with a standard deviation of 8.0 x 10^{-3} cm^2/mJ between runs. The R^2 values for each individual fit of the single-event model were always above

0.94 ($R_1^2 = 0.978$; $R_2^2 = 0.943$; $R_3^2 = 0.957$). The normalized inactivation constant for the multi-target model was 0.011 compared to 0.012 for the single-event model.
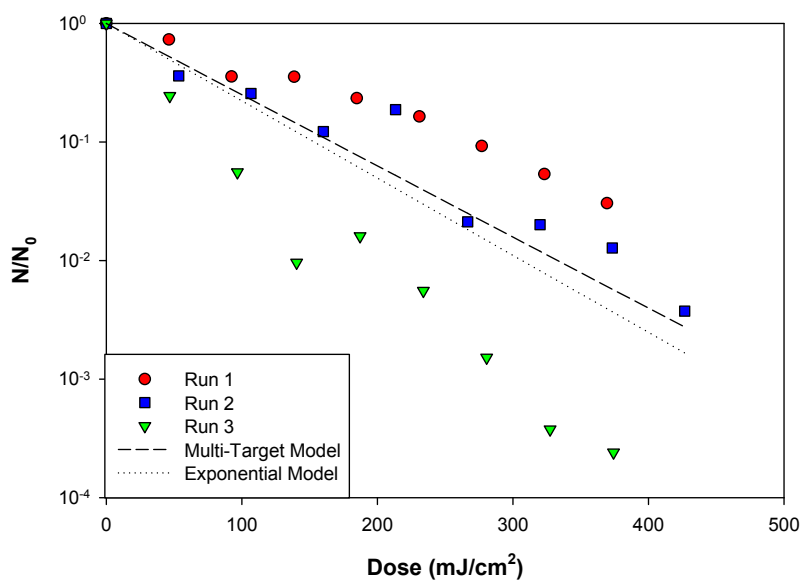
Figure 4.14. *S. typhimurium* LT2 dose response at 330 nm (multi-target model $k = 0.006$ cm^2/mJ; single-event model $k = 0.015$ cm^2/mJ).

Results of the inactivation constants for the multi-target model are summarized in Table 4.3 and the inactivation constants for the single-event model are summarized in Table 4.4. The inactivation constants were then normalized to 254 nm, as seen in the last column of Table 4.3.

Table 4.3. *S. typhimurium* LT2 dose response data for the multi-target model.

S. typhimurium LT2 Dose-Response Data with the Multi-Target Model				
Wavelength (nm)	Inactivation Constant (k) (cm^2/mJ)	n	R^2	Normalized Inactivation Constant (k)
254				
254	0.586	3	0.903	1.000
254				
282	0.470	6	0.981	0.802
282				
289				
289	0.200	3	0.917	0.341
289				
297				
297	0.060	6	0.963	0.102
297				
310				
310	0.008	1	0.740	0.013
310				
320				
320	0.013	1	0.494	0.023
320				
330				
330	0.006	1	0.594	0.011
330				

The normalized average inactivation constant from Table 4.3 can be compared to the normalized inactivation constants from Table 4.2 to understand the differences in model predictions. These normalized inactivation constants were plotted in comparison to previous inactivation studies conducted by Chen et al. (2009), as well as DNA absorbance spectrum obtained in this same study.

Table 4.4. *S. typhimurium* LT2 dose response data for the single-event model.

S. typhimurium LT2 Dose-Response Data with the Single-Event Model					
Wavelength (nm)	Inactivation Constant (k) (mJ/cm^2)	R^2	Average k (mJ/cm^2)	Standard Deviation	Normalized Average k
254	1.304	0.889			
254	1.395	0.997	1.231	0.210	1.000
254	0.995	0.959			
282	0.850	0.920	0.872	0.030	0.708
282	0.893	0.976			
289	0.465	0.920			
289	0.437	0.976	0.409	0.074	0.332
289	0.325	0.986			
297	0.125	0.955			
297	0.100	0.981	0.110	0.013	0.089
297	0.104	0.961			
310	0.023	1.000			
310	0.027	0.973	0.021	0.007	0.017
310	0.013	0.910			
320	0.057	0.914			
320	0.027	0.979	0.034	0.021	0.027
320	0.017	0.876			
330	0.009	0.978			
330	0.012	0.943	0.015	0.008	0.012
330	0.024	0.957			

The multi-target model yielded higher inactivation constants at wavelengths up through 297 nm in comparison to the single-event model. At longer UVB wavelengths, this trend was reversed. This could be due to a decrease in the shoulder constant to 1.0 at the longer wavelengths, resulting in an improved fit of the data from the single-event model. A summary of all data is presented in Figure 4.15.
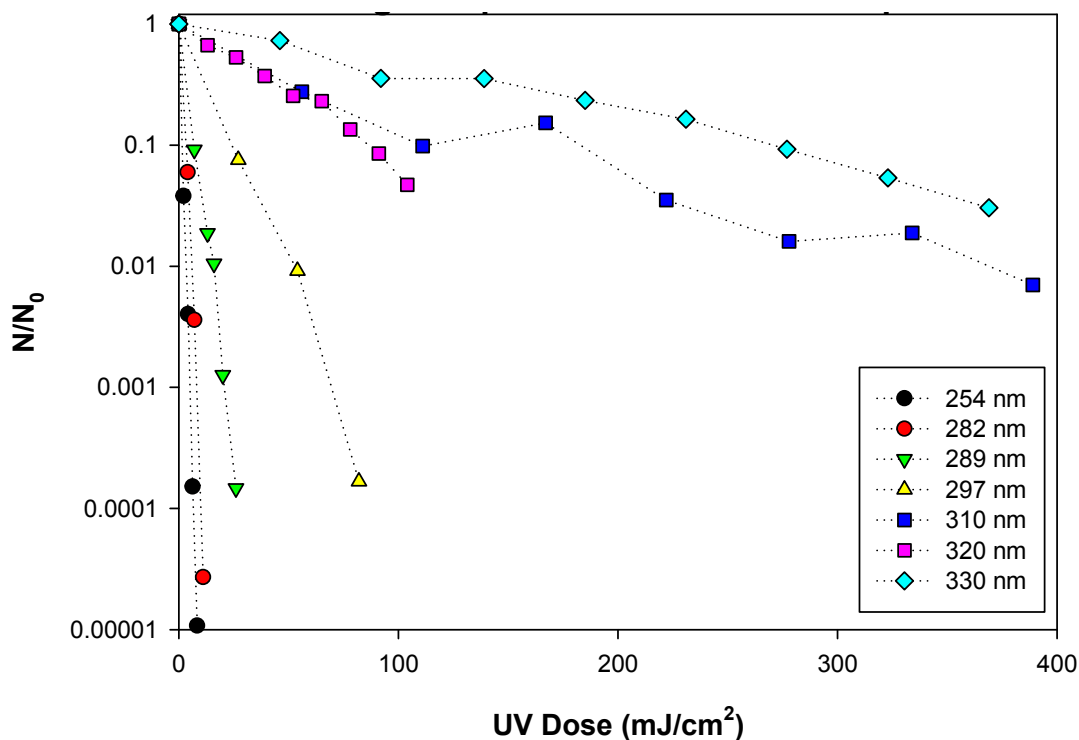
Figure 4.15. Overall comparison of dose-response data for *S. typhimurium* LT2 on the same inactivation and dose scales.

In general, as wavelength increased, the dose required to achieve the same amount of inactivation also increases. This is true for all wavelengths except 320 nm, where bacterial sensitivity was greater than at 310 nm.

Figure 4.16, illustrates normalized action spectra for *S. typhimurium* LT2 from this study compared to results from Chen et al. (2009). The single-event and multi-target models yielded similar trends. Specifically, the action spectra from both models closely followed the DNA absorbance spectrum up to 300 nm. However, the inactivation response at 320 nm was slightly higher than at 310 nm or 330 nm. This suggests involvement of a biomolecule other than DNA, a systematic error in the experiment in this wavelength range, or contribution of UVA effects (i.e., reactive oxygen species and temperature) based on the transmittance spectra of the optical filters.
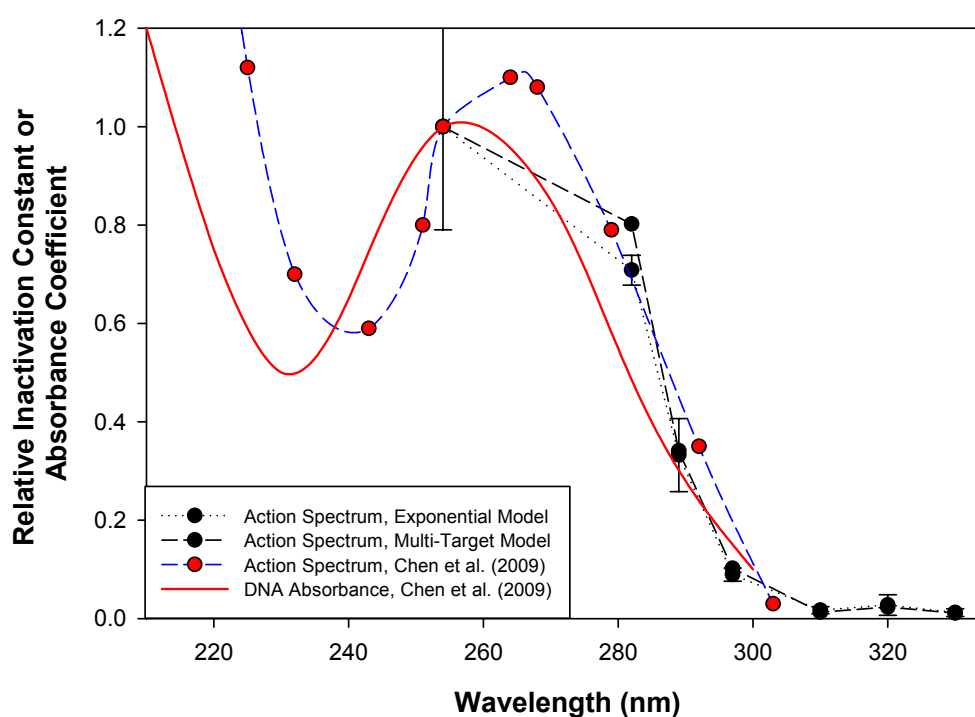
Figure 4.16. Summary of normalized inactivation constants for *S. typhimurium* LT2 compared to the literature for DNA absorbance and previous studies of *S. typhimurium* LT2. Data from the experiments conducted in this work are indicated by black circles; data from Chen et al. (2009), which span wavelengths from 220-300 nm are included for comparison. The DNA absorbance spectrum from Chen et al. (2009) is also included for comparison.

Vibrio harveyi

V. harveyi was grown at 30°C in Heart Infusion Broth (HIB) supplemented with 25 g/L sodium chloride. The original culture was grown for 24 hours at which point a subculture was started by diluting the 24-hour culture 1:100 in HIB. Subculture growth was monitored with absorbance readings at 600 nm (1.0 cm optical path) every 30 minutes. Figure 4.17 represents the growth of the subculture in terms of absorbance as a function of time. Three separate subcultures were grown with the same 1:100 dilution ratio. The target cell concentration for the subculture was 10^8 cfu/mL, which is achieved at an optical density of 1.0.
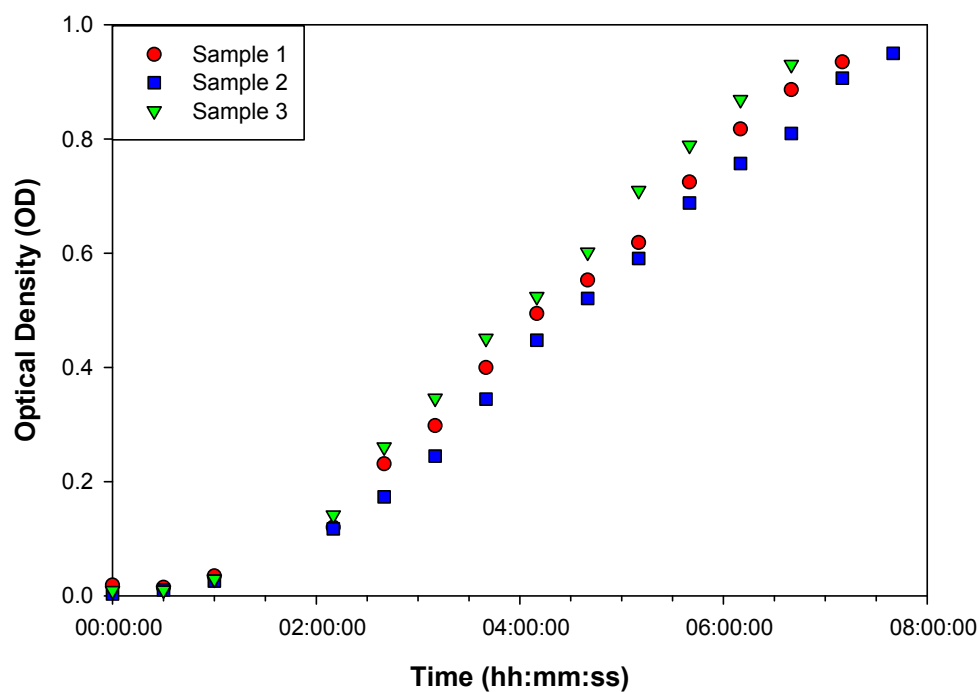
Figure 4.17. Secondary growth curve for *V. harveyi.*

The samples reached an optical density of 1.0 after approximately 8 hours; therefore, in subsequent experiments the subcultures were grown for 8 hours before UV exposure. After 8 hours of subculture growth, the multiplication of bacteria was visually apparent (Figure 4.18).
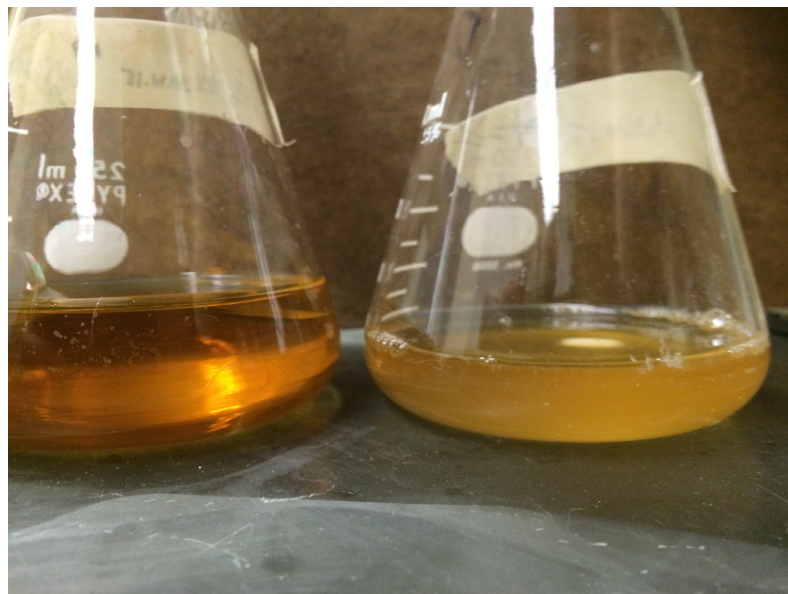
Figure 4.18. Difference in transparency between HIB broth (left) and HIB broth with *V. harveyi* subculture at an OD ~ 1.0 at 600 nm. Incubation time for the sample on the right was 7 hours, 45 minutes.

Sub-samples from the three subculture flasks were transferred into 1.0 cm plastic cuvettes for absorbance readings with the spectrophotometer. The instrument was zeroed ($\lambda = 600$ nm) with a sample of pure HIB. All subcultures were started form the same culture, so they were expected to grow in a similar manner producing comparable optical densities. Figure 4.19 illustrates a blank and three subcultures after 7 hours, 45 minutes of

incubation. Absorbance readings of samples illustrated in Figure 4.19 demonstrated roughly 10% variability.
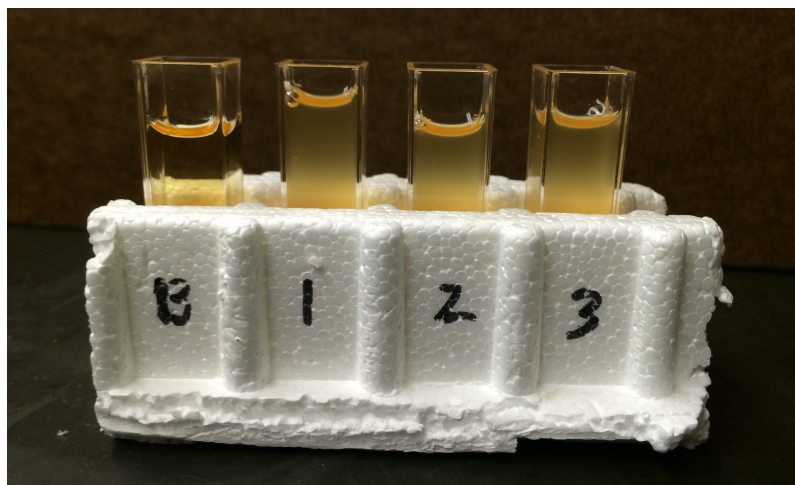
Figure 4.19. Plastic cuvettes with samples of *V. harveyi* subcultures measured for OD after 7 hours, 45 minutes (B) Blank OD = 0; (1) OD = 1.004; (2) OD = 0.95; and (3) OD = 1.05.

The normalized concentration of viable bacteria (N/N_0) are illustrated as a function of average dose for each wavelength in Figures 4.20-4.28. For many of these data sets, a shoulder in the dose-response data was clearly evident. Therefore, the series-event model (Equation 4.3) was fitted to the measurements from triplicate experiments at each wavelength. To determine these inactivation constants, series-event parameters were estimated by non-linear regression of Equation 4.3, while minimizing the residual sum of squares (RSS). The non-linear regression algorithm used for fitting is described in Appendix B.

At 254 nm (Figure 4.20), the series event model with a shoulder constant of 3 produced an inactivation constant of 1.36 cm^2/mJ with an R^2 value of 0.83. All of the dose-response experiments were normalized against this behavior.
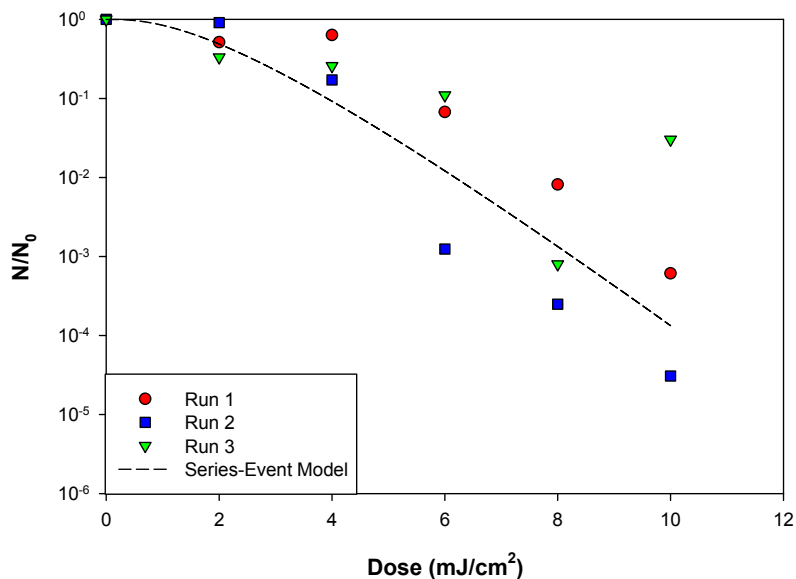
Figure 4.20. *V. harveyi* dose-response at 254 nm (n = 3; k = 1.36 cm^2/mJ).

At 282 nm (Figure 4.21), the dose response experiments produced the same shoulder constant of 3 and an inactivation constant of 0.94 cm^2/mJ at an R^2 of 0.95. The normalized inactivation constant at 282 nm was 0.691.
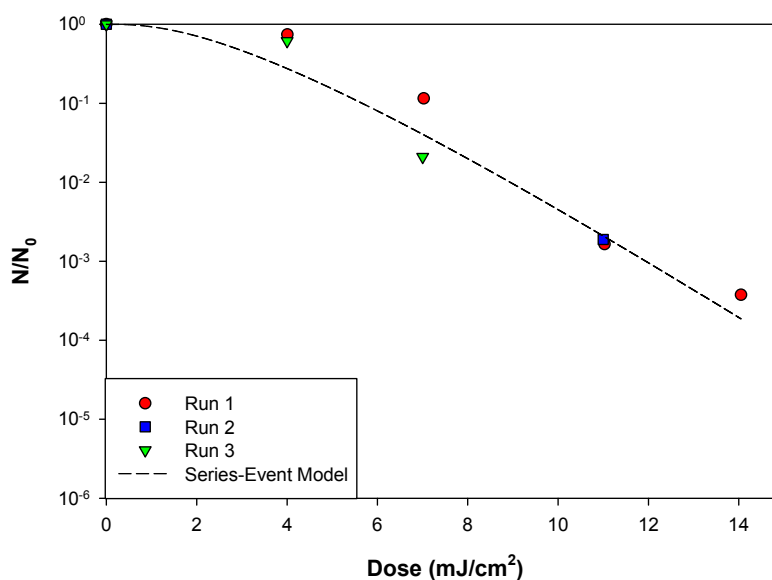
Figure 4.21. *V. harveyi* dose-response at 282 nm ($n = 3$; $k = 0.940$ cm^2/mJ).

Figure 4.22 illustrates measured dose-response behavior and series-event model fit for λ = 289 nm. No evidence of a shoulder was apparent in the data; non-linear regression indicated and estimate of $n = 1$. The regression analysis yielded an inactivation constant estimate of 0.226 cm^2/mJ with an R^2 value of 0.772. Normalized to 254 nm, the inactivation constant was 0.166 cm^2/mJ.

Figure 4.23 illustrates measured dose-response behavior and series-event model fit for λ = 297 nm. The series-event model with a shoulder constant of 3 yielded an inactivation constant of 0.099 cm^2/mJ with an R^2 value of 0.91. The normalized inactivation constant was 0.077.
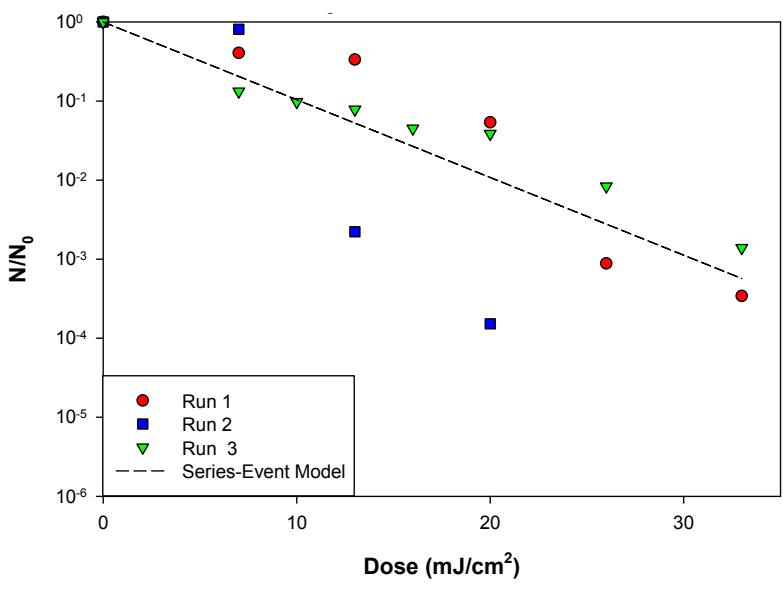
Figure 4.22. *V. harveyi* dose-response at 289 nm (n = 1; k = 0.226 cm^2/mJ).
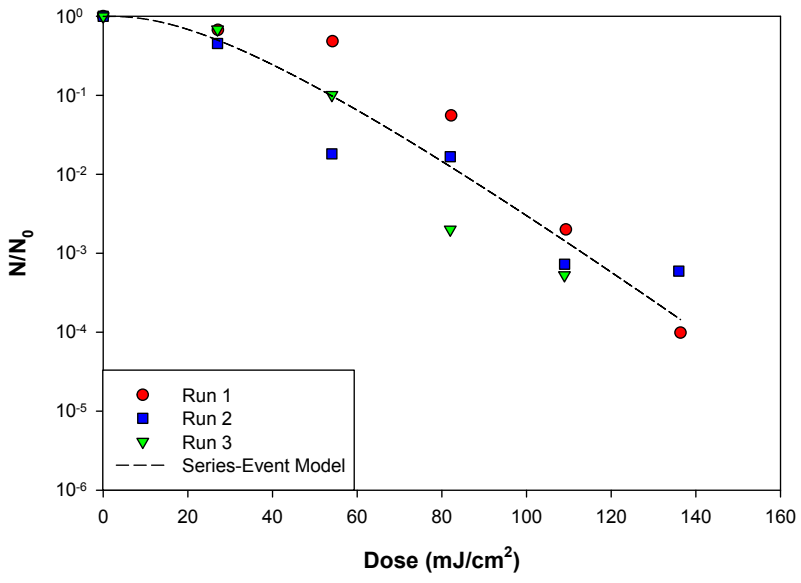
Figure 4.23. *V. harveyi* dose-response at 297 nm (n = 3; k = 0.099 cm^2/mJ).

At a wavelength of 310 nm (Figure 4.24), the correlation between the data and the

regression line decreased, as was the trend with other regression lines with a shoulder

constant of 1. The series-event model with a shoulder constant of 1 produced an

inactivation constant of 0.010 cm^2/mJ with an R^2 value of 0.788. When normalized, the

inactivation constant became 0.01.

.
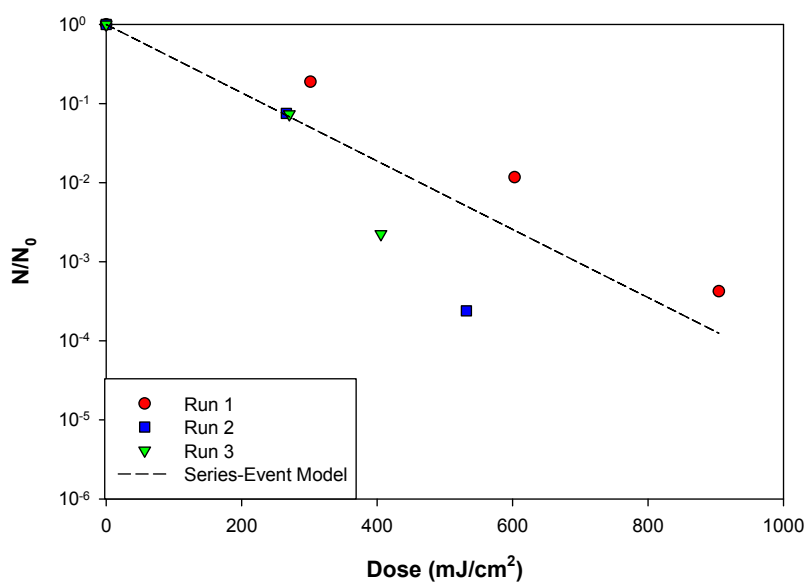
Figure 4.24. *V. harveyi* dose-response at 310 nm (n = 1; k = 0.01 cm^2/mJ).

Figure 4.25 represents the dose-response of *V. harveyi* at 320 nm, where the correlation

of the best fit line to the data is 0.931, almost double of that at this wavelength for *S.*

typhimurium LT2. At a shoulder constant of 3, the inactivation constant was 0.06 cm^2/mJ,

normalized to 0.042. An increase in the normalized inactivation constant is observed here

at 320 nm as compared to 310 nm.
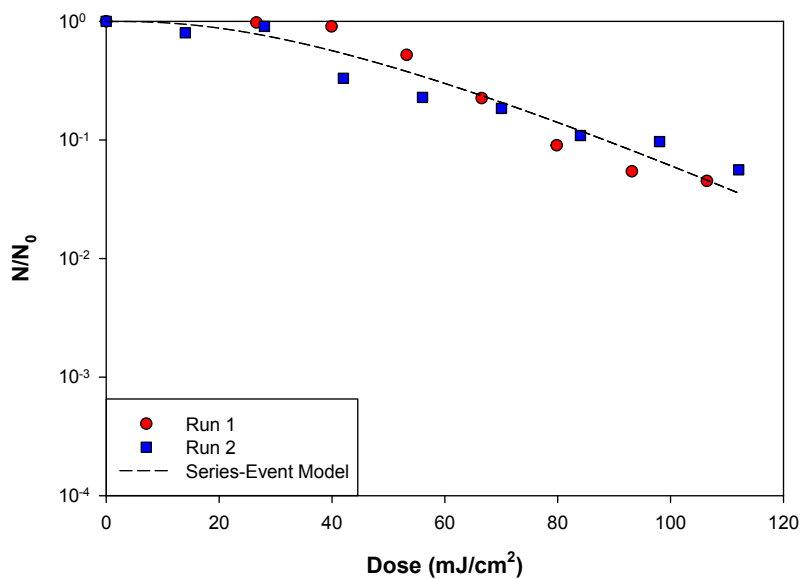
Figure 4.25. *V. harveyi* dose-response at 320 nm (n = 3; k = 0.06 cm^2/mJ).

For 330 nm (Figure 4.26), the series-event model with a shoulder constant of 1 produced an inactivation constant of 3.0 x 10^{-3} cm^2/mJ, which was similar to the behavior observed at 310 nm and an order of magnitude smaller than that at 320 nm. The R^2 value was 0.85, and the normalized inactivation constant was 0.073.
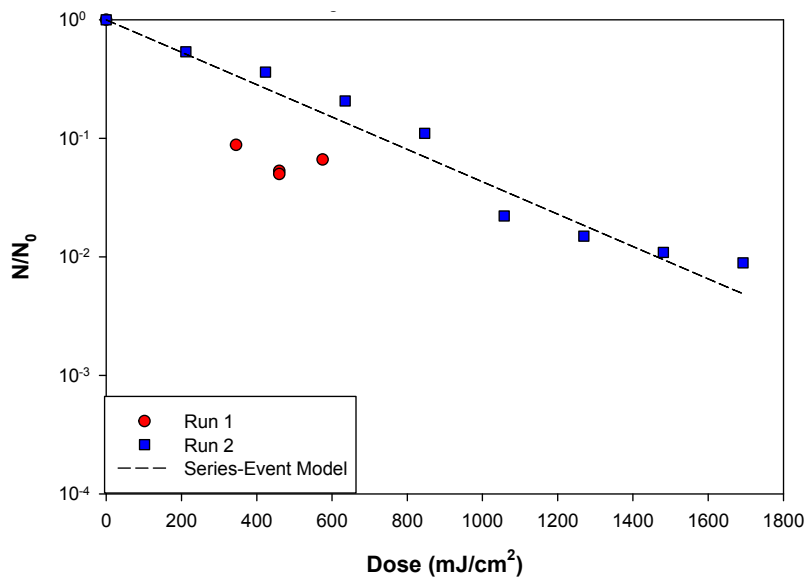
Figure 4.26. *V. harveyi* dose-response at 330 nm (n = 1; k = 0.003 cm^2/mJ).

The results of this series-event model fit of the data are summarized in Table 4.5, where an expected decrease in activation constant was observed as the wavelength increased from 254 nm to 310 nm. A slight increase in inactivation rate with increased wavelength is observed at 320 nm followed by a decrease in inactivation efficiency at 330 nm.

Table 4.5. Dose-response data for *V. harveyi* fit with the series-event model.

V. harveyi Dose-Response Studies fit with the Series-Event Model				
Wavelength (nm)	Inactivation Constant (k) (cm^2/mJ)	n	R^2	Normalized Inactivation Constant (k)
254	1.360	3	0.830	1.000
254				
254				
282	0.940	3	0.954	0.691
282				
282				
289	0.226	1	0.772	0.166
289				
289				
297	0.099	3	0.910	0.073
297				
297				
310	0.010	1	0.788	0.007
310				
310				
320	0.060	3	0.931	0.044
320				
330	0.003	1	0.852	0.002
330				

Figure 4.27 provides a summary of *V. harveyi* dose-response behavior at each of the wavelengths used in this work. These results illustrate a slight increase in effectiveness at 320 nm, relative to 310 nm and 330 nm.
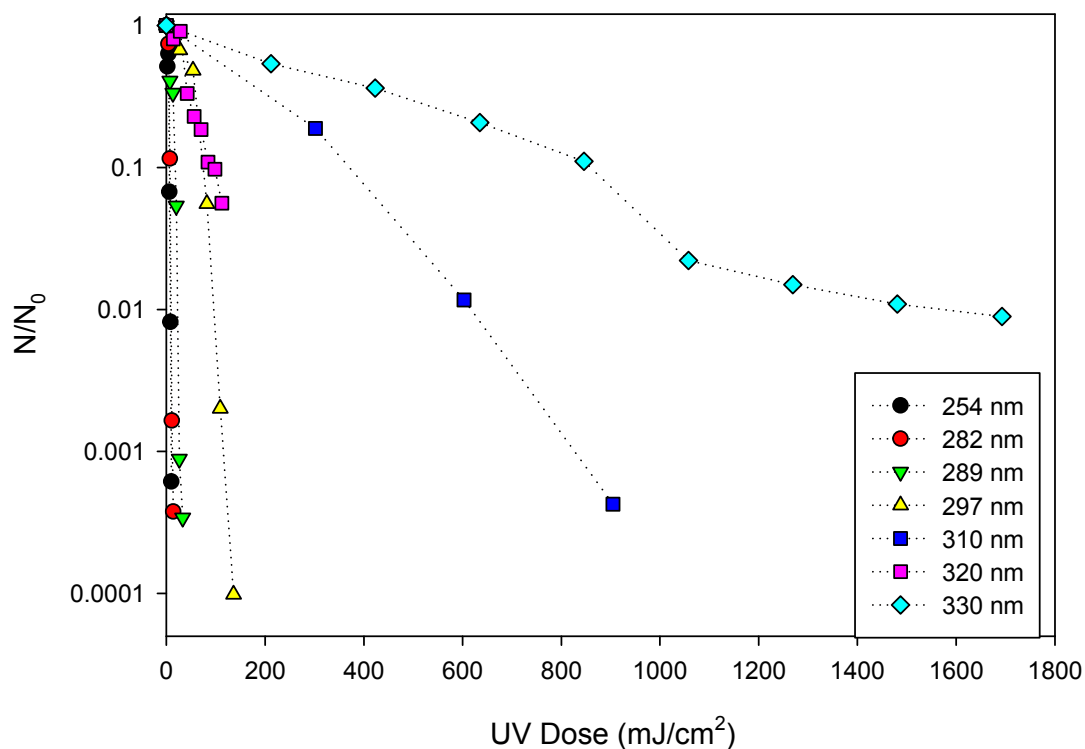
Figure 4.27. Overall comparison of dose-response data for *V. harveyi*.

Figure 4.28 provides a graphical illustration of relative inactivation constants and DNA absorbance across the range of wavelengths used in this study. The trend in relative inactivation constants followed the DNA absorbance spectrum up to approximately λ= 300 nm. For wavelength above this value, inactivation appeared to be enhanced relative to the trend in DNA absorbance. This may imply an increase in DNA absorbance in the vicinity of 320 nm, the involvement of other biomolecules in inactivation at UVB

wavelengths, systematic error of the 320 nm experiments, or UVA effects as mentioned

for *S. typhimurium* LT2.
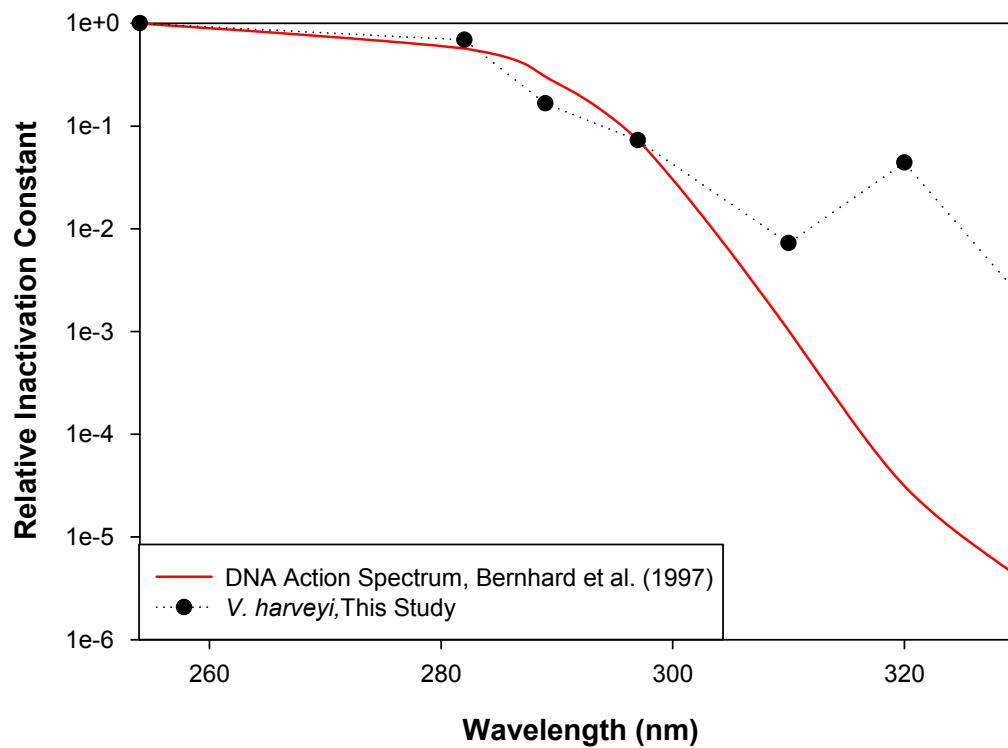
Figure 4.28. Summary of inactivation constants for *V. harveyi* compared to the
normalized response for DNA (Bernhard et al., 1997).

Cryptosporidium parvum

Quantification of inactivation was determined through enumeration of infectious foci within a host cell monolayer. These foci can consist of three to possibly hundreds of stained life stages of *C. parvum* within a diameter less than or equal to 175 μm (Johnson et al., 2012). Figure 4.29 shows foci from experimentation at 254 nm.
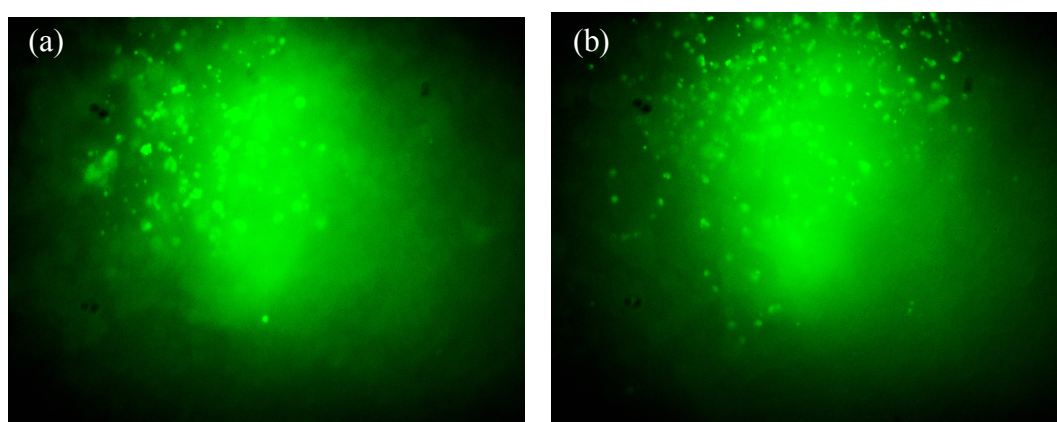
Figure 4.29. Foci observed at 254 nm (a) dose = 1 mJ/cm^2 at a dilution of 10^{-4} (b) dose = 2.0 mJ/cm^2 at a dilution of 10^{-3}.

For the mapping approach employed to quantify the *C. parvum* action spectrum, Equation 2.5 was used to fit the data from triplicate experiments a 254 nm to one curve. This was the reference wavelength (λ_{ref}) that was used to map the dose-response behavior at other wavelengths. The regression line determined for combined data sets in Figure 4.30 can be described by Equation 4.5. The R^2 value for this fit was 0.8526.

$$\log_{10} \frac{N}{N_0} = 0.1536 \cdot D^2 + 0.2998 \cdot D$$
<div align="right">Equation 4.5</div>
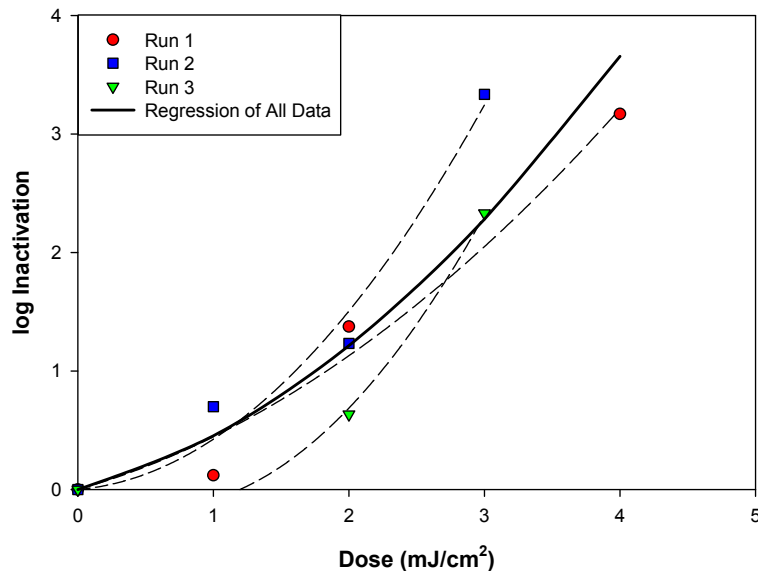
Figure 4.30. Dose-response behavior of *C. parvum* at 254 nm; individual fits are represented with the dotted lines (k = 1.0); solid line represents the regression for the total data set that was used as the basis for mapping.

To map every other wavelength onto this quadratic regression line at 254 nm, the doses at each wavelength were multiplied by a weighting factor (*w)*, which represents the normalized inactivation constant. The associated MATLAB codes for fitting can be found in Appendix B. The results of this mapping approach are summarized in Table 4.6.

Figure 4.31 illustrates the dose-response behavior at 280 nm. At a dose of 2.0 mJ/cm^2 this wavelength achieved 1-2 log$_{10}$ units inactivation, resulting in a normalized inactivation constant of 1.084 with a standard deviation of 0.21. The R^2 values correlated with each individual run were in the range of 0.69 - 0.94. Data at λ = 280 nm had the lowest correlation of the regression (R^2).
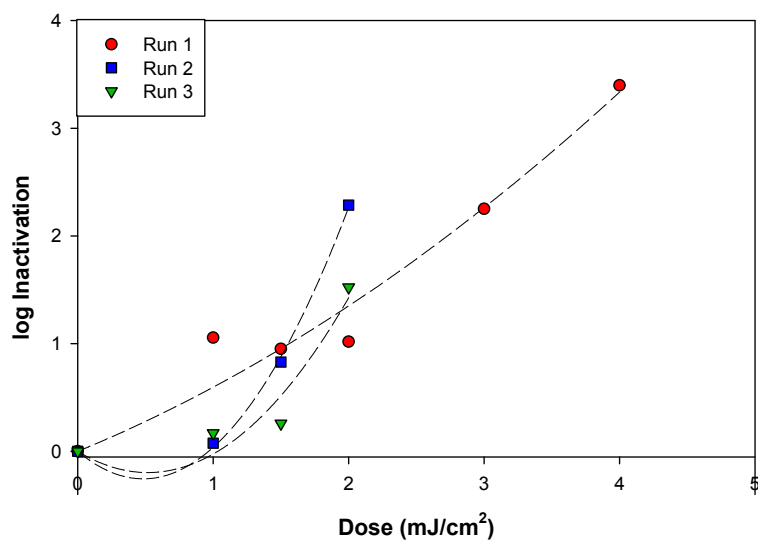
Figure 4.31. Dose-response behavior of *C. parvum* at 280 nm with quadratic regression lines for data set (k = 1.084, σ = 0.209).

Figure 4.32 illustrates measured dose-response behavior for *C. parvum* inactivation at 289 nm. At a dose of 10 mJ/cm^2 this wavelength can achieve approximately 3-log$_{10}$ units inactivation, resulting in a normalized inactivation constant of 0.419 with a standard deviation of 0.121. The R^2 values correlated with each individual run were 0.96 and above.

The dose-response data at 297 nm are illustrated in Figure 4.33, where the normalized inactivation constant was 0.131 with a standard deviation of 0.031. The resulting R^2 values were above 0.93 in each experimental run. It was also apparent that there was a decrease in inactivation rate at 297 nm relative to 289 nm. This was consistent with the DNA absorbance spectrum.
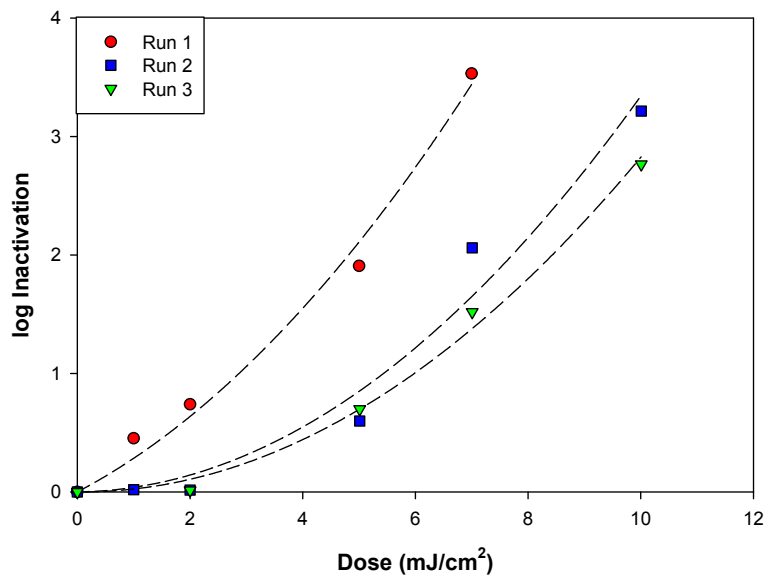
Figure 4.32. Dose-response behavior of *Cryptosporidium parvum* at 289 nm with quadratic regression lines for data set (k = 0.419, σ = 0.121).
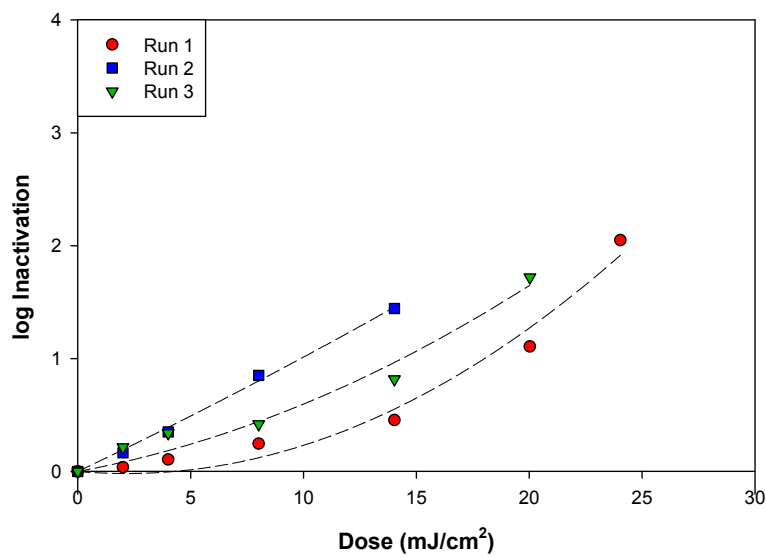
Figure 4.33. Dose-response behavior of *C. parvum* at 297 nm with quadratic regression lines for data set (k = 0.131, σ = 0.031).

UV dose-response behavior for *C. parvum* at 310 nm is illustrated in Figure 4.34. A dose of 150 mJ/cm^2 yielded 3.17-log$_{10}$ units inactivation. The average normalized inactivation constant was 0.028 with a standard deviation equal to 0.005. The R^2 values for mapping to 254 nm ranged from 0.87 to 0.96.
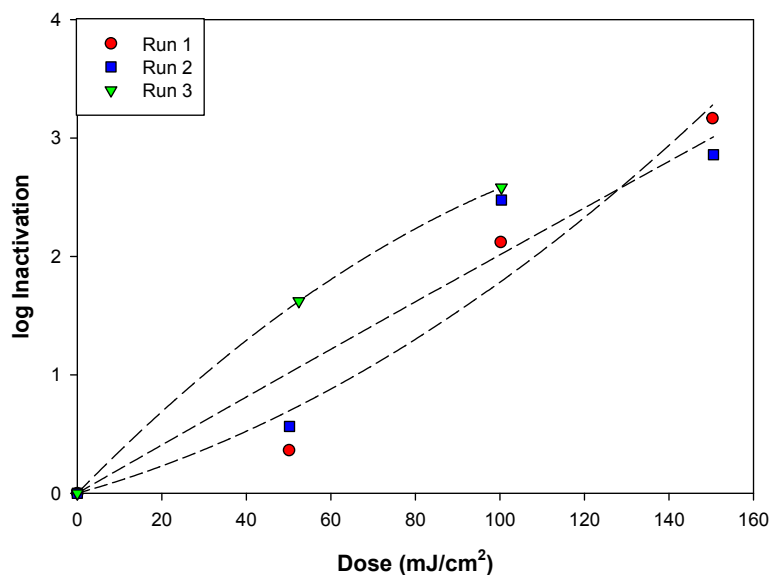
Figure 4.34. Dose-response of *C. parvum* at 310 nm with quadratic regression lines for data set (k = 0.028, σ = 0.005).

Figure 4.35 represents the dose-response behavior at 320 nm; the dose required for 3-log$_{10}$ units of inactivation was about half of that that was required at 310 nm. At a dose of 60 mJ/cm^2, this wavelength can achieve between 3-4 log$_{10}$ units inactivation resulting in a normalized inactivation constant of 0.075 with a standard deviation of 0.013. The R^2 values correlated with each individual run were 0.94 and above.
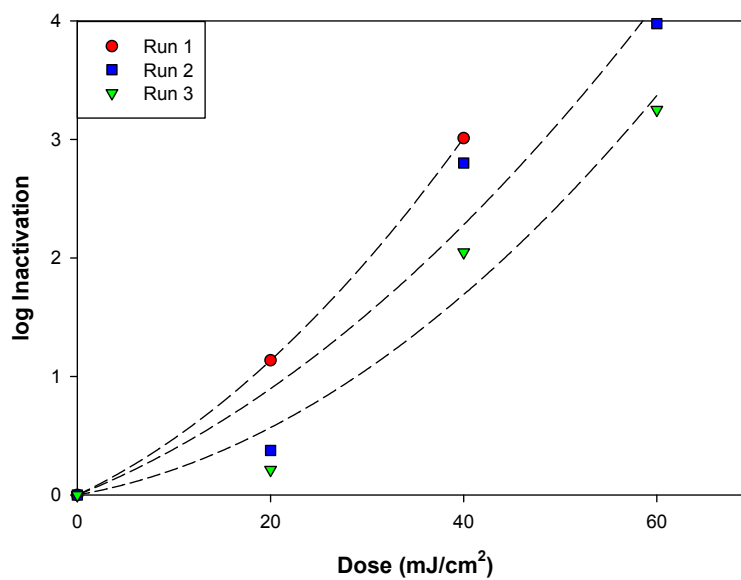
Figure 4.35. Dose-response behavior of *C. parvum* at 320 nm with quadratic regression lines for data set (k = 0.075, σ = 0.0.013).

At 330 nm (Figure 4.36), a decrease in inactivation efficiency was observed relative to 320 nm; similar behavior was observed for *S. typhimurium* LT2 and *V. harveyi*. The average normalized inactivation constant was 0.055 with a standard deviation of 0.008. R^2 values were above 0.91.
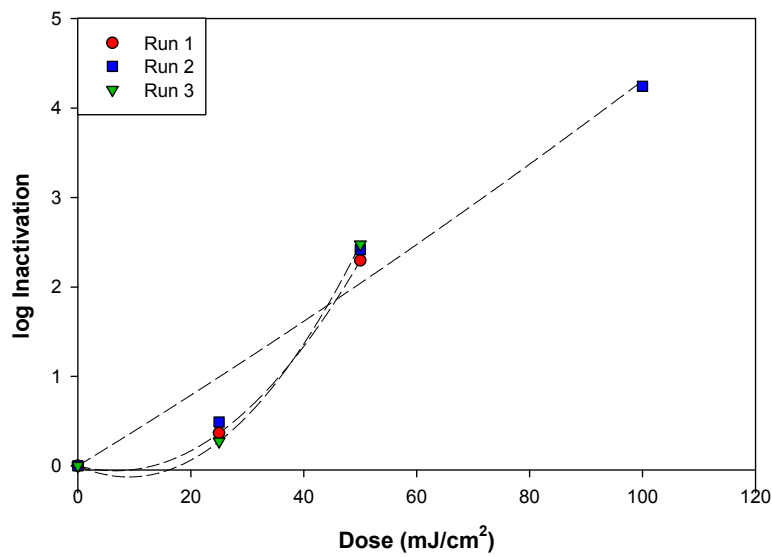
Figure 4.36. Dose-response behavior of *C. parvum* at 330 nm with quadratic regression lines for data set (k = 0.055, σ = 0.008).

Table 4.6. Dose-response data for *C. parvum* fit with the mapping approach.

C. parvum Dose-Response Studies fit with the Mapping Approach					
Wavelength (nm)	Normalized Inactivation Constant (k)	R^2	Average Normalized k	Standard Deviation	Normalized k (Beck et al., 2015)
254					
254	1.000	N/A	1.000	N/A	1.015
254					
280	0.973	0.936			
280	1.325	0.804	1.084	0.209	0.876
280	0.954	0.690			
289	0.557	0.986			
289	0.368	0.957	0.419	0.121	0.528
289	0.331	0.972			
297	0.105	0.925			
297	0.166	0.964	0.131	0.031	0.200
297	0.122	0.964			
310	0.025	0.964			
310	0.025	0.869	0.028	0.005	
310	0.034	0.879			
320	0.090	0.997			
320	0.073	0.945	0.075	0.013	
320	0.063	0.962			
330	0.058	0.944			
330	0.045	0.913	0.055	0.008	
330	0.061	0.916			

Figure 4.37 provides a comparison of representative inactivation curves at each

wavelength. The trend in inactivation responses was similar to those observed with the

two bacterial species. Specifically, for wavelengths ranging from 254 nm to 310 nm, the

inactivation response became less efficient as wavelength increased. The inactivation

behavior at 320 nm was more efficient than at 310 nm, followed by a decrease at 330 nm.
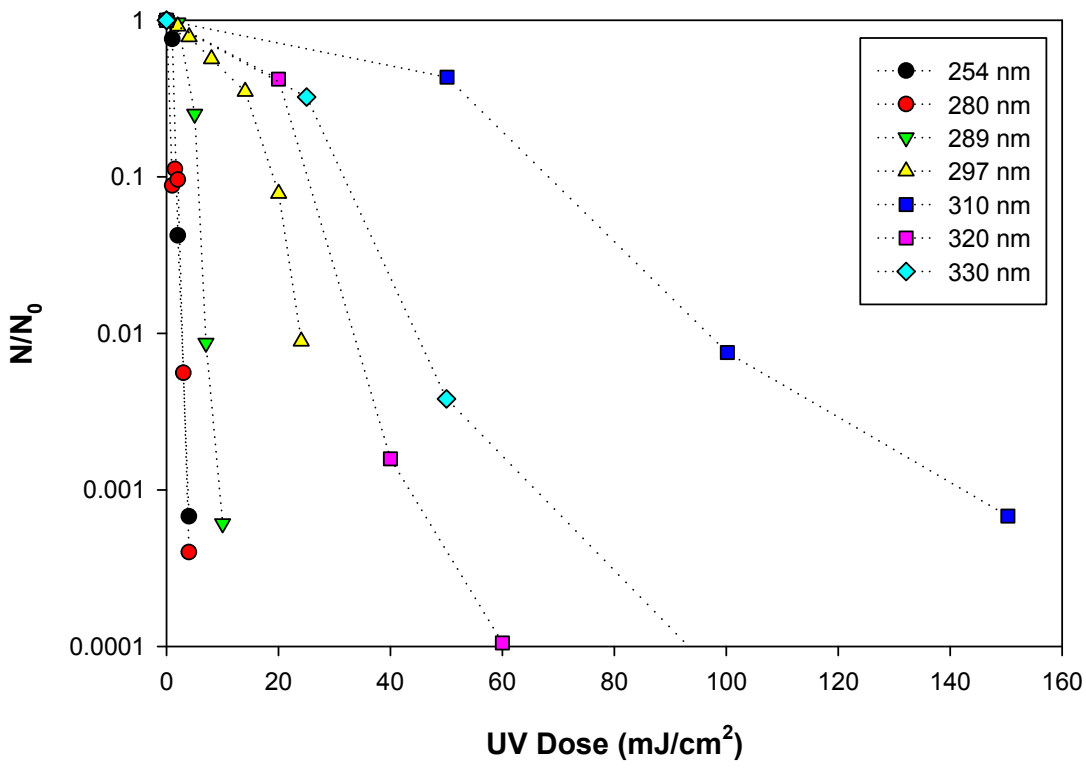
Figure 4.37. Overall comparison of dose-response data for *C. parvum* on the same
inactivation and dose scales.

Figure 4.38 provides a graphical comparison of the results of this work with previously

reported action spectra for *C. parvum* as well as a DNA absorbance reference spectrum.

The data from this study, normalized with the mapping approach is in general agreement

with the data from the work of Linden et al., 2001 and Beck et al. (2015) for wavelengths

up to 290 nm, but allows extension into the UVB range.
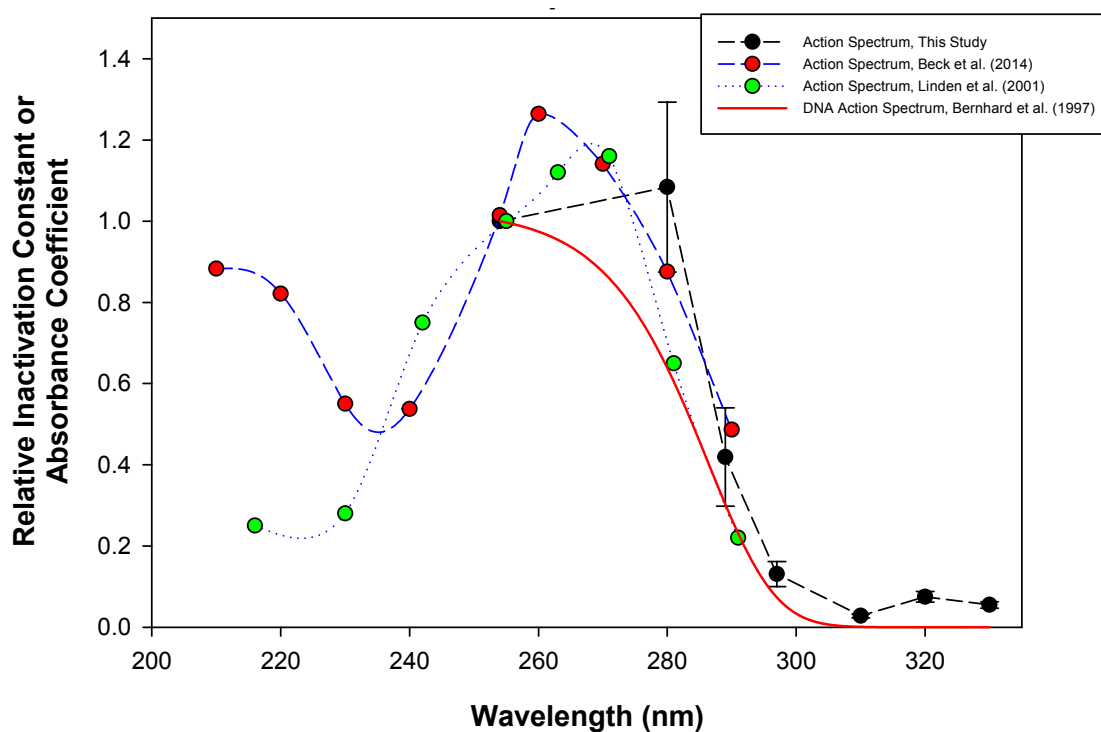
Figure 4.38. Summary of inactivation constants for *C. parvum* compared to the
normalized response for DNA.

4.4   Discussion/Conclusion

Salmonella typhimurium LT2

Dose-response curves from this study reveal that both the single-event model and multi-

target model fit the data well. In the study conducted by Chen et al. (2009), inactivation

of *S. typhimurium* LT2 required a UV_{254} dose of 4 mJ/cm^2 for approximately 0.8-log$_{10}$

units inactivation. The results herein reported higher inactivation for all UV_{254} doses,

yielding an average inactivation of 1.63-log$_{10}$ units across the triplicate experiments at a

UV_{254} dose of 4 mJ/cm^2. This is almost double the inactivation observed by Chen et al.

(2009). Chen et al. (2009) also reported tailing effects after 4-log$_{10}$ inactivation at 225

nm, 292 nm and 303 nm; no tailing behavior was observed in this study.

The differences in sensitivity of *S. typhimurium* LT2 between the work of Chen et al.

(2009) and those reported herein may be due in part to the strains of *S. typhimurium* LT2

used. Chen et al. (2009) used *S. typhimurium* LT2 (SL3770 from the *Salmonella* Genetic

Stock Centre at University of Calgary), which has weakened pathogenicity in comparison

to *Salmonella* spp.. In this study *S. typhimurium* LT2 (TL155) was used, which is a

restriction-modification (R-M) strain (O'Connor et al., 2009). R-M systems are

commonly made up of a restriction endonuclease and a modification enzyme which

identifies the same nucleotide sequence as the endonuclease. This can lead to methylation

of bases within the system altering DNA to become available for attack (O'Neill et al.,

1997), which could potentially affect inactivation properties of the system.

Wavelength-dependent results based on a MP lamp with optical filters may also differ

due to differences in the methods used to quantify irradiance delivered to the microbial

suspension. In this study, the wavelength corresponding to peak transmittance of the filter

was defined as the wavelength of exposure. Chen et al. (2009) used a weighted average

wavelength for each filter, based on measurements of the relative photon flux at each

wavelength. The weighted average wavelength adjusted the filter classification of the wavelength by at most 3 nm for wavelengths above 280 nm (Chen et al., 2009).

Results reported herein, as well as others in the literature indicate that the action spectrum for *S. typhimurium* LT2 generally follows the DNA absorbance spectrum, but with slightly higher relative inactivation at wavelengths above 330 nm. Similarity between the action spectrum and the DNA absorbance suggests that the DNA absorbance spectrum could be used to develop a conservative estimate of the action spectrum.

Vibrio harveyi

V. harveyi was selected as a surrogate for pathogenic *V. cholerae* in this work. *V. cholerae* has been widely studied for UV inactivation, and it is known to be more sensitive than *S. typhi* and *E. coli* to UVC radiation (Coohill and Sagripanti, 2008). For example, 1-$\log_{10}$ unit of inactivation of *V. cholerae* has been reported to require a UV_{254} dose of 1.1 mJ/cm^2; a UV_{254} dose of 2.5-5 mJ/cm^2 is required for 4-$\log_{10}$ units of inactivation (Coohill and Sagripanti, 2008). Other studies have indicated that 1-$\log_{10}$ unit of inactivation can be achieved with a UV_{254} dose of 2 mJ/cm^2, with 4-$\log_{10}$ units inactivation being achieved with UV_{254} dose of 9 mJ/cm^2 (Hijnen et al., 2006). For the work reported herein, a UV_{254} dose of 6 mJ/cm^2 yielded average inactivation of 1.67-$\log_{10}$ units for *V. harveyi*. To achieve 3-$\log_{10}$ units inactivation, a UV_{254} dose of 8 mJ/cm^2 was required. In general, *V. harveyi* is less sensitive to UV exposure than *V. cholerae*, and as such may represent a conservative surrogate for the bacteria that cause cholera.

Figure 4.39 is an image of plates after exposure to 289 nm radiation at a dose of 6 mJ/cm^2 (left) and 10 mJ/cm^2 (right). Inconsistency in colony size is evident in this image. At a dose of 6 mJ/cm^2, there are larger colonies, with smaller colonies scattered throughout. On the plate that was exposed to a dose of 10 mJ/cm^2, all of the colonies consistent in size indicating that they formed at the same time.

This is consistent with the literature where bacteria with bioluminescence can actually generate their own light repair in dark conditions through the *lux* gene (Kozakiewicz et al., 2005). More specifically, *V. harveyi, luxA, luxB* and *luxD* mutants, which are all unable to produce light, can be responsive to UV radiation under dark conditions resulting in light emission for photorepair (Czyz et al., 2000).
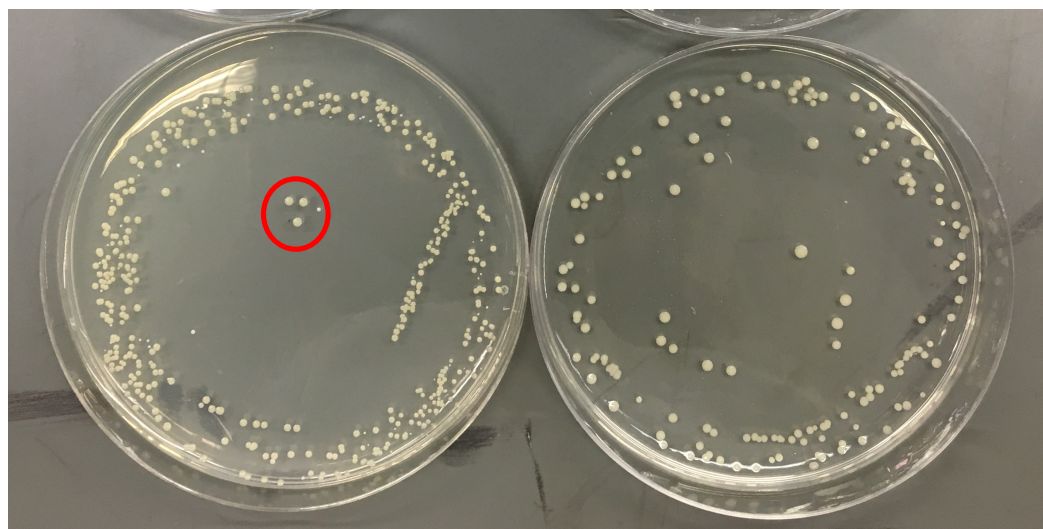
Figure 4.39. HIB agar plates with *V. harveyi* after exposure to radiation at 289 nm (Left: Dose = 6 mJ/cm^2; Right: D = 10 mJ/cm^2).

Though not the focus of this study, the details of photoreactivation will be important to understand in order to proceed with any bioluminescent surrogate for an organism in UV inactivation studies.

Cryptosporidium parvum

In this study, at a dose of 2.0 mJ/cm^2 using a LP UV source, an average 1.1-log$_{10}$ inactivation was observed across the triplicate experiments. In the literature, 1.7-log$_{10}$ inactivation has been reported to result from a LP UV dose of 2.0 mJ/cm^2 (Linden et al., 2001). With a tunable laser, 2.0-log$_{10}$ units of inactivation was reported to result from a UV$_{254}$ dose of 1.9 mJ/cm^2 (Beck et al., 2015). Another study reported on an optically-filtered MP UV source that was used to expose samples to wavelengths from 216 nm to 290 nm with the same brand of optical filters used in this study (Linden et al., 2001). At each wavelength, the samples were exposed to 2.0 mJ/cm^2 of irradiation. These results indicated that at a wavelength of 255 nm there was 1.8-log$_{10}$ units of inactivation, at 281 nm 1.3-log$_{10}$ units of inactivation were observed, and at 290 nm 0.5-log$_{10}$ units of inactivation were observed (Linden et al., 2001). The three studies yielded similar results; by comparison, the experiments and the study described herein indicated lower inactivation at 254 nm. This could be, in part due to the application of the trypsinization process (that excited the *C. parvum* for infection), before the UV exposure. The study conducted by Beck et al. (2015) involved trypsinization after UV exposure. Trypsinization involves application of an acidic solution to alter the oocyst walls to allow for the entrance of trypsin. Subsequent exposure of trypsinized oocysts to bile salts results in release of the sporozoites in preparation for infection (Hijjawi, 2003). Because

exposure to bile and elevated temperature (37^oC) were not performed unitl after UV

exposure, it is likely that UV exposure involved only the oocysts (i.e., no other life stages

were exposed to UV radiation). Therefore, it is difficult to determine whether this

excitation process had a significant effect on experimental results.

Overall

Experimentation at 320 nm and 330 nm should be studied further to understand the cause

of increased inactivation at these two wavelengths in comparison to 310 nm. Based on

observation and results from the radiometer, it is evident that there was greater irradiance

the difference between irradiance at the center of the beam relative to the beam edge was

greater when type 3 optical filters were used (320 nm and 330 nm) than when type 7

optical filters were used (all other wavelengths). Although microbial suspensions were

continuously stirred, calculation of average irradiance across the petri dish may not

accurately describe the amount of irradiation received by the sample. The change in

irradiance from beam center to beam edge should be quantified and compared to the

calculated average irradiance. This feature of the optically-filtered collimated beam could

be improved by adding a non-focusing lens to the beam to more evenly distribute the

radiation.

CHAPTER 5. UV MODELING

5.1   Introduction

Quantification of ambient UVB spectral irradiance is crucial to determining which

wavelengths will contribute most effectively to microbial inactivation with a UV

disinfection system. A UVB Monitoring Network has been established by the USDA and

Colorado State University. Data from this network of stations is collected to define actual,

ambient spectral irradiance across the UVB spectrum and at longer wavelengths. As such,

the data from this network represent a standard for comparison against numerical

simulations of spectral irradiance. By comparing measurements with model predictions, it

is possible to define error associated with model predictions. By extension, this allows for

an assessment of error in application of numerical simulation for prediction of spectral

irradiance at locations outside the USDA UVB Monitoring Network.

5.2   Materials & Methods

Due to the difficulty in quantification of cloud cover, most UV modeling tools struggle to

provide accurate simulations of UV spectral irradiance for cloudy conditions. Therefore,

data used for comparison with model results were collected from the USDA UV

Modeling Network for clear days, using historical data from Weather Underground

(https://www.wunderground.com/us/in/lafayette/zmw:47907.13.99999) at the Purdue

University Airport (KLAF), which is 6.5 miles from the UVB monitoring network site at

the Purdue Agronomy Farm . Historical cloud cover is reported on an hourly basis, and

the days that were defined as clear were considered for evaluation. Other classifications

of cloud cover included: mostly cloudy, scattered clouds and overcast.

USDA UV Modeling Network

Network data by site and date can be obtained at the USDA UVB Modeling Network

website (http://uvb.nrel.colostate.edu/UVB/da_queryLangleyIrradiance.jsf). Data

downloaded from the site included time of day, total irradiation, direct irradiation and

diffuse irradiation. Irradiance measurements were downloaded at six wavelengths – 300

nm, 305 nm, 311 nm, 317 nm, 325 nm and 368 nm.

TUV Model

The TUV model has been used to simulate UV spectral irradiance. The program was

downloaded from the NCAR website

(https://www2.acom.ucar.edu/modeling/tropospheric-ultraviolet-and-visible-tuv-

radiation-model). Figure 5.1 is the user interface for version 5.2 of the TUV model. Input

parameters defined location, time of day/year and atmospheric composition.

```
TUV inputs:
============================================================================
inpfil =         WL    outfil =      I70414   nstr =             -2
lat =        40.050    lon =        -88.370   tmzone =         -5.0
iyear =        2014    imonth =           7   iday =              4
zstart =      0.188    zstop =       80.000   nz =               81
wstart =    300.000    wstop =      370.000   nwint =          -156
tstart =      0.000    tstop =       24.000   nt =               25
lzenit =          F    alsurf =       0.100   psurf =        -999.0
o3col =     297.000    so2col =       0.000   no2col =        0.000
taucld =      0.000    zbase =        4.000   ztop =          5.000
tauaer =      0.262    ssaaer =       0.990   alpha =         1.000
dirsun =      1.000    difdn =        1.000   difup =         0.000
zout =        0.216    zaird =    -9.990E+02   ztemp =      -999.000
lirrad =          T    laflux =           F   lmmech =            F
lrates =          T    isfix =            0   nms =               7
ljvals =          F    ijfix =            0   nmj =               0
iwfix =           0    itfix =            0   izfix =             0
============================================================================
Type ?variable for help on a variable, or
<enter> = keep these settings, or
Type variable name to change (lower case):
```

Figure 5.1. TUV user interface (version 5.2).

The program is initiated with an input file (inpfil) that can be modified, saved and re-

called. A default program, defin1, was chosen as a starting point because it is the

suggested model for calculations of spectral irradiance at the earth's surface at

wavelengths between 280 nm – 420 nm at an interval of 1 nm. A 2-stream delta-

Eddington code is used to output the sum of radiation in all directions. Output files (outfil)

are saved as text files under a six-character name that can be defined by the user. Altering

the values for iyear, imonth and iday in numerical form changes the date to that which the

user wants to model (Madronich, 2014).

Site-specific details are the next parameters to consider. Time zone (tmzone) is a

numerical value of the time difference from Coordinated Universal Time (UTC)

(Madronich, 2014). As an example, West Lafayette is five hours behind UTC, resulting

in tmzone = -5. The latitude (lat) and longitude (lon) of the desired site are defined, and

the directions are indicated by positive or negative values – North (+); South (-); East (+);

West (-). Elevation of the test site (zstart) is defined as well as the elevation of the output (zout) in kilometers above mean sea level. Elevation at the top of the atmosphere is also defined (zstop). The sun's zenith angle (lzenit) was set to false (F), which prompts the program to use calculated values for this parameter (Madronich, 2014).

Atmospheric conditions are also site-specific and there are a number of parameters that can be defined in this program. According to a study that observed and modeled solar UV in Antarctica, the two parameters with the greatest impact on the output are the ozone column (o3col) and the atmospheric aerosols (tauaer) (Ghude et al., 2008). Other factors such as the SO_2 and NO_2 columns are not considered by some studies due to their low levels that have little to no effect on the output (Palancar and Toselli, 2004). Atmospheric ozone (AOD) is a parameter with collected data from NASA satellites based on absorbance measurements at a wavelength of 550 nm.

5.3   Results

In partnership with Colorado State University, the USDA has set up a UVB Monitoring Network site in West Lafayette, IN at the Purdue Agronomy Farm. Data from this site were used for comparison to modeled data from TUV. One such comparison was conducted on August 1, 2013. This day was selected because a field experiment involving a prototype CPC was conducted in West Lafayette, IN on that date. According to Weather Underground, this day was classified as clear from 9:54 AM until 12:45 PM. Between 1:54 PM and 6:54 PM there were scattered clouds and times defined as partly cloudy. After this point the day was again considered clear.

Differences in measured and simulated spectral irradiance were calculated for three

wavelengths (305 nm, 311 nm, 325 nm) (Table 5.1), where both TUV predictions and

USDA measured spectral irradiance was available on August 1, 2013 in West Lafayette,

IN. Error was calculated as the percent deviation of the TUV predicted value from the

measured value.

In general, the model over-estimated measured UV irradiance. This is consistent with

results of other studies comparing UV models to ground-level studies, where regardless

of site location, models tended to overestimate the amount of UV on a clear day

(Buntoung and Webb, 2010).

Table 5.1. Summary of error between USDA UVB Monitoring Network measurements
and TUV estimates for West Lafayette, IN on August 1, 2013.

	ERROR (%)						
	Time (hh:mm)						
Wavelength (nm)	6:00	8:00	10:00	12:00	14:00	16:00	18:00
305		22.0	15.2	12.5	11.7	19.6	6.41
311	49.4	24.0	20.8	17.6	17.0	26.3	16.0
325	102	8.02	5.85	2.68	2.00	11.8	6.60
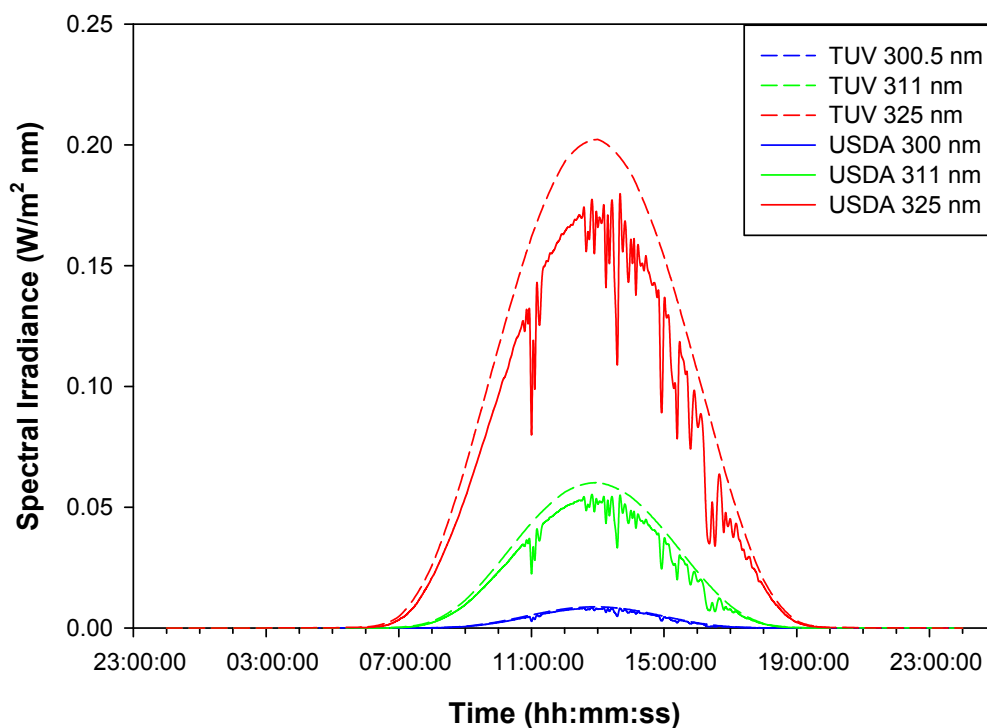
Figure 5.2. Comparison of simulated spectral irradiance from TUV and measured values from the USDA UVB Monitoring Network at wavelengths in the UVB range on August 1, 2013 in West Lafayette, IN.

Comparison of TUV model predictions with measured values from the USDA UVB

Monitoring Network were also conducted for a fixed, mid-summer date (July 15, 2015) at

several locations. These included Flagstaff, Arizona, Waimea, Hawaii and Ontario,

Canada. Similar results were observed at all locations in that the model results

consistently over-predicted measured values. A summary of the results at 305 nm is

presented in Figure 5.3. Variation in the USDA measurement data for Flagstaff, AZ and

West Lafayette, IN was largely due to cloud cover throughout the day. In these two cases,

the TUV model mimicked the overall trend of the USDA data. For Toronto, Ontario and

Waimea, Hawaii, model predictions were in better agreement, probably because of clear

sky conditions that prevailed for both locations that day.
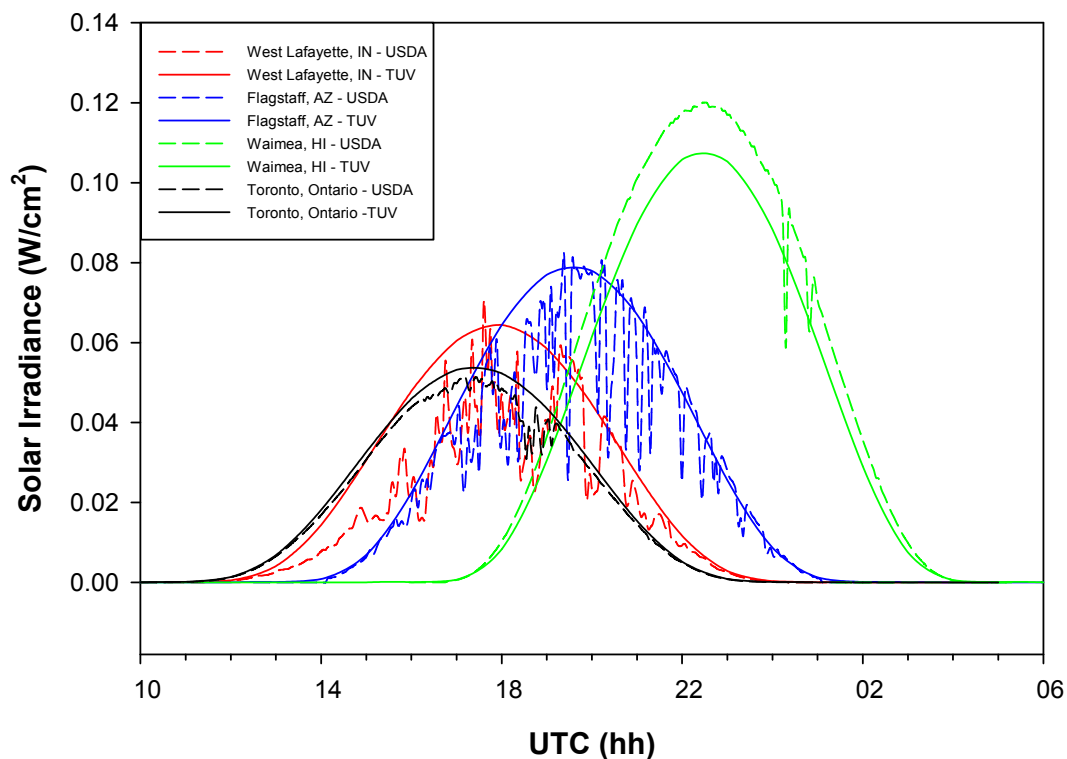
Figure 5.3 Comparison of spectral irradiance from TUV and the USDA UVB Monitoring
Network at 305 nm on June 15, 2015 for selected locations with USDA UVB monitoring
stations

With knowledge of the error associated with TUV, the model can be used to predict

available UV radiation at locations where there are no established monitoring stations.

This is the situation in most of the countries where solar UV disinfection could be

applied.

Critical parameters for application of the TUV model include: AOD, O_3, NO_2 and SO_2.

Data for these parameters and for spectral irradiance were examined as a function of date

throughout the year. Data were collected on the 15th of every month for the year 2015.

NASA's Giovanni version 4.18 was used to obtain data. Aerosol optical depth was

obtained with Giovanni through the MODIS-Terra satellite (MOD08_M3 v6) for deep

blue, land-only parameters. Data was recorded at latitude and longitude intervals (spatial

resolution) of 1° with a monthly temperature resolution. This satellite began recording

data in March of 2000. Figure 5.4 illustrates changes in AOD as a function of date over

the year 2015. Time-dependent trends have been observed based on location due to

combustion processes (Clarke and Kapustin, 2010), urbanization, altitude and wind

speeds (Ramachandran et al., 2012). Ramachandran et al. (2012) observed an increase of

AOD with urbanization and lower elevation. Types of aerosols detected by the satellite

are carbonaceous, mineral, dust, smoke and sulfate. Error associated with AOD

measurement includes the detection of clouds smaller than the satellite image pixel with

the instrument, but the effects have been reported to be minimal (Motohka et al., 2011;

NASA, 2012). All locations appeared to reach peak AOD by mid-June. Ramachandran et

al. (2012) also reported a similar observation for multiple locations across India.
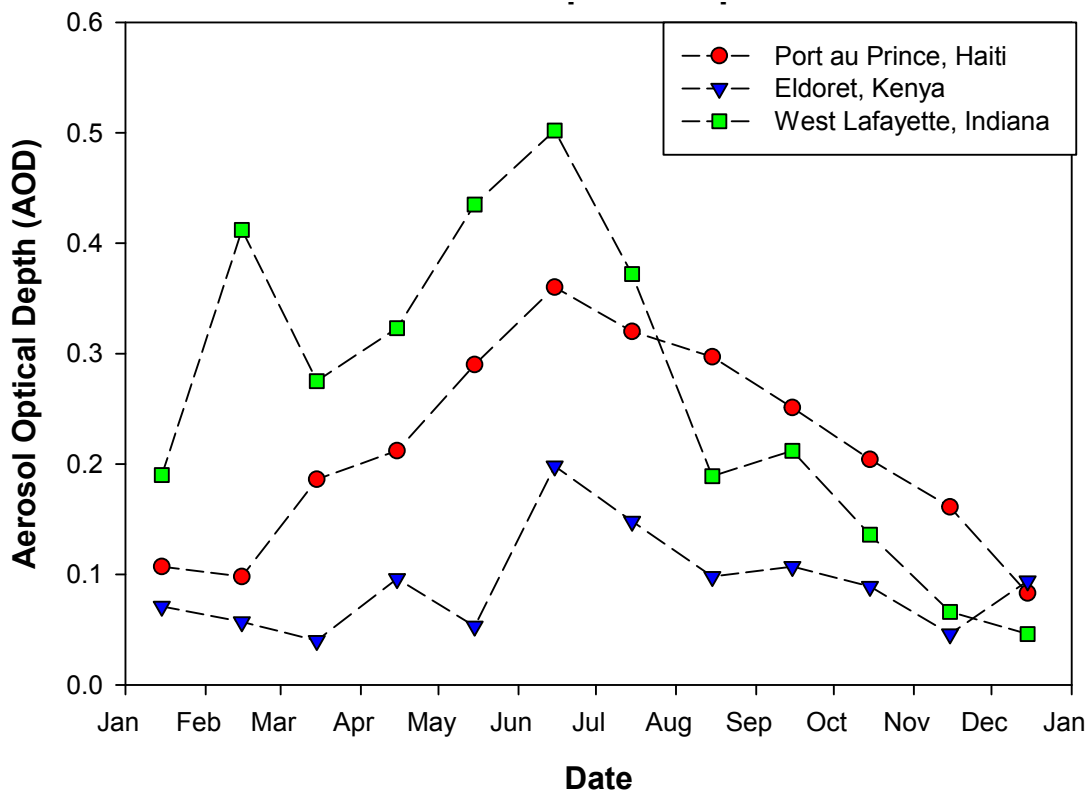
Figure 5.4. Comparison of aerosol optical depth (AOD) by location on the 15th of every month in 2015.

The next parameter examined as a function of time throughout the year was the ozone column in Dobson Units (DU). Ozone total column was obtained with the OMI, TOMS-like satellite (OMDOAO3e v003) with a daily temperature resolution and 0.25° steps in latitude and longitude (spatial resolution). The satellite was put into service in October of 2004. Results from the obtained ozone data are summarized in Figure 5.5. The time-dependence of the ozone column is associated with ozone transport due to weather pattern changes such as the North Atlantic Oscillation (NAO) over Europe, as well as pressure changes between low and high (Khokhlov and Romanova, 2011). In West Lafayette, IN, the highest values for ozone column were recorded in May, and in April

for Port au Prince, Haiti. The peak ozone column depth was recorded in September for

Eldoret, Kenya. With the lowest values ozone column recorded in Eldoret, Kenya, it is

evident that less solar radiation is blocked from reaching earth's surface by the

atmosphere at this location than the other two locations.
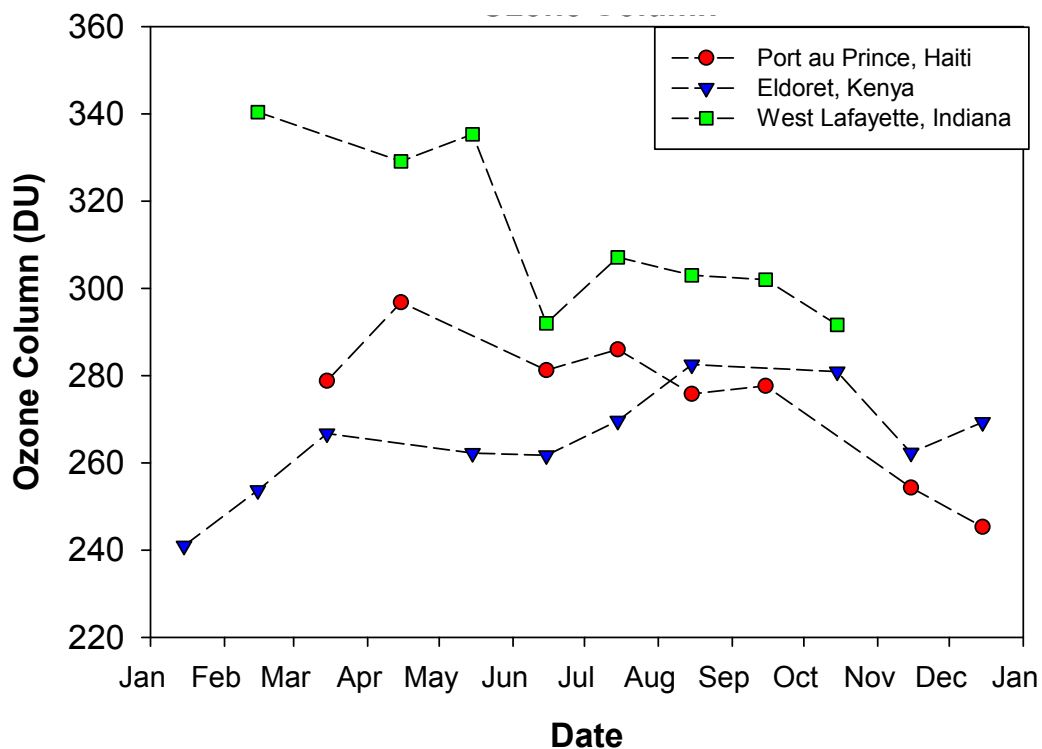
Figure 5.5. Comparison of the ozone column by location on the 15th of every month in 2015.

Sulfur dioxide (SO_2) data were obtained as SO_2 column amount with a planetary

boundary layer from the OMI satellite (OMSO2e v003). The data were collected at a

0.25^{o} spatial resolution and daily temperature resolution. The system was deployed in

October of 2004. Collected data are summarized in Figure 5.6 as a function of time of

year. Most of the data values obtained were negative (the sensor reported concentrations less than zero), resulting in a data set that was essentially unusable except for a few select positive points. Data from this satellite has been released for public use, but has not been fully validated (NASA, 2016). Therefore, only positive data points were used in the TUV modeling when they were available.
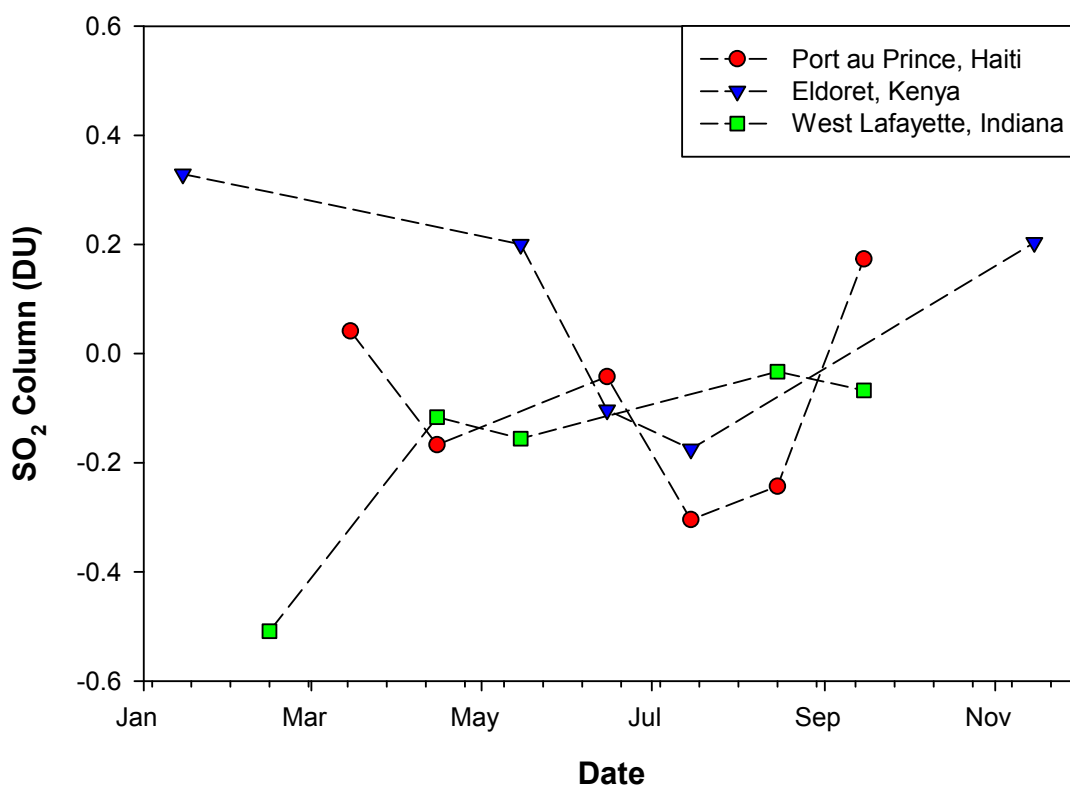
Figure 5.6. Comparison of SO_2 column by location on the 15th of every month in 2015.

Nitrogen dioxide (NO_2) was the last parameter obtained from the Giovanni data network. This data set was defined by the NO_2 Total Column that was 30% cloud screened (OMNO2d v003). Again, and the OMI satellite was employed using daily temperature resolution and 0.25^{o} spatial resolution. The units of this parameter were recorded in $1/cm^2$

and the results are summarized in Figure 5.7. For input into the TUV model, the column

was converted to Dobson Units using the relation that 2.69×10^{16} molecules/cm^2 equates

to 1 DU (Ahmad et al., 2007).
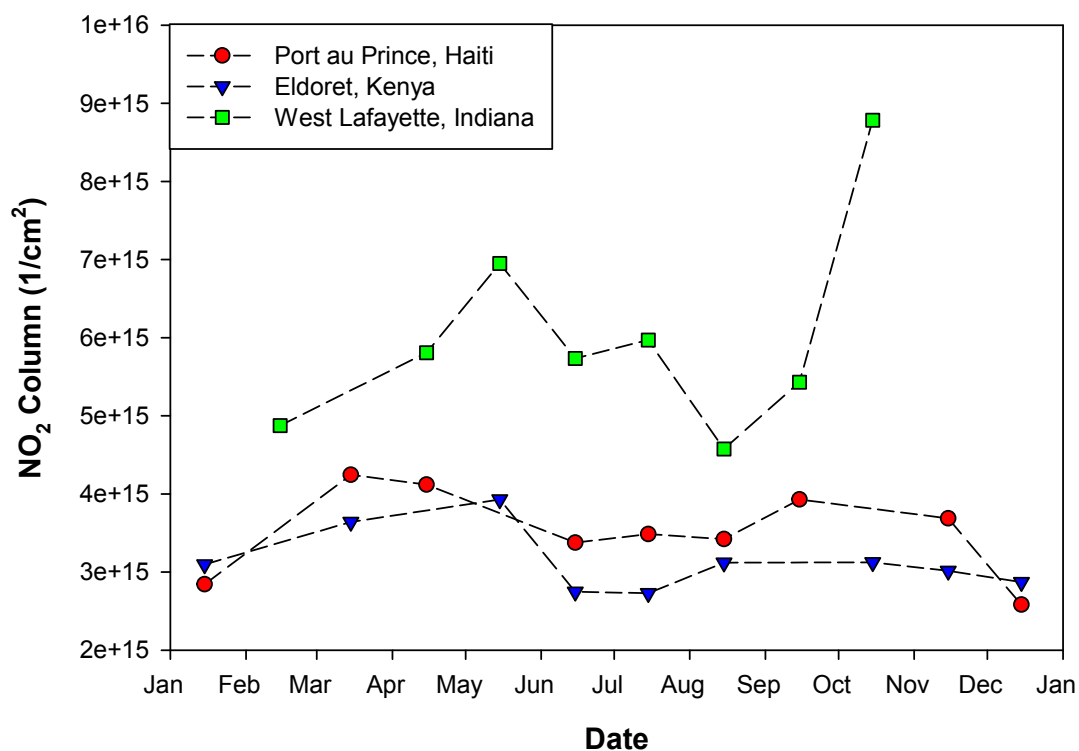
Figure 5.7. Comparison of NO$_2$ column by location on the 15th of every month in 2015.

The output from TUV was spectral irradiance on a predetermined hourly basis. Figure 5.8

depicts the results at 305 nm throughout the course of 2015. Latitude is largely

responsible for the seasonal variation in maximum spectral irradiance received. It can be

observed that the maximum daily peak irradiance received in West Lafayette, IN during

during June was lower than the lowest maximum daily peak irradiance ever observed in

Eldoret, Kenya. Peak irradiance in Eldoret, Kenya occurs in March and November.

Graphical summaries of data presented in Figures 5.4-5.8 can be found in Appendix C for other locations.
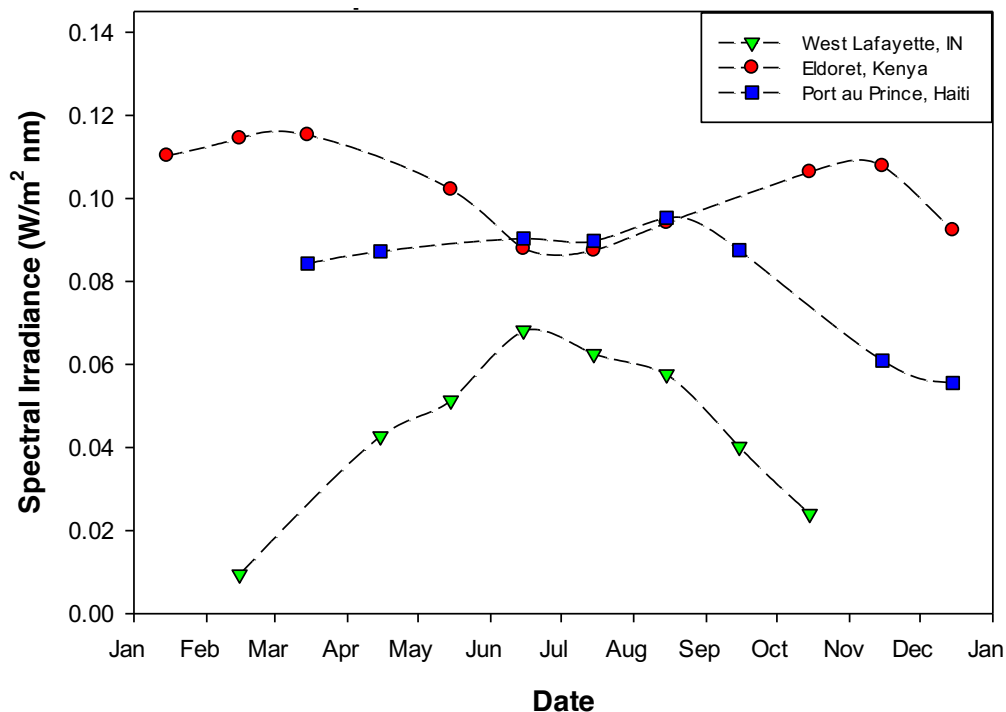
Figure 5.8. Comparison of maximum daily peak spectral irradiance at 305 nm by location on the 15th of every month in 2015.

June 15, 2015 was selected for further examination of the locational dependence of available UVB radiation. Three specific wavelengths were considered from the UVB spectrum - 300.5 nm (Figure 5.9), 305 nm (Figure 5.10) and 310 nm (Figure 5.11). The locations selected were the same as above in Figure 5.8: Port au Prince, Haiti; Eldoret, Kenya; and West Lafayette, Indiana. Each figure was plotted using identical horizontal and vertical axis scales to facilitate comparison. At 300.5 nm, solar irradiance barely exceeded 0.02 W/m^{2}nm at any location. Peak irradiance increased to 0.08 W/m^{2}nm at

305 nm and to just above 0.14 W/m^{2}nm at 310 nm. It can be observed that among these three locations, West Lafayette will receive the least amount of radiation. In June, West Lafayette, IN will receive its maximum amount of solar irradiance; spectral irradiance received in Eldoret, Kenya will be consistently higher than the peak irradiance observed in West Lafayette, IN. This indicates that if prototype studies were conducted in West Lafayette, IN during June, it would represent poorer performance of the reactor at any given point of the year for Eldoret, Kenya based on available UVB alone.
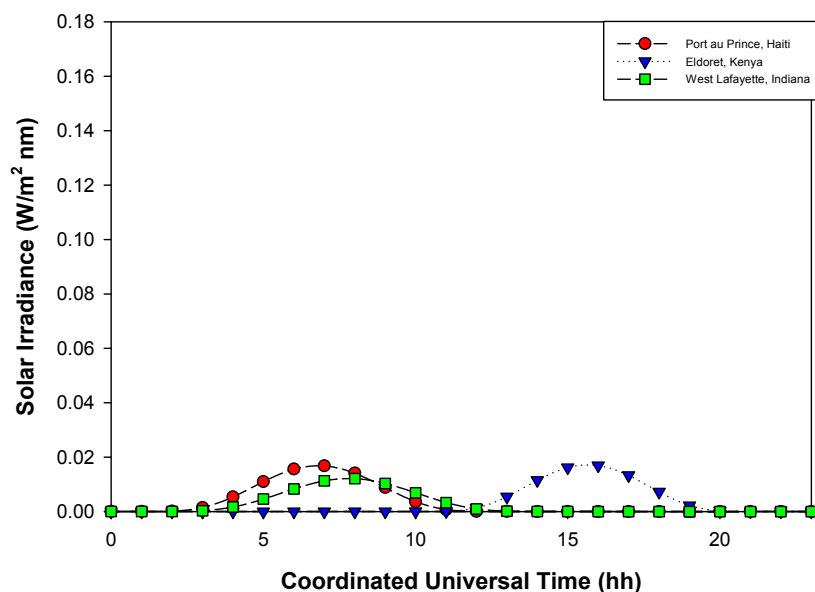
Figure 5.9. Comparison of spectral irradiance at 300.5 nm by location.
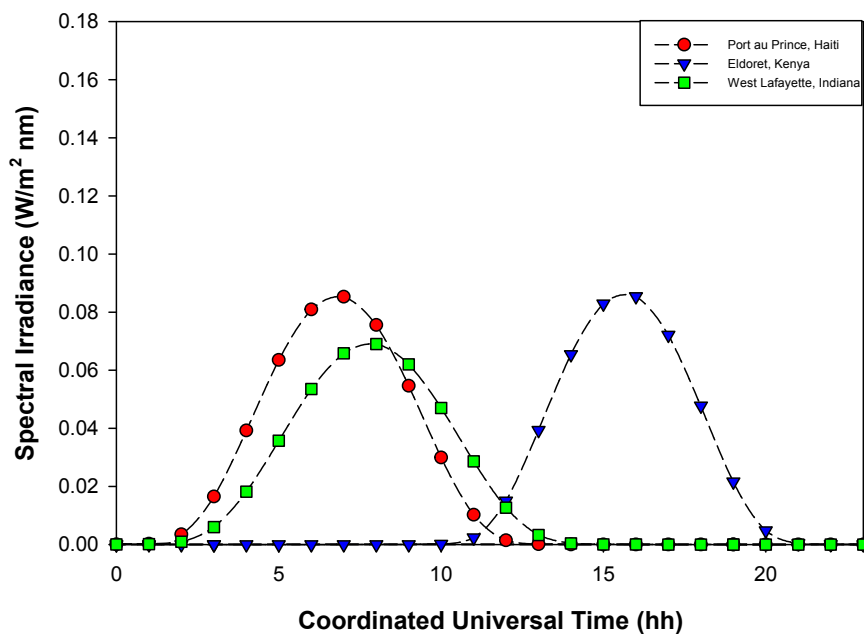
Figure 5.10. Comparison of spectral irradiance at 305 nm by location.
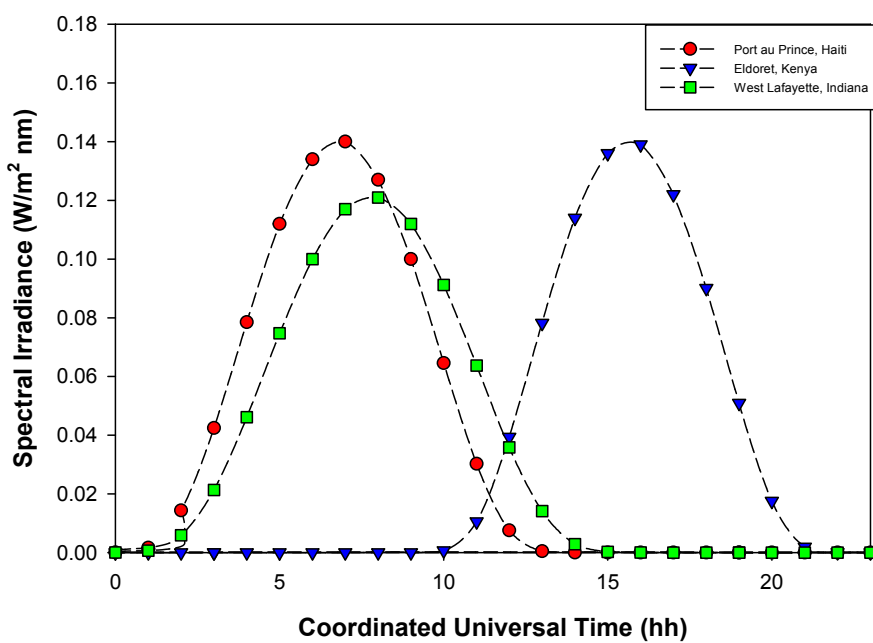
Figure 5.11. Comparison of spectral irradiance at 310 nm by location.

5.4   Discussion/Conclusion

Simulation results included herein indicate consistent over-prediction of the TUV model relative to measurements from the USDA UVB Monitoring Network for most locations. This was found to be true in other studies comparing the two methods as well. Xu et al. (2006) compared TUV data with measurements from the USDA UVB Monitoring Network in Holtville, California (CA22), Bondville, IL (IL02) and Nunn, Colorado (CO02). At these sites, total irradiance as well as direct and diffuse were modeled well with TUV at wavelengths less than 311 nm. Above 311 nm, the model appeared to over-predict the data, especially at lower solar zenith angles (CA22) (Wang et al., 2006; Xu et al., 2006).

For the simulations described herein, TUV was shown to consistently overestimate the data collected data from the USDA UVB monitoring network, except in Waimea, Hawaii. This was consistent in the literature, which identifies error in measurements leading to over-prediction at lower solar zenith angles, and Hawaii has a significantly larger solar zenith angle than the other sites considered. All things being considered, there is error associated with both the measured and modeled data sets, so the sensitivity of the system to the exact UV input will drive development of process controls.

CHAPTER 6. EFFECTIVENESS SPECTRA

6.1   Introduction

The combination of data from the action spectrum and the available UVB from modeling allows for the development of effectiveness spectra, which provides an understanding of the wavelengths that will be responsible for UV activation within the solar disinfection system.

6.2   Materials & Method

The effectiveness spectrum is defined by Equation 6.1. For each of the microorganisms in this study (*S. typhimurium* LT2, *V. harveyi* and *C. parvum),* effectiveness spectra were calculated.

$$Effectiveness(\lambda) = E(\lambda) \cdot A(\lambda)$$ Equation 6.1

Where,

λ = wavelength (nm)

$E(\lambda)$ = incident spectral irradiance (W/m^2·nm)

$A(\lambda)$ = normalized action spectra to 254 nm.

Incident spectral irradiance was simulated using the TUV model, and plotted as a function of wavelength for 10 AM, 12 PM, 2 PM and 4 PM in Figures 6.1, 6.2 and 6.3 on August 1, 2013 in West Lafayette, Indiana. The available spectral irradiance at 12 PM and 2 PM were similar, and the amount was significantly higher than that available at 10 AM or 4 PM.

6.3   Results
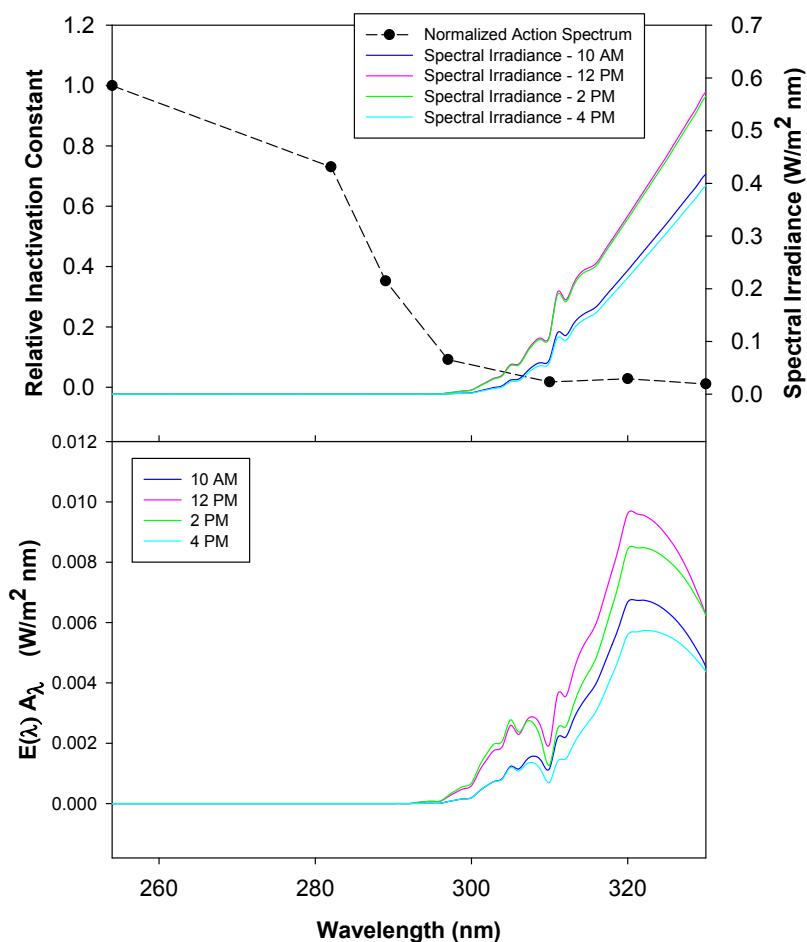
Figure 6.1. Effectiveness spectrum for *S. typhimurium* LT2 on August 1, 2013 in West Lafayette, Indiana.

The effectiveness spectra for *S. typhimurium* LT2 (Figure 6.1) indicate that the most

effective wavelengths for inactivation are in the vicinity of 320 nm. As wavelength is

increased, there is more UV radiation available. With the main mechanism of

inactivation predicted to be DNA damage, inactivation should decrease with a decrease in

DNA absorbance at increasing wavelengths. This was not the observed case for 320 nm,

resulting in a large effectiveness response with this wavelength.
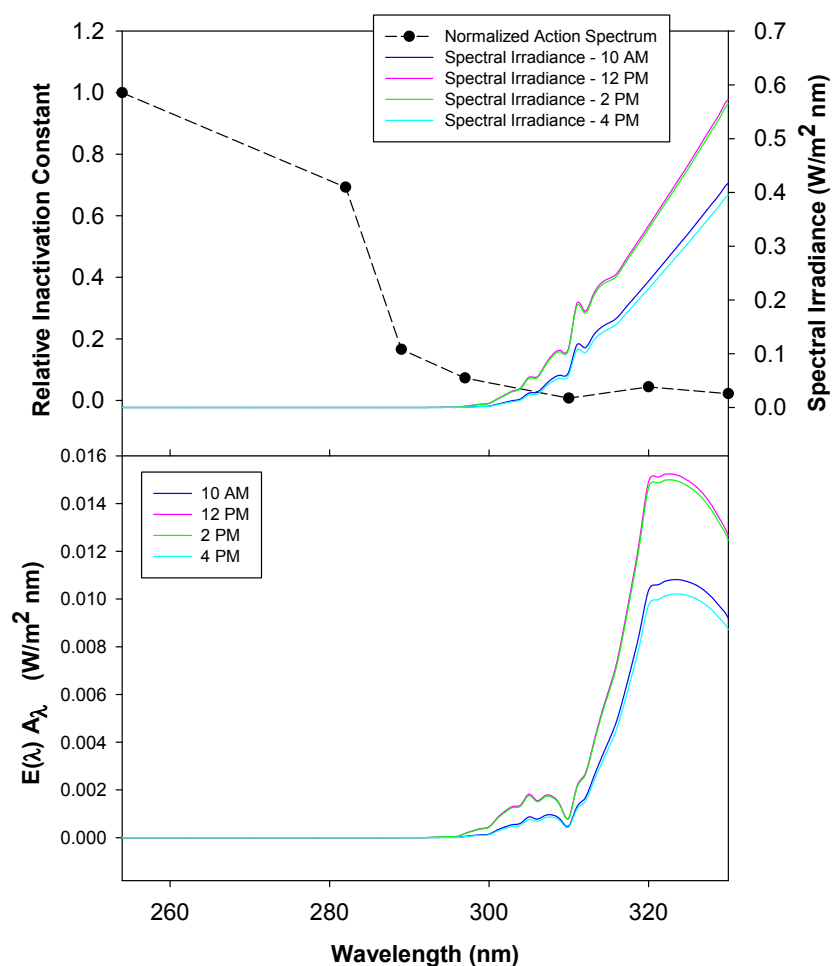
Figure 6.2. Effectiveness spectrum for *V. harveyi* on August 1, 2013 in West Lafayette, Indiana.

This same trend was observed for the effectiveness spectra developed for *V. harveyi* in Figure 6.2. Due to the large difference between available irradiance at 310 nm and 320 nm and the similarity in the normalized inactivation constant at both wavelengths (with 320 nm producing slightly more inactivation at a faster rate), 320 nm becomes the most effective wavelength for inactivation in the system.
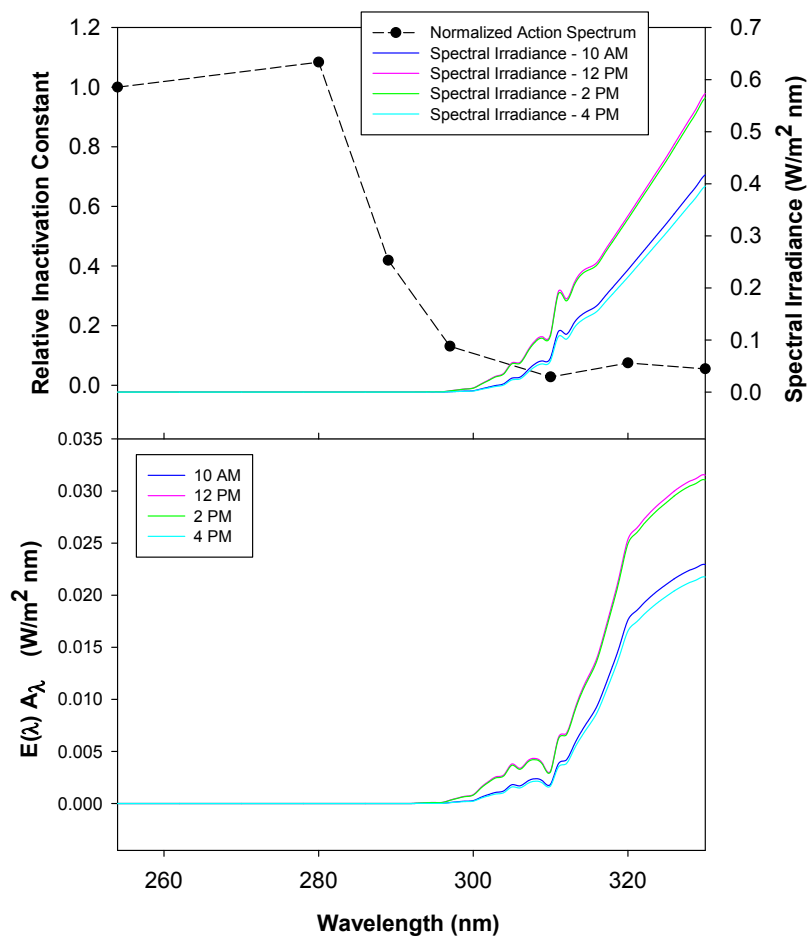
Figure 6.3. Effectiveness spectrum for *C. parvum* on August 1, 2013 in West Lafayette, Indiana.

Results from the effectiveness spectrum for *C. parvum* differ slightly because the available solar irradiance increases again as wavelength increases from 320 nm to 330 nm. In this study, the inactivation at 330 nm was similar to that at 320 nm and more effective than 310 nm, differing from the bacterial studies. Therefore, 330 nm becomes the most effective wavelength for inactivation of *C. parvum* as seen in Figure 6.3.

6.4   Discussion/Conclusions

The effectiveness spectra for both *S. typhimurium* LT2 and *V. harveyi* indicate that the most effective wavelength for inactivation is in the vicinity of 320 nm. This differs from previously published results based on *E. coli* and synthetic spectra, where 310 nm was determined to be the most effective wavelength (Mbonimpa et al., 2012). The effectiveness spectrum for *C. parvum* presents another deviation from the literature suggesting that 330 nm is the most effective wavelength for inactivation. Further investigation of the experimental conditions must be completed to determine whether this is a correct conclusion, or an experimental artifact. The inactivation potential due to DNA absorbance should approach zero for wavelengths above 310 nm. In contrast, spectral irradiance increases sharply from the UVB (290 nm - 320 nm) into the UVA range (320 nm – 380 nm) (Coohill and Sagripanti, 2008; Fisher et al., 2012; Lin et al., 1997). Therefore, increasing inactivation efficiency above 310 nm will have a large impact on a solar inactivation system by inactivation processes other than DNA damage.

The effects of location on resulting effectiveness spectra have not been examined, but will also affect the site-specific system design if they differ from the results obtained for West Lafayette, IN.

CHAPTER 7. RAYTRACING

7.1   Introduction

Photopia is a raytracing software package used for lighting simulations. However, the

basic physics of UV-based processes are identical to those that apply within the visible

portion of the electromagnetic spectrum. Therefore, a raytracing approach can be used to

simulate the spatial distribution of radiant energy in UV-based systems.

Su et al. (2012a) used a raytracing approach to the spatial distribution of radiant energy in

compound parabolic reactors (CPCs), which are described in a general manner in Figure

7.1.
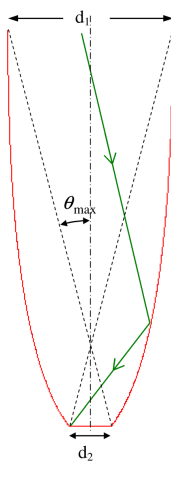
Figure 7.1. Diagram of a generic CPC and its components (Su et al., 2012a).

In this model d_1 represents the aperture of the CPC, d_2 is the width at the bottom of the collector and θ_{max} is the half acceptance angle (Su et al., 2012a).

7.1.1   Inputs

The output from the TUV model (i.e., solar spectral irradiance) can be used as input in a Photopia simulation of a solar process. Converting the TUV output to radiant watts allows for raytracing and system modeling in Photopia of any modeled UVB radiation and it impacts on the receiving model. Within Photopia there are lamp models used for source light, and there is a lamp with a built in function for daylighting models, compatible with TUV data. Daylighting models include skylights, light pipes, windows and important for this project, solar collectors. This function uses a "lamp" based on IESNA RP-21 daylight equations, which accounts for the absolute illuminance from the sun under a given set of conditions. These lamp sources are selected based on their ability to illuminate the entire daylight collector, and they illuminate the outside of the collector as opposed to the other lamps, which illuminate from within (LTI Optics, 2014). For good resolution of the output between 20-50 million rays are used in the model, and there is little resolution improvement past this upper limit (Oh et al., 2013). Resolution can also be improved with and increase in the grid density of the receiving object such as illuminance planes. The output can also be scaled relatively (based on the input), absolutely (based on the output) or per thousand lamp lumens. Therefore, if the output is scaled relatively, the units of the input will be the same as the output, allowing the user to use different units than the default lumens (LTI Optics, 2014).

7.1.2 Outputs

Photopia employs a variety of outputs depending on the user's needs. Either a photometric report can be selected or illuminance on a plane. Illuminance surfaces (e.g., planes or spheres) are defined by their location and grid density, and they are used to describe the illuminance imposed on a specified surface in a grid configuration. The number of lumens that fall into each box are summed and divided by the bin area. Bins correlate to stability and resolution of the results. The higher the number of bins, the better the resolution and the larger the number of rays needed for analysis (LTI Optics, 2014).

According to a study by Su et al., (2012a) output of the software using the daylighting simulation can predict within 1-2% of measured values. If appropriate input parameters are selected, the IES file output can be modeled as accurately as measured conditions (Oh et al., 2013). Conditions are all measured at a certain point in the day, which correlates to a specific angle of the sun in the sky. In another study, the chosen daylight system had a collection efficiency of 68% regardless of the solar altitude angle (Han et al., 2013).

An alternate to using illuminance planes is to model (small) spherical surfaces across cross-sectional areas of the CPC reactor. By placing each spherical particle in its own plane, the illuminance on the plane can be modeled resulting in the fluence rate at a give point within a reactor. The use of small spherical illuminance surfaces is motivated by the formal definition of fluence rate: radiant power per unit area imposed on an infinitesimally-small sphere.

7.1.3 Skylight Simulations

Three-dimensional sun and sky simulations of a model are important to consider because they can take into account non-parallel rays to the plane being assessed, which will play an important role in the output of the system. The Daylighting Simulation Function in Photopia provides a method to account for real atmospheric conditions, such as the altitude of the sun and the weakening of the sun's rays as their path length through the atmosphere increases (Oh et al., 2013; Yu et al., 2014). Further, these models can be set up specific to the atmospheric conditions at the area of study, with a spectrum of wavelengths as opposed to running the model for the most effective wavelength. This would allow for a thorough understanding of solar inactivation due to DNA damage of microorganisms (LTI Optics, 2014).

7.2 Materials & Methods

The geometry of the compound parabolic collector (CPC) used by Mbonimpa (2010) was recreated in Photopia based on the equations that define the profile of a CPC (Equations 7.1 and 7.2) The reactor was designed with a 42 cm aperture, 9.2 cm width for receiving solar radiation and 125 cm length. The interior of the collector was lined with aluminum foil (Mbonimpa et al., 2012).

$$X = \frac{2f * \cos\theta}{(1 - \cos\theta)}$$
Equation 7.1

$$Y = \frac{2f * \sin\theta}{(1 - \cos\theta)}$$
Equation 7.2

(X,Y) = Cartesian coordinates of the CPC profile

θ = angle between the line joining the focus, point on the parabola and x-axis

f = focus of the parabola.

From this design, it was determined that the half acceptance angle of the CPC was 7.5°. This value is important because optimal use of the system will depend on the solar zenith angle. The half acceptance angle was also used to calculate the maximum concentration ratio (C_{max}) of the CPC, which is the ratio of the input and output aperture area calculated by Equation 7.3 (Prapas et al., 1987).

$$C_{max} = \frac{1}{\sin(\theta_{acc})} \qquad \text{Equation 7.3}$$

Where,

C_{max} = is the maximum concentration ratio

θ_{acc} = half acceptance angle (deg).

The concentration ratio calculated for the CPC in this study way 1.07, which is essentially the same concentration ratio of a flat plate (1.0). In collectors with low concentration ratio, the temperature in the system remains between 30-200°C (Abdullahi and Mahmoud, 2013). The boiling point of water falls in the central portion of this temperature range indicating that the thermal component of disinfection can be manipulated.

Running along the bottom of the CPC, where the radiation was focused, was a

borosilicate glass tube, which was modeled as being filled with water (Figure 7.2). The

tube had a 5 cm outer diameter, 5 mm wall thickness and 125 cm length (Mbonimpa et al.,

2012). Two interfaces were modeled with the reactor to appropriately evaluate the

transitions between different materials with varying reflective properties. The inner

surface was modeled as a wavelength dependent borosilicate glass-water interface, and

the outer pipe was modeled with a borosilicate glass material set up with transmission

properties at each wavelength of study.
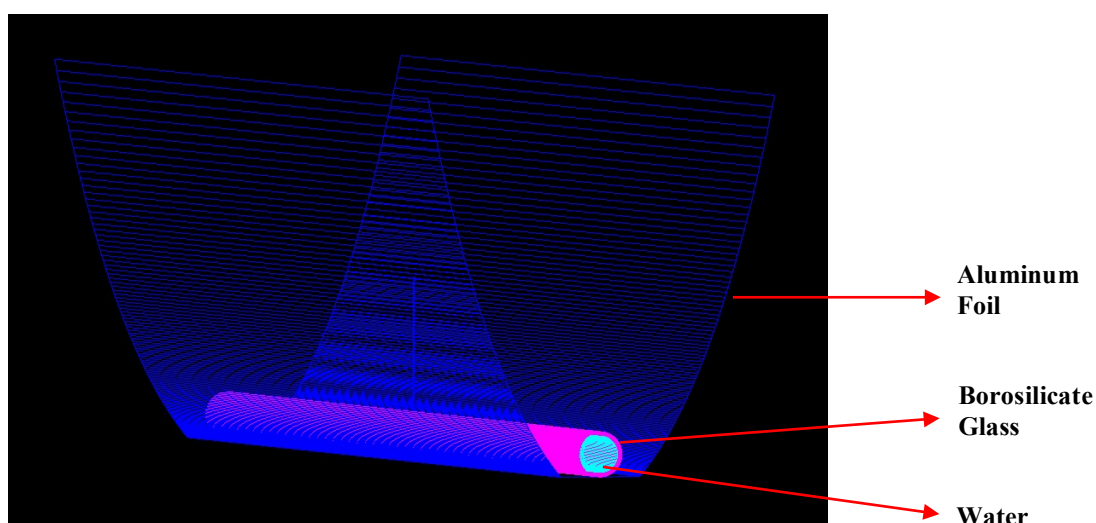
Figure 7.2. Photopia model of the CPC with borosilicate glass transport tube.

Input parameters to the model included refractive indexes for water and borosilicate glass,

as well as an extinction coefficient for water. These values will change for each

wavelength, so new parameter estimates must be developed for each wavelength-specific

run of the Photopia model. The extinction coefficient (κ) for borosilicate glass at each

Wavelength, with Fresnel reflections included, was also calculated using the material's

index of refraction (n), thickness, transmittance (T) and incidence angle of transmittance

(θ_i). The series of equations below describe the relationship between these parameters to

determine κ.

$$\theta_r = \sin^{-1}\left(\frac{\sin(\theta_i)}{n}\right)$$ Equation 7.3

$$t_t = \frac{h}{\theta_r}$$ Equation 7.4

$$R_{Par} = \frac{\tan(\theta_i - \theta_r)^2}{\tan(\theta_i + \theta_r)^2}$$ Equation 7.5

$$R_{Perp} = \frac{\sin(\theta_i - \theta_r)^2}{\sin(\theta_i + \theta_r)^2}$$ Equation 7.6

$$R_{avg} = \frac{R_{Par} + R_{Perp}}{2}$$ Equation 7.7

$$\kappa = \left(-1 + 2R_{avg} - R_{avg}^2\right) +$$

$$\left[\frac{}{\sqrt{1 - 4R_{avg} + 6R_{avg}^2 - 4R_{avg}^3 + R_{avg}^4 + 4T^2 R_{avg}^2}}\right.$$

$$\left. - \frac{\ln\left(0.5\left(\frac{-1 + 2R_{avg} - R_{avg}^2 + \sqrt{1 - 4R_{avg} + 6R_{avg}^2 - 4R_{avg}^3 + R_{avg}^4 + 4h^2 \cdot R_{avg}^2}}{h \cdot R_{avg}^2}\right)\right)}{t_t}\right] \quad \text{Equation 7.8}$$

Where,

θ_i = incidence angle (radians)

θ_r = angle of refraction (radians)

t_t = travel time (s)

R_{Par} = parallel reflectance

R_{Perp} = perpendicular reflectance

R_{avg} = average of R_{par} and R_{perp}

h = thickness (cm).

If this equation yields a result less than 0, the transmission is greater than the Fresnel

reflections and there is no extinction coefficient.

To model the sun, a "numerical lamp" was selected at a size that would illuminate the entire surface of the CPC. Output from this "lamp" was defined as being equal to ambient solar irradiance. The solar zenith angle for the day of this simulation (August 1, 2013) at noon was determined with the TUV data set and used as the lamp angle in the model. This was verified by the USDA UVB monitoring network, which indicated an angle of 22.72^o, equating to a 67.28^o angle above horizontal for the sun lamp. Established sun lamp models with pre-defined solar angles are available at 10° intervals in Photopia, so a sun lamp at 70° was used in this study. Output from the TUV model for West Lafayette, IN at 300.5 nm, 305 nm, 311 nm and 325 nm was scaled by the acceptance area of the CPC and an integration of a 10 nm wavelength range. This 10 nm range was based off of the 10-nm bandpass of the optical filters used in experiments to determine action spectra with the MP lamp. This output was used as an input to Photopia in radiant watts.

7.3   Results

As described above, raytracing was used to simulate the spatial distribution of radiant energy within the prototype CPC reactor system. The output from the TUV simulations or the measured spectral irradiance values from the TUV model or the USDA UVB Monitoring Network can be used as input to the raytracing simulations, but TUV was used in these studies. A schematic of the Photopia model is shown in Figure 7.3, where the sun is at an angle of 70°.

Figure 7.3. Schematic of CPC modeled with the sun lamp at 70°.

The raytracing simulation was also developed to include spherical receptor surfaces in the locations within the computational domain corresponding to several cross-sections of the transmission tube indicated (Figure 7.4). The portion of the figure on the right illustrates the spherical receptors (diameter = 4 mm) in the center cross-section of the CPC. Spherical receptors were selected to most appropriately represent the definition of fluence rate, which is the incident light from all directions onto a sphere divided by the cross-sectional area of the sphere (Coohill and Sagripanti, 2008). This quantifies total radiant power at the selected points throughout the system.
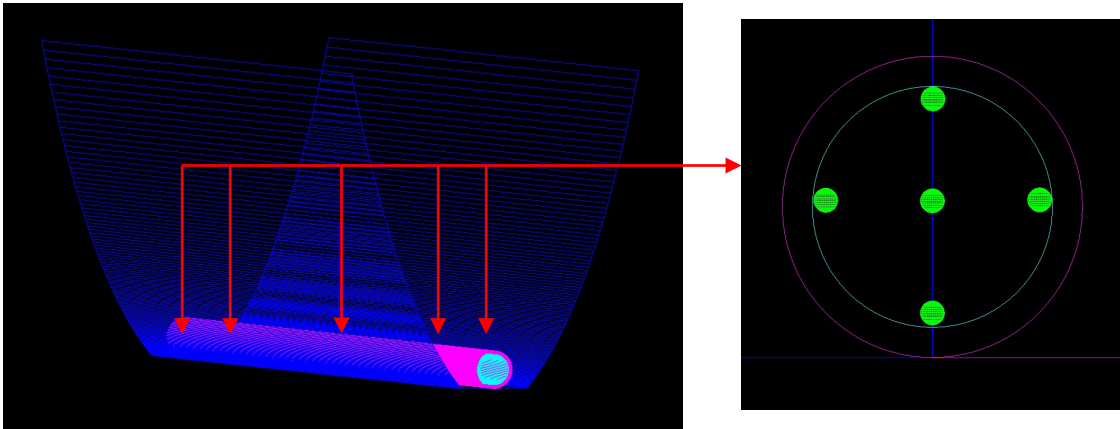
Figure 7.4. Locations at which the spherical receptors were places within the CPC reactor.

Figure 7.5 provides a schematic illustration of the system as simulated in Photopia. The model includes a square source (upper left) that was used to simulate solar irradiance, the CPC, and the UVB-transparent transmission tube, located in the focus of the CPC cross-section. The simulations conducted to date have involved direct radiation only. It is possible to include diffuse radiation in the model simulations as well; however, this involves features of the raytracing software that have not yet been implemented for these simulations.
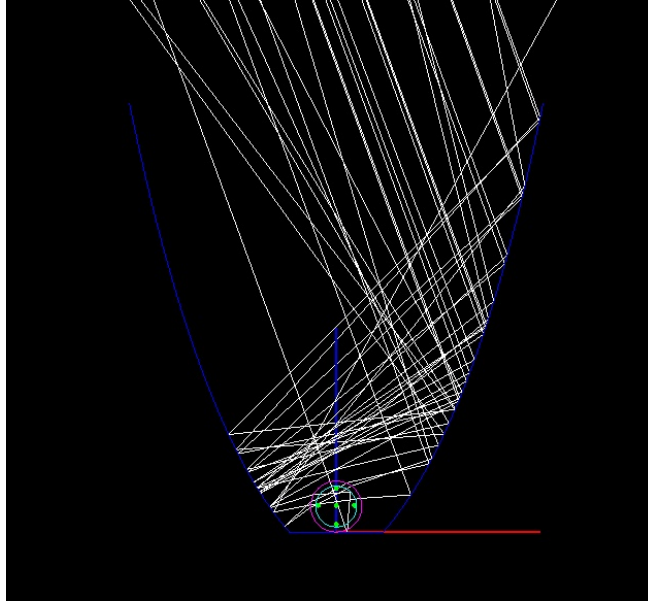
Figure 7.5. Solar radiation focused within the CPC on August 1, 2013 in West Lafayette, IN at an incident angle of 70°.

In Figure 7.5, the same trend reported by Su et al. (2012b) was observed, where solar

radiation was not focused on a point at the bottom of the reactor when the zenith angle of

the sun was outside the half acceptance angle of the CPC. The solar zenith angle of 20°,

which was modeled here, is outside of the 7.5° half acceptance angle. Therefore, the rays

are concentrated above the borosilicate glass tube in the bottom of the CPC. Modeling of

the current configuration indicated that the most effective portion of the central cross-

section of the borosilicate glass tube was the left sphere (located at the center vertical and

horizontal cross-sections of the borosilicate glass tube at the furthest left point), and the

least effective was the point at the bottom of the tube.

Using this same amount of input radiation, the solar zenith angle was shifted to 90˚,

would represent the optimum condition for use of this system. An incident angle of 90°

may be maintained with the inclusion of simple solar tracking hardware for the CPC.

Figure 7.6 illustrates the results of this simulation. In general, amplification of incident

solar irradiance is far more effective for the incident angle of 90° than 70°. This suggests

that the systems should be expected to perform much better at locations near the equator

than in West Lafayette, IN. These results also indicate that the inclusion of simple solar

tracking hardware may allow for substantial improvements in process performance with

the CPC system.
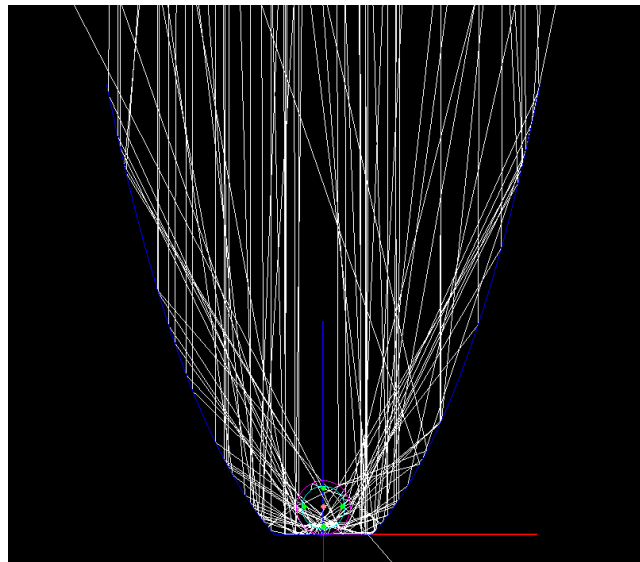
Figure 7.6. Solar radiation focused within the CPC on August 1, 2013 in West Lafayette,
IN at an incident angle of 90˚.

The results of these simulations are illustrated in Figure 7.7, where amplification ratio has

been defined by the output fluence rate at a given location divided by the input fluence

rate. The input to this model was the integration of available spectral irradiance in West Lafayette, IN on August 1, 2013 between the wavelengths of 305-315 nm at noon converted to radiant watts based on the acceptance area of the CPC. The same radiant input used in the 70° model was used in the 90° model for direct comparison of the effects of solar zenith angle on fluence rate. The least and most effective fluence rates within the reactor changed with solar zenith. At 70° the most effective point modeled was the left of the reactor and the least effective is the bottom. When the zenith angle increased to 90°, the most effective position modeled became the bottom of the reactor and the least effective was the top of the reactor. The results of this simulation indicate that the local fluence rate will vary considerably across the cross-section of the transmission tube. As seen in the raytracing results (Figures 7.5 and 7.6), the modeled locations within the reactor may not appropriately model the total amplification of the system; the modeled spheres were not located in at the focal point of the incoming rays. These findings suggest that performance in this system may be improved by inclusion of a static mixing device upstream of the transmission tube. These results also indicate opportunities for selection of a transmission tube with dimensions that match the amplified solar signal.
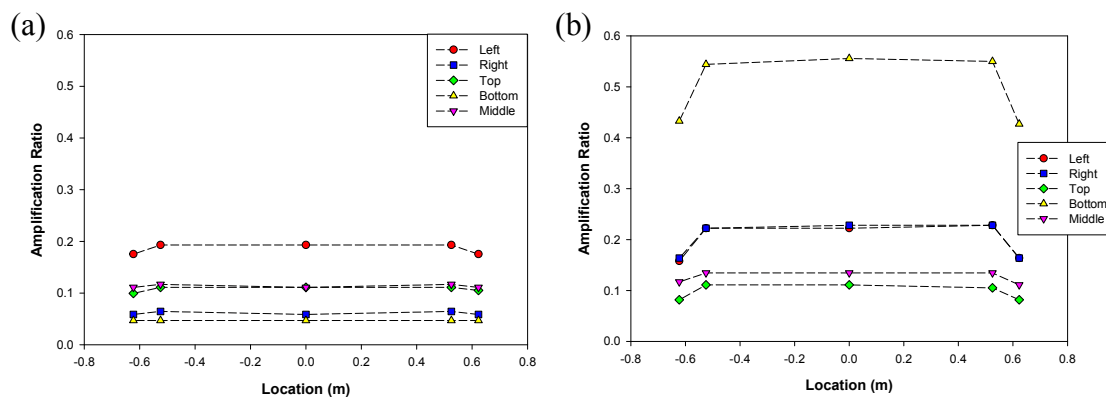
Figure 7.7. Fluence rates within the transmission tube for (a) 70° and (b) 90°.

7.4   Discussion/Conclusion

The orientation of a CPC relative to incident solar radiation will need to be adjusted as

the incident solar radiation moves outside of the half acceptance angle (Gudekar et al.,

2013). This behavior was validated by the results of this study by adjusting the zenith

angle of the lamp representing the sun. It has been shown that at a half acceptance angle

of 7°, the shortest period that the system can go without adjustment is 13 days (Rabl,

1980), and when this angle increases to 8° the time increases to 16 days. This would

result in 14-20 adjustments of the system per year (Rabl, 1980). So with an increase in

the half acceptance angle of the CPC or a tracking system, the adjustments of the system

can be altered so that it works more efficiently under a range of conditions. The locations

throughout the reactor at which most of the radiation is focused will be studied to

understand the possible amplification within the reactor if the radiation is actually

focused within the borosilicate glass tube.

CHAPTER 8. FUTURE WORK

Detailed measurements of the irradiance distribution across the optically-filtered MP

beam will be conducted. Analysis will be conducted to determine average irradiance from

the beam compared to irradiance calculated from one central measurement of the beam.

Once this is complete, finalized effectiveness spectra and fluence rates from Photopia

results will be integrated with computational fluid dynamics (CFD) modeling of the

reactor. This will create an understanding of the disinfection properties within the reactor,

and it will allow for the development of process controls for the system.

For employment of process controls, the available solar irradiance must be continuously

monitored. Tests will be performed to evaluate the sensitivity of multiple UVB sensing

devices at the Purdue Agronomy Farm at the same height and orientation as the USDA

UVB monitoring device located there. Data from the portable UV sensor will be

compared to that of the USDA device to evaluate sensitivity. Once process controls have

been developed the prototype CPC will be tested in field studies. Its performance will be

predicted and the experimental output will be compared to this data for verification of

scale-up potential.

LIST OF REFERENCES

LIST OF REFERENCES

193-299nm Standard Bandpass Optical Filters [WWW Document], n.d. . Andover Corp. URL https://www.andovercorp.com/products/bandpass-filters/standard/193-299nm/ (accessed 3.29.16).

300-399nm Standard Bandpass Optical Filters [WWW Document], n.d. . Andover Corp. URL https://www.andovercorp.com/products/bandpass-filters/standard/300-399nm/ (accessed 3.29.16).

Abdullahi, B., Mahmoud, S., 2013. Effect of Acceptance Angle on the Design and Performance of a Heat Pipe Based Compound Parabolic Collector at Kano, Nigeria, in: International Conference on Renewable Energies and Power Quality. pp. 2–7.

Ahmad, Z., McClain, C.R., Herman, J.R., Franz, B. a, Kwiatkowska, E.J., Robinson, W.D., Bucsela, E.J., Tzortziou, M., 2007. Atmospheric Correction for NO2 Absorption in Retrieving Water-leaving Reflectances from the SeaWiFS and MODIS Measurements. Appl. Opt. 46, 6504–12.

Alexandrov, M.D., Kiedron, P., Michalsky, J.J., Hodges, G., Flynn, C.J., Lacis, A. a, 2007. Optical Depth Measurements by Shadow-band Radiometers and their Uncertainties. Appl. Opt. 46, 8027–8038.

Alifano, P., Nassisi, V., Siciliano, M. V., Talà, A., Tredici, S.M., 2011. Unexpected Photoreactivation of Vibrio harveyi Bacteria Living in Ionization Environment. J. Appl. Phys. 109, 1–5.

Beck, S.E., Wright, H.B., Hargy, T.M., Larason, T.C., Linden, K.G., 2015. Action Spectra for Validation of Pathogen Disinfection in Medium-pressure Ultraviolet (UV) Systems. Water Res. 70, 27–37.

Bernhard, G., Mayer, B., Seckmeyer, G., Moise, A., 1997. Measurements of Spectral Solar UV Irradiance in Tropical Australia. J. Geophys. Res. 102, 8719–8730.

Bigelow, D.S., Slusser, J.R., Beaubien, A.F., Gibson, J.H., 1998. The USDA Ultraviolet Radiation Monitoring Program. Bull. Am. Meteorol. Soc. 79, 601–615.

Blatchley, E.R., 1997. Numerical Modelling of UV Intensity: Application to Collimated-beam Reactors and Continuous-flow Systems. Water Res. 31, 2205–2218.

Blatchley, E.R., Dumoutier, N., Halaby, T.N., Levi, Y., Laîné, J.M., 2001. Bacterial Responses to Ulraviolet Radiation. Water Sci. Technol. 43, 179–186.

Blatchley, E.R., Meeusen, A., Aronson, A.I., Brewster, L., 2005. Spores by Ultraviolet or Gamma Radiation. J. Environ. Eng. 131, 1245–1252.

Bolton, J.R., Linden, K.G., 2003. Standardization of Methods for Fluence (UV Dose) Determination in Bench-Scale UV Experiments. J. Environ. Eng. 129, 209–215.

Buntoung, S., Webb, a. R., 2010. Comparison of erythemal UV irradiances from Ozone Monitoring Instrument (OMI) and ground-based data at four Thai stations. J. Geophys. Res. Atmos. 115, 1–8.

Campbell, A.T., Robertson, L.J., Snowball, M.R., Smith, H. V., 1995. Inactivation of Oocysts of Cryptosporidium parvum by Ultraviolet Irradiation. Water Res. 29, 2583–2586.

Chang, Feng, R., Gao, Z., Gao, W., 2010. Skin Cancer Incidence is Highly Associated with Ultraviolet-B Radiation History. Int. J. Hyg. Environ. Health 213, 359–368.

Chang, J.C.H., Ossoff, S.F., Lobe, D.C., Dorfman, M.H., Dumais, C.M., Qualls, R.G., Johnson, J.D., 1985. UV inactivation of pathogenic and indicator microorganisms. Appl. Environ. Microbiol. 49, 1361–1365.

Chen, R.Z., Craik, S.A., Bolton, J.R., 2009. Comparison of the Action Spectra and Relative DNA Absorbance Spectra of Microorganisms: Information Important for the Determination of Germicidal Fluence (UV dose) in an Ultraviolet Disinfection of Water. Water Res. 43, 5087–5096.

Clarke, A., Kapustin, V., 2010. Hemispheric Aerosol Vertical Profiles: Anthropogenic Impacts on Optical Depth and Cloud Nuclei. Science (80-.). 329, 1488–1492.

Coohill, T.P., 1996. Stratospheric Ozone Loss, Ultraviolet Effects and Action Spectroscopy. Adv. Sp. Res. 18, 27–33.

Coohill, T.P., 1994. Exposure Response Curves Action Spectra and Amplification Factors, in: Stratospheric Ozone Depletion/UV-B Radiation in the Biosphere. pp. 57–62.

Coohill, T.P., 1991. Action Spectra Again? Photochem. Photobiol. 54, 859–870.

Coohill, T.P., Sagripanti, J.L., 2008. Overview of the Inactivation by 254 nm Ultraviolet Radiation of Bacteria with Particular Relevance to Biodefense. Photochem. Photobiol. 84, 1084–1090.

Czyz, A., Wróbel, B., Węgrzyn, G., 2000. Vibrio harveyi Bioluminescence Plays a Role in Stimulation of DNA Repair. Microbiology 146, 283–288.

Das, G., Das, J., 1983. Radiation-sensitive Mutant of Hyper- toxinogenic Strain 569B of Vibrio cholerae. Mutat. Res. 109, 21–30.

Das, G., Sil, K., Das, J., 1981. Repair of Ultraviolet-light-induced DNA Damage in Vibrio cholerae. Biochem. Biophys. Acta 655, 413–420.

Edlén, B., 1966. The Refractive Index of Air. Metrologia 2, 71–80.

Fisher, M.B., Iriarte, M., Nelson, K.L., 2012. Solar Water Disinfection (SODIS) of Escherichia coli, Enterococcus spp., and MS2 coliphage: Effects of Additives and Alternative Container Materials. Water Res. 46, 1745–1754.

Fisher, M.B., Keenan, C.R., Nelson, K.L., Voelker, B.M., 2008. Speeding up Solar Disinfection (SODIS): Effects of Hydrogen Peroxide, Temperature, pH, and Copper plus Ascorbate on the Photoinactivation of E. coli. J. Water Health 6, 35.

GEMS, 2013. The Global Enteric Multicenter Study Implications for Diarrheal Disease Control.

Gennari, M., Ghidini, V., Caburlotto, G., Lleo, M.M., 2012. Virulence Genes and Pathogenicity Islands in Environmental Vibrio Strains Nonpathogenic to Humans. FEMS Microbiol. Ecol. 82, 563–573.

Ghude, S.D., Singh, S., Kulkarni, P.S., Kumar, A., Jain, S.L., Singh, R., Arya, B.C., Shahnawaz, 2008. Observations and Model Calculations of Direct Solar UV Irradiances in the Schirmacher Region of East Antarctica. Int. J. Remote Sens. 29, 5907–5921.

Gómez-Couso, H., Fontán-Sainz, M., Ares-Mazás, E., 2010. Thermal Contribution to the Inactivation of Cryptosporidium in Plastic Bottles During Solar Water Disinfection Procedures. Am. J. Trop. Med. Hyg. 82, 35–39.

Grady, C.A., Kipkorir, E.C., Nguyen, K., Blatchley III, E.R., 2015. Microbial Quality of Improved Drinking Water Sources: Evidence from Western Kenya and Southern Vietnam. J. Water Heal. 13, 607–612.

Greenfield, J.A., Park, P.S., Farahani, E., Malik, S., Vieth, R., McFarlane, N.A., Shepherd, T.G., Knight, J.A., 2012. Solar Ultraviolet-B Radiation and Vitamin D: A Cross-sectional Population-based Study Using Data from the 2007 to 2009 Canadian Health Measures Survey. BMC Public Health 12, 660.

Gudekar, A.S., Jadhav, A.S., Panse, S. V., Joshi, J.B., Pandit, A.B., 2013. Cost effective Design of Compound Parabolic Collector for Steam Generation. Sol. Energy 90, 43–50.

Guo, M., Hu, H., Bolton, J.R., El-Din, M.G., 2009. Comparison of Low- and Medium-Pressure Ultraviolet Lamps: Photoreactivation of Escherichia coli and Total Coliforms in Secondary Effluents of Municipal Wastewater Treatment Plants. Water Res. 43, 815–821.

Han, H.J., Riffat, S.B., Lim, S.H., Oh, S.J., 2013. Fiber Optic Solar Lighting: Functional Competitiveness and Potential. Sol. Energy 94, 86–101.

Hijjawi, N., 2003. In vitro Cultivation and Development of Cryptosporidium in Cell Culture, in: Cryptosporidium: From Molecules to Disease. pp. 233–249.

Hijnen, W.A.M., Beerendonk, E.F., Medema, G.J., 2006. Inactivation Credit of UV Radiation for Viruses, Bacteria and Protozoan (oo)cysts in Water: A Review. Water Res. 40, 3–22.

Hooton, S.P.T., Timms, A.R., Moreton, J., Wilson, R., Connerton, I.F., 2013. Complete Genome Sequence of Salmonella enterica Serovar Typhimurium U288. Genome Announc. 1, 2010–2011.

Hoyer, O., 1998. Testing Performance and Monitoring of UV Systems for Drinking Water Disinfection. Water Supply 16, 424–429.

Joe, A., Verdon, R., Tzipori, S., Keusch, G.T., Ward, H.D., 1998. Attachment of Cryptosporidium parvum Sporozoites to Human Intestinal Epithelial Cells. Infect. Immun. 66, 3429–3432.

Johnson, A.M., 2015. Image of Cryptosporidium parvum Focus in HCT-8 Cells.

Johnson, A.M., Di Giovanni, G.D., Rochelle, P.A., 2012. Comparison of Assays for Sensitive and Reproducible Detection of Cell Culture-infectious Cryptosporidium parvum and Cryptosporidium hominis in Drinking Water. Appl. Environ. Microbiol. 78, 156–162.

Khaengraeng, R., Reed, R.H., 2005. Oxygen and Photoinactivation of Escherichia coli in UVA and Sunlight. J. Appl. Microbiol. 99, 39–50.

Khokhlov, V.N., Romanova, A. V., 2011. NAO-induced Spatial Variations of Total Ozone Column Over Europe at Near-synoptic Time Scale. Atmos. Environ. 45, 3360–3365.

King, B.J., Keegan, A.R., Phillips, R., Fanok, S., Monis, P.T., 2012. Dissection of the Hierarchy and Synergism of the Bile Derived Signal on Cryptosporidium parvum Excystation and Infectivity. Parasitology 139, 1533–1546.

Kozakiewicz, J., Gajewska, M., Łyzeń, R., Czyz, A., Węgrzyn, G., 2005. Bioluminescence-mediated Stimulation of Photoreactivation in Bacteria. FEMS Microbiol. Lett. 250, 105–110.

Lin, L., Cook, D.N., Wiesehahn, G.P., Alfonso, R., Behrman, B., Cimino, G.D., Corten, L., Damonte, P.B., Dikeman, R., Dupuis, K., Fang, Y.M., Hanson, C. V., Hearst, J.E., Lin, C.Y., Londe, H.F., Metchette, K., Nerio, A.T., Pu, J.T., Reames, A.A., Rheinschmidt, M., Tessman, J., Isaacs, S.T., Wollowitz, S., Corash, L., 1997. Photochemical Inactivation of Viruses and Bacteria in Platelet Concentrates by Use of a Novel Psoralen and Long-wavelength Ultraviolet Light. Transfusion 37, 423–435.

Linden, K.G., Mofidi, A., 2004. Disinfection Efficiency and Dose Measurement of Polychromatic UV Light.

Linden, K.G., Shin, G., Sobsey, M.D., 2001. Comparative Effectiveness of UV Wavelengths for the Inactivation of Cryptosporidium parvum Oocysts in Water. Water Sci. Technol. 43, 171–174.

LTI Optics, 2014. Photopia User's Guide.

Luzi, S., Tobler, M., Suter, F., Meierhofer, R., 2016. SODIS Manual [WWW Document]. Swiss Fed. Inst. Aquat. Sci. Technol.

Madronich, S., 2014. TUV 5.2 User's Guide.

Madronich, S., Wagner, M., Groth, P., 2011. Influence of Tropospheric Ozone Control on Exposure to Ultraviolet Radiation at the Surface. Environ. Sci. Technol. 45, 6919–23.

Mamane-Gravetz, H., Linden, K.G., Cabaj, A., Sommer, R., 2005. Spectral Sensitivity of Bacillus subtilis Spores and MS2 Coliphage for Validation Testing of Ultraviolet Reactors for Water Disinfection. Environ. Sci. Technol. 39, 7845–7852.

Mbonimpa, E.G., 2010. Disinfection of Drinking Water Using Solar UV: A Low Cost System Application in Developing Countries. Purdue University.

Mbonimpa, E.G., Vadheim, B., Blatchley III, E.R., 2012. Continuous-flow Solar UVB Disinfection Reactor for Drinking Water. Water Res. 46, 2344–54.

McGuigan, K., Samaiyar, P., Preez, M., Conroy, R., 2011. High Compliance Randomized Controlled Field Trial of Solar Disinfection of Drinking Water and Its Impact on Childhood Diarrhea in Rural Cambodia. Environ. Sci. Technol. 45, 7862–7867.

McKinlay, A.F., Diffey, B.L., 1987. A Reference Action Spectrum for Ultraviolet Induced Erythema in Human Skin, CIE Research Note. CIE 6, 17–22.

Motohka, T., Nasahara, K.N., Murakami, K., Nagai, S., 2011. Evaluation of Sub-pixel Cloud Noises on MODIS Daily Spectral Indices Based on in situ Measurements. Remote Sens. 3, 1644–1662.

NASA, 2016. OMI/Aura Sulfer Dioxide (SO2) Total Column Daily L3 Best Pixel Global 0.25deg Lat/Lon Grid V003 (OMSO2e) at GES DISC [WWW Document]. URL http://gcmd.nasa.gov/KeywordSearch/Metadata.do?Portal=daacs&KeywordPath=Pa rameters%7CHUMAN+DIMENSIONS%7CENVIRONMENTAL+IMPACTS&Ori gMetadataNode=GCMD&EntryId=GES_DISC_OMSO2e_V003&MetadataView=F ull&MetadataType=0&lbnode=mdlb3

NASA, 2012. Ozone Monitoring Instrument (OMI) Data User's Guide.

O'Connor, K., Fletcher, S.A., Csonka, L.N., 2009. Increased Expression of Mg(2+) Transport Proteins Enhances the Survival of Salmonella enterica at High Temperature. Proc. Natl. Acad. Sci. U. S. A. 106, 17522–17527.

O'Neill, M., Chen, A., Murray, N.E., 1997. The Restriction-modification Genes of Escherichia coli K-12 May not be Selfish: They do not Resist Loss and are Readily Replaced by Alleles Conferring Different Specificities. Proc. Natl. Acad. Sci. U. S. A. 94, 14596–601.

Oates, P.M., Shanahan, P., Polz, M.F., 2003. Solar disinfection (SODIS): Simulation of Solar Radiation for Global Assessment and Application for Point-of-use Water Treatment in Haiti. Water Res. 37, 47–54.

Oh, S.J., Chun, W., Riffat, S.B., Jeon, Y. Il, Dutton, S., Han, H.J., 2013. Computational Analysis on the Enhancement of Daylight Penetration into Dimly Lit Spaces: Light Tube vs. Fiber Optic Dish Concentrator. Build. Environ. 59, 261–274.

Onda, K., Lobuglio, J., Bartram, J., 2012. Global access to safe water: Accounting for water quality and the resulting impact on MDG progress. Int. J. Environ. Res. Public Health 9, 880–894.

Palancar, G.G., Toselli, B.M., 2004. Effects of meteorology and tropospheric aerosols on UV-B radiation: A 4-year study. Atmos. Environ. 38, 2749–2757.

Prapas, D.E., Norton, B., Probert, S.D., 1987. Optics of Parabolic-trough, Solar-energy Collectors, Possessing Small Concentration Ratios. Sol. Energy 39, 541–550.

Rabl, A., 1980. Concentrating Collectors, in: Solar Energy Technology Handbook Part A - Engineering Fundamentals. pp. 257–343.

Ramachandran, S., Kedia, S., Srivastava, R., 2012. Aerosol Optical Depth Trends Over Different Regions of India. Atmos. Environ. 49, 338–347.

Rochelle, P.A., Marshall, M.M., Mead, J.R., Johnson, A.M., Korich, D.G., Rosen, J.S., De Leon, R., 2002. Comparison of in vitro Cell Culture and a Mouse Assay for Measuring Infectivity of Cryptosporidium parvum. Appl. Environ. Microbiol. 68, 3809–17.

Schiebener, P., Straub, J., Levelt Sengers, J.M.H., Gallagher, J.S., 1990. Refractive Index of Water and Steam as Function of Wavelength, Temperature and Density. J. Phys. Chem. Ref. Data 19, 677–717.

Setlow, R.B., 1974. The Wavelengths in Sunlight Effective in Producing Skin Cancer: A Theoretical Analysis. Proc. Natl. Acad. Sci. U. S. A. 71, 3363–3366.

Severin, B.F., Suidan, M.T., Engelbrecht, R.S., 1983. Kinetic Modeling of U.V. Disinfection of Water. Water Res. 17, 1669–1678.

Shin, G., Linden, K.G., Arrowood, M.J., Sobsey, M.D., 2001. Low-Pressure UV Inactivation and DNA Repair Potential of Cryptosporidium parvum Oocysts. Appl. Environ. Microbiol. 67, 3029–3032.

Sifuentes, L.Y., Di Giovanni, G.D., 2007. Aged HCT-8 Cell Monolayers Support Cryptosporidium parvum Infection. Appl. Environ. Microbiol. 73, 7548–7551.

Sigma-Aldrich, 2010. Cell Quantification.

Slifko, T.R., Friedman, D., Rose, J.B., Jakubowski, W., 1997. An In Vitro Method for Detecting Infectious Cryptosporidium Oocysts with Cell Culture. Appl. Environ. Microbiol. 63, 3669–3675.

Su, Pei, G., Riffat, S.B., Huang, H., 2012a. A Novel Lens-Walled Compound Parabolic Concentrator for Photovoltaic Applications. J. Sol. Energy Eng. 134, 021010–021010–7.

Su, Riffat, Pei, 2012b. Comparative Study on Annual Solar Energy Collection of a Novel Lens-walled Compound Parabolic Concentrator (Lens-walled CPC). Sustain. Cities Soc. 4, 35–40.

Sutherland, J.C., 2002. Biological Effects of Polychromatic Light. Photochem. Photobiol. 76, 164.

UNICEF/WHO, 2011. Drinking Water Equity, Safety and Sustainability, JMP Thematic Report on Drinking Water.

USDA, n.d. UV-B Monitoring and Research Program at Colorado State University [WWW Document]. UV-B Monit. Res. Progr. URL http://uvb.nrel.colostate.edu/UVB/uvb_network.jsf

Wang, X., Gao, W., Slusser, J.R., Davis, J., Gao, Z., Scott, G., Olson, B., Krotkov, N., Xu, M., Liang, X.-Z., 2006. Spectral Distribution of UV-B Irradiance Derived by Synthetic Model Compared with Simulation Results of TUV and Ground Measurements. Proc. SPIE 6298, 62980L–62980L–9.

Wang, X., Gao, W., Slusser, J.R., Davis, J., Olson, B., Janssen, S., Janson, G., Durham, B., Tree, R., Deike, R., 2008. USDA UV-B Monitoring System: An Application of Centralized Architecture. Comput. Electron. Agric. 64, 326–332.

WHO, 1997. Guidelines for Drinking-water Quality. WHO 3, 78.

Xu, M., Liang, X.-Z., Gao, W., Slusser, J., Kunkel, K., 2006. Validation of the TUV Module in CWRF Using USDA-UVB Network Observations. Proc. SPIE 6298.

Ye, Z., Koutchma, T., Parisi, B., Larkin, J., Forney, L.J., 2007. Ultraviolet Inactivation Kinetics of Escherichia coli and Yersinia pseudotuberculosis in Annular Reactors. J. Food Sci. 72.

Yu, X., Su, Y., Zheng, H., Riffat, S., 2014. A Study on Use of Miniature Dielectric Compound Parabolic Concentrator (dCPC) for Daylighting Control Application. Build. Environ. 74, 75–85.

APPENDICES

Appendix A   Andover Corporation 10-nm Bandpass Filters

10-nm bandpass filters with a 50-nm diameter from Andover Corporation were used at

the bottom of the MP collimated beam. These filters were used at 280, 289, 297, 310, 320

and 330 nm, where these values were the center wavelength transmitted by the filter.

These filters were used with the reflective side facing the collimated beam. These optical

filters work the same way regardless of orientation, but the reflective surface protects the

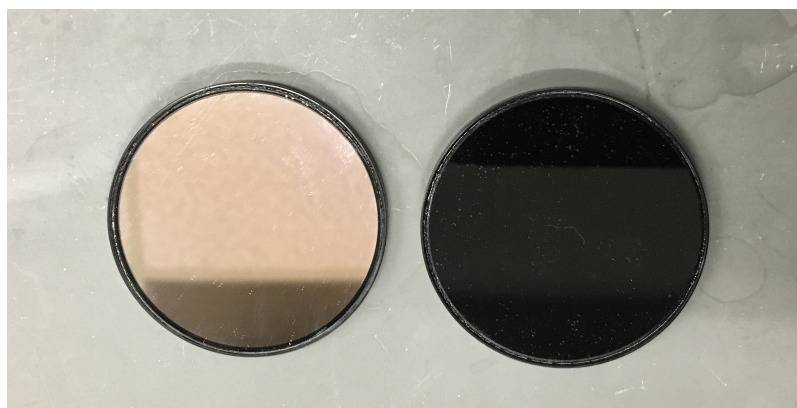optical components of the filter for increased life span.

Figure A 1. Comparison of two sides of optical filter, where the more reflective side (left)
was oriented upwards towards the collimated beam.

The filters are classified as Filter Type 7 by Andover Corporation as shown in Figure A 2

and Filter Type 3 represented in Figure A 3. The following figures represent the

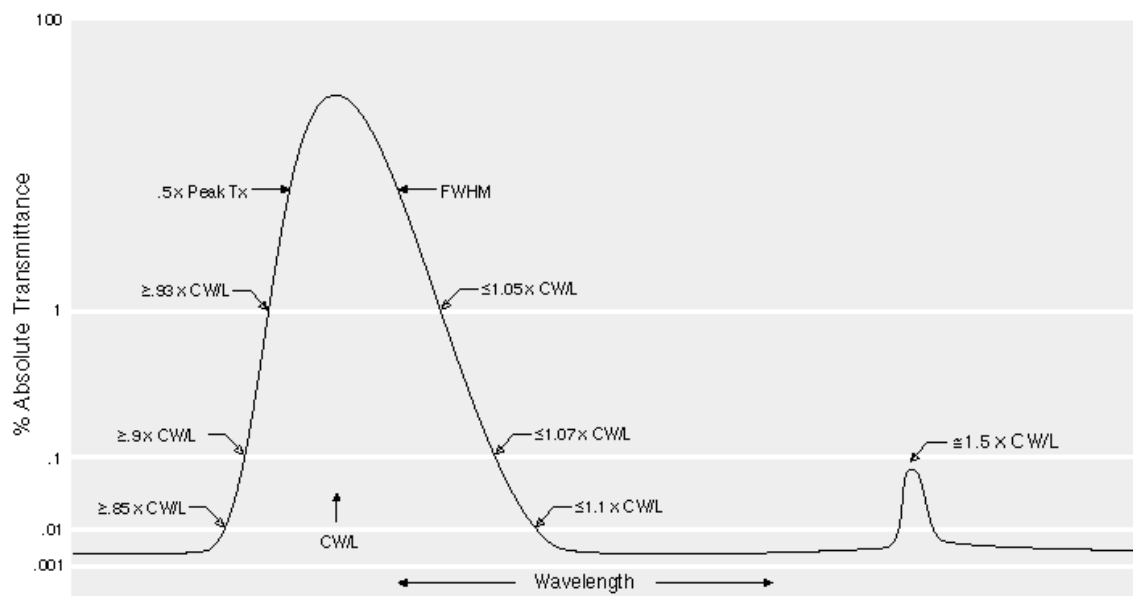wavelengths allowed to pass through each filter at each wavelength.

Figure A 2. Filter Type 7 from Andover Corporation (280, 289, 297, 310 nm) ("193-299nm Standard Bandpass Optical Filters," n.d.).
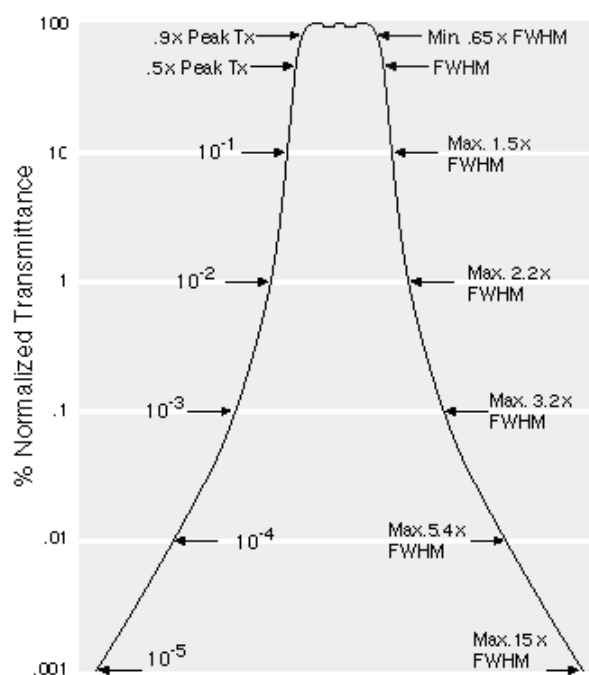

Figure A 3. Filter Type 3 from Andover Corporation (320 and 330 nm) ("300-399nm Standard Bandpass Optical Filters," n.d.).
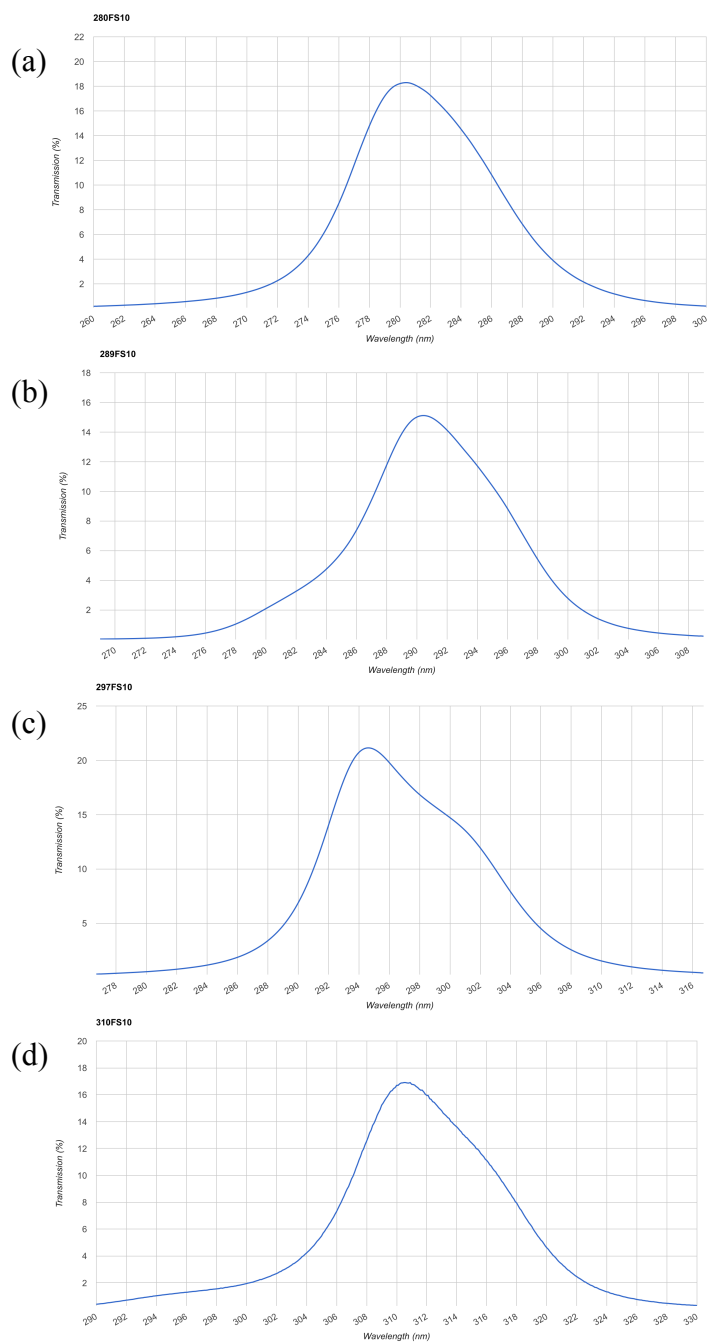
Figure A 4. Plot of transmittance from filters (Type 7) used with MP lamp (a) 280 nm (b) 289 nm (c) 297 nm (d) 310 nm ("193-299nm Standard Bandpass Optical Filters," n.d., "300-399nm Standard Bandpass Optical Filters," n.d.).
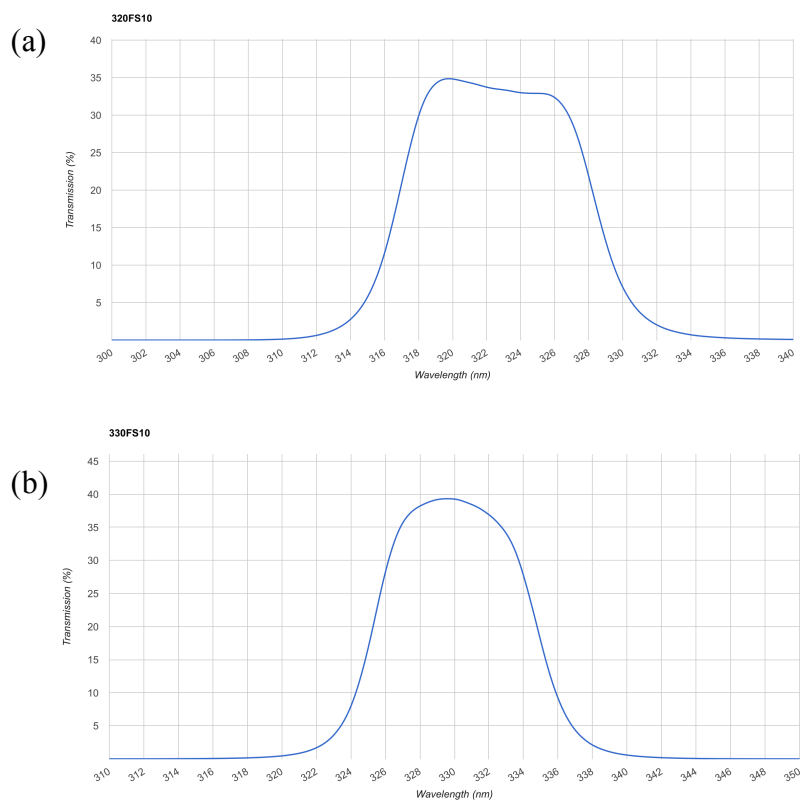
Figure A 5. Plot of transmittance from filters (Type 3) used with MP lamp (a) 320 nm (b) 330 nm ("300-399nm Standard Bandpass Optical Filters," n.d.).

Appendix B   MATLAB Code

MATLAB was used to generate best-fit lines for the graphs in chapter 4 by minimizing

the RSS value.

Salmonella typhimurium LT2

```matlab
% USER INPUTS
D1 = [0,65,131,196,262,327,393,458,524];
NoN0_exp1 = [1,0.859,1.01,1.31,0.615,1.13,1.39,2.15,2.83];

D2 = [0,13,26,39,52,65,78,91,104];
NoN0_exp2 = [1,0.667,0.529,0.373,0.255,0.23,0.135,0.0853,0.0471];

D3 = [0,13,26,39,52,65,78,91,104];
NoN0_exp3 = [1,0.667,0.529,0.373,0.255,0.23,0.135,0.0853,0.0471];

D = [D1,D2,D3];
NoN0_exp = [NoN0_exp1,NoN0_exp2,NoN0_exp3];
exp_all = [D;NoN0_exp];
sort_exp = sortrows(exp_all');
D = transpose(sort_exp(:,1));
NoN0_exp = transpose(sort_exp(:,2));


x0 = 0;    % Initial Guess for optimization
nstart = 1;
nend = 30;

markercolor = [0,0,1]; % Marker Color of Plot
markersize = 6; % Marker weight of plot
linewidth = 2; % Width of line
linecolor = [1 0.25 0]; % Color of line
plottitle = 'Salmonella typhimurium LT2 Dose Response at 330 nm'; %
Title of Plot

SAVEPLOT = 1; % 1 Saves PDF of figure, 0 does not save anything
plotnum = 330;  % Save file num
fp = 'D:\Melissa\Maggie\DoseResponseLT2Combined'; % Save file path
```

```matlab
% CALCULATIONS
fdata = zeros(length(nstart:nend),4);   % Contains optimization data
fdata(:,1) = transpose(nstart:nend);
options = optimset('MaxFunEvals',500);      % Limit Fun Evals to 500

ct = 1;
for w=nstart:1:nend  % Hard code n values
    [x,fval,exitflag] = fminsearch(@(x)
LT2(x,w,D,NoN0_exp),x0,options);   % Search for optimal k value for
given n
    fdata(ct,2) = x;            % Optimal k Value
    fdata(ct,3) = fval;        % Optimized cost function value
    fdata(ct,4) = exitflag;  % Save exit flag for reference
    ct = ct + 1;
end

funvals = fdata(:,3);
[RSS,index] = min(funvals);    % Determine min function value
n_opt = fdata(index,1);
k_opt = fdata(index,2);

ymean = mean(log(NoN0_exp));
TSS = sum((log(NoN0_exp)-ymean).^2);

r2 = 1-RSS/TSS;

fprintf('\n\n-----Correlation-------\nRSS = %f\nr^2 = %f\nExit Flag:
%i\n',RSS,r2,fdata(index,4))
fprintf('Optimal k = %f\nOptimal n = %f\n\n',k_opt,n_opt)

D_reg = transpose(linspace(D(1),D(end),1000));
NoN0_reg = zeros(length(D_reg),1);
for p = 1:1:length(D_reg)

    NoN0_reg(p) = 1-(1-exp(-k_opt*D_reg(p))).^n_opt;
end

% PLOT RESULTS
figure(13)
semilogy(D1,NoN0_exp1,'o','MarkerFaceColor',markercolor,'MarkerSize',ma
rkersize,'MarkerEdgeColor',markercolor)
hold on
semilogy(D2,NoN0_exp2,'^','MarkerFaceColor',markercolor,'MarkerSize',ma
rkersize,'MarkerEdgeColor',markercolor)
hold on
semilogy(D3,NoN0_exp3,'s','MarkerFaceColor',markercolor,'MarkerSize',ma
rkersize,'MarkerEdgeColor',markercolor)
hold on
semilogy(D_reg,NoN0_reg,'-','LineWidth',linewidth,'Color',linecolor)
legend('Experimental','Theoretical')
title(plottitle,'FontSize',12,'FontWeight','bold')
```

```matlab
xlabel('Dose (mJ/cm sq.)','FontSize',12,'FontWeight','bold')
ylabel('log(N/N0)','FontSize',12,'FontWeight','bold')
set(gca,'LineWidth',2,'FontSize',10,'FontWeight','bold','Box','on')
set(gcf,'Color',[1 1 1]);


% SAVE PLOT RESULTS
if SAVEPLOT
    print(13,'-dpdf',[fp,num2str(plotnum,'%03i'),'.pdf'])
end
```

Salmonella typhimurium LT2 run file

```matlab
function [f] = LT2(x,n,D,NoN0_exp)


errors = zeros(length(D),1);


for p=1:length(D)


    errors(p) = log(NoN0_exp(p)) - log(1-(1-exp(-x*D(p)))^n);
end



f = sum(errors.^2);




end
```

Vibrio harveyi

```matlab
% USER INPUTS
D1 = [0,57,115,172,230,345,460,460];
NoN0_exp1 = [1,1.04,1.21,1.35,1.13,0.0881,0.0531,0.05];


D2 = [0,7,13,26];
NoN0_exp2 = [1,0.809,0.00223,0.000152];


D3 = [0,270,406];
NoN0_exp3 = [1,0.0735,0.00224];


D = [D1,D2,D3];
NoN0_exp = [NoN0_exp1,NoN0_exp2,NoN0_exp3];
exp_all = [D1;NoN0_exp1];
sort_exp = sortrows(exp_all');
D = transpose(sort_exp(:,1));
NoN0_exp = transpose(sort_exp(:,2));


x0 = 0;    % Initial Guess for optimization
```

```matlab
nstart = 1;
nend = 30;


markercolor = [0,0,1]; % Marker Color of Plot
markersize = 6; % Marker weight of plot
linewidth = 2; % Width of line
linecolor = [1 0.25 0]; % Color of line
plottitle = 'Vibrio Harveyi Dose Response at 330 nm'; % Title of Plot

SAVEPLOT = 1; % 1 Saves PDF of figure, 0 does not save anything
plotnum = 330;   % Save file num
fp = 'D:\Melissa\Maggie\DoseResponseGraphsCombined'; % Save file path



% CALCULATIONS
fdata = zeros(length(nstart:nend),4);   % Contains optimization data
fdata(:,1) = transpose(nstart:nend);

options = optimset('MaxFunEvals',500);      % Limit Fun Evals to 500

ct = 1;
for w=nstart:1:nend  % Hard code n values
    [x,fval,exitflag] = fminsearch(@(x) VH(x,w,D,NoN0_exp),x0,options);
% Search for optimal k value for given n
    fdata(ct,2) = x;          % Optimal k Value
    fdata(ct,3) = fval;       % Optimized cost function value
    fdata(ct,4) = exitflag;   % Save exit flag for reference
    ct = ct + 1;
end

funvals = fdata(:,3);
[RSS,index] = min(funvals);    % Determine min function value
n_opt = fdata(index,1);
k_opt = fdata(index,2);


ymean = mean(log(NoN0_exp));
TSS = sum((log(NoN0_exp)-ymean).^2);


r2 = 1-RSS/TSS;

fprintf('\n\n-----Correlation-------\nRSS = %f\nr^2 = %f\nExit Flag:
%i\n',RSS,r2,fdata(index,4))
fprintf('Optimal k = %f\nOptimal n = %f\n\n',k_opt,n_opt)


D_reg = transpose(linspace(D(1),D(end),1000));
NoN0_reg = zeros(length(D_reg),1);
for p = 1:1:length(D_reg)
    sumval = 0;
    for ct = 0:1:(n_opt-1)
        sumval = sumval + ((k_opt*D_reg(p))^ct)/factorial(ct);
    end
```

```matlab
        NoN0_reg(p) = exp(-k_opt*D_reg(p))*sumval;
end


% PLOT RESULTS
figure(13)
semilogy(D1,NoN0_exp1,'o','MarkerFaceColor',markercolor,'MarkerSize',ma
rkersize,'MarkerEdgeColor',markercolor)
hold on
semilogy(D2,NoN0_exp2,'^','MarkerFaceColor',markercolor,'MarkerSize',ma
rkersize,'MarkerEdgeColor',markercolor)
hold on
semilogy(D3,NoN0_exp3,'s','MarkerFaceColor',markercolor,'MarkerSize',ma
rkersize,'MarkerEdgeColor',markercolor)
hold on
semilogy(D_reg,NoN0_reg,'-','LineWidth',linewidth,'Color',linecolor)
legend('Experimental','Theoretical')
title(plottitle,'FontSize',12,'FontWeight','bold')
xlabel('Dose (mJ/cm sq.)','FontSize',12,'FontWeight','bold')
ylabel('log(N/N0)','FontSize',12,'FontWeight','bold')
set(gca,'LineWidth',2,'FontSize',10,'FontWeight','bold','Box','on')
set(gcf,'Color',[1 1 1]);

% SAVE PLOT RESULTS
if SAVEPLOT
    print(13,'-dpdf',[fp,num2str(plotnum,'%03i'),'.pdf'])
end
```

Vibrio harveyi run file

```matlab
function [f] = VH(x,n,D,NoN0_exp)

errors = zeros(length(D),1);

for p=1:length(D)
    sumI = 0;
    for i = 0:1:(n-1)
        sumI = sumI + ((x*D(p))^i)/factorial(i);
    end
    errors(p) = log(NoN0_exp(p)) - log(exp(-x*D(p))*sumI);
end



f = sum(errors.^2);



end
```

Cryptosporidium parvum

```
SLSE_MIN = 1E6;
D = [0 25 50];
y_exact = [0 0.273 2.48];
ct = 1;
for w = 0:0.0001:5
    y_curr = 0.1536*(w*D).^2 + 0.2998*(w*D);
    SLSE(ct) = sum((y_curr-y_exact).^2);
    if SLSE(ct) < SLSE_MIN
        SLSE_MIN = SLSE(ct);
        w_opt = w;
    end
    ct = ct + 1;
end

funvals = 0.1191*(w_opt*D).^2 + 0.3264*(w_opt*D);
ymean = mean(y_exact);
SStot = sum((y_exact-ymean).^2);
SSres = SLSE_MIN;

r2 = 1-SSres/SStot;
```

Appendix C   TUV Parameter Data for All Studied Locations

These figures provide all of the TUV input data on the 15th of every month in 2015 for every location studied. Figure C 1 containts the nitrogen dioxoide erythmal data, C 2 contains the data for sulfur dioxide, C 3 has aerosol optical depth, C 4 has ozone data and C 5 is solar irradiance at 305 nm.
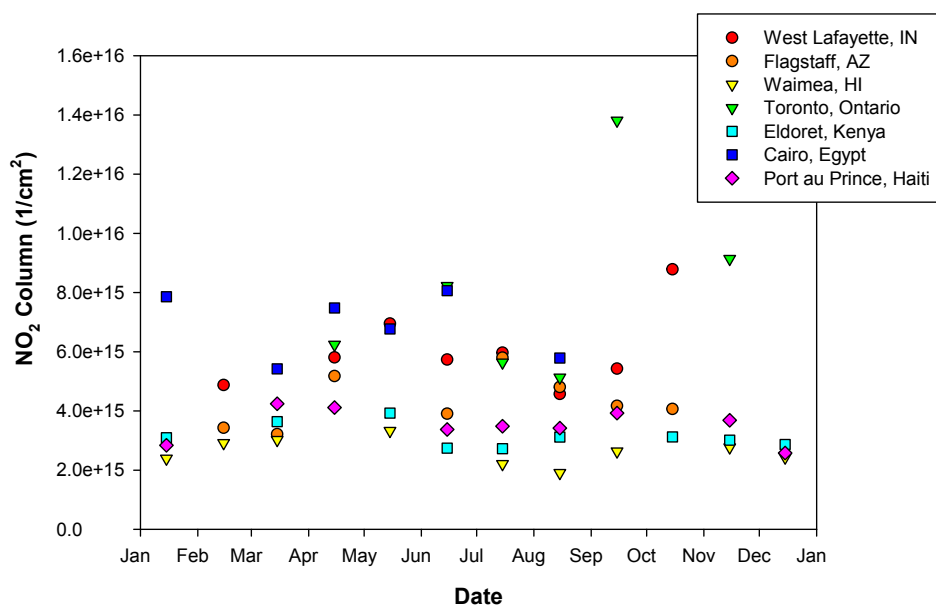

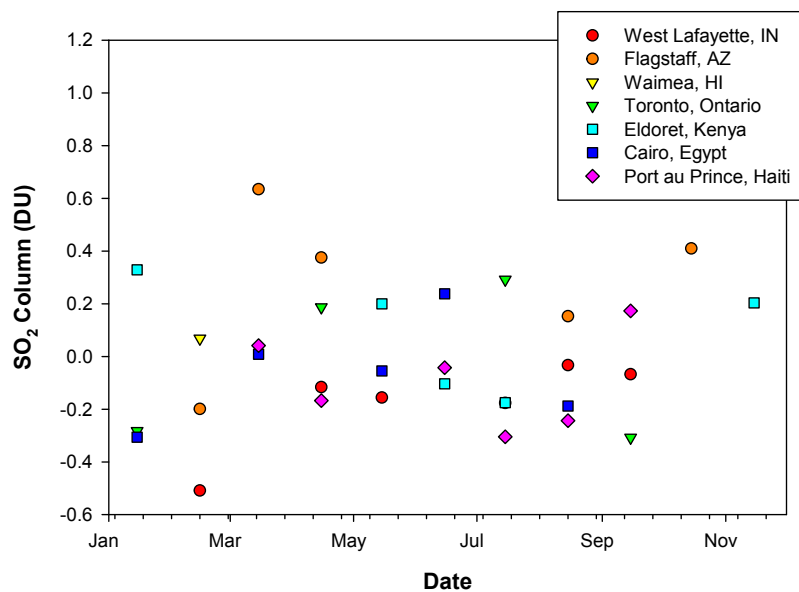Figure C 1. Comparison of NO_2 column by location on the 15th of every month in 2015.

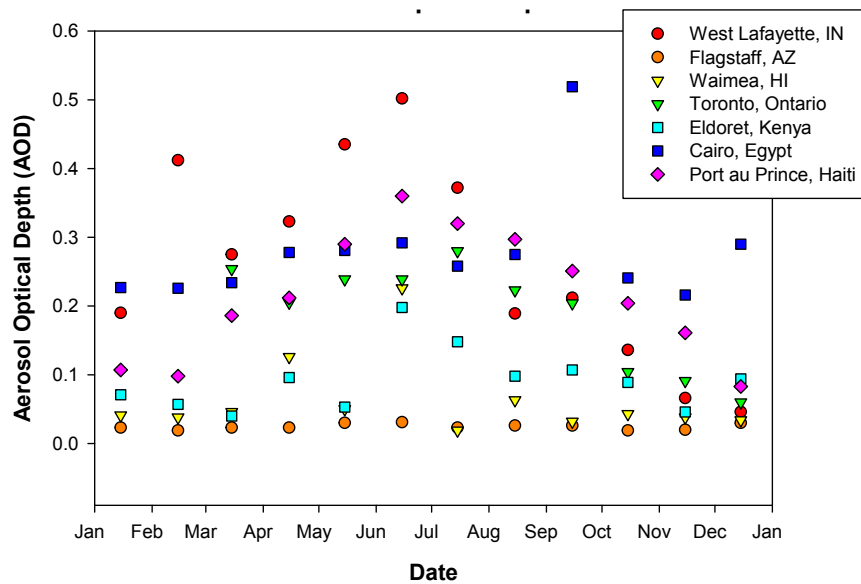Figure C 2. Comparison of SO_2 column by location on the 15th of every month in 2015.

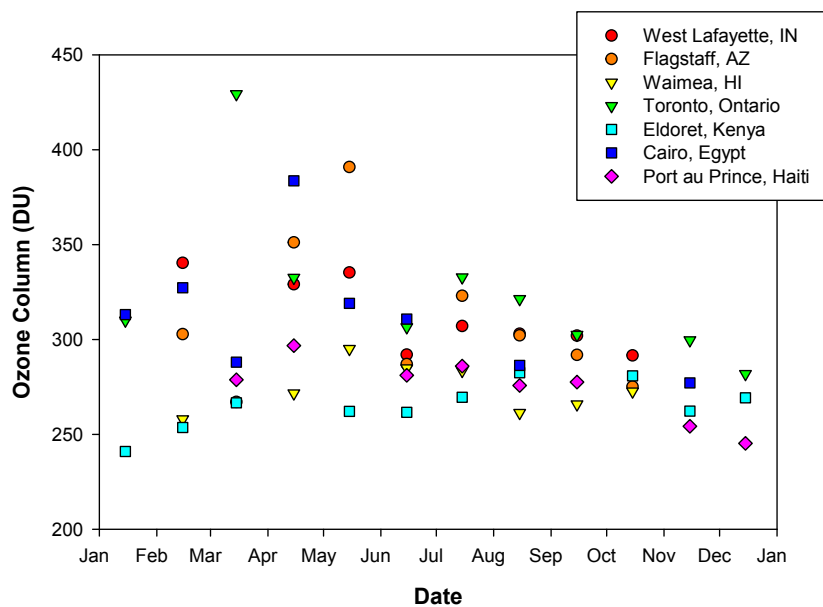Figure C 3. Comparison of AOD column by location on the 15th of every month in 2015.

Figure C 4. Comparison of Ozone column by location on the 15th of every month in 2015.
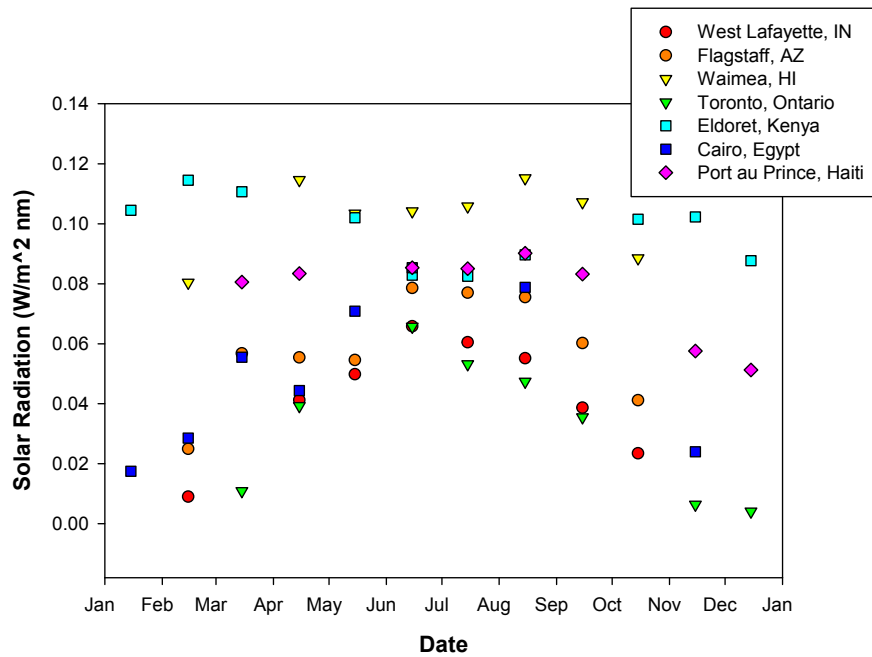

Figure C 5. Comparison of peak solar radiation by location on the 15th of every month in 2015.